Doctoral Thesis

Study on Two-Dimensional
Transition Metal Dichalcogenide-Based
Semiconductor-Graphene Heterostructures

Se-Yang Kim

Department of Materials Science and Engineering

Graduate School of UNIST

2019

Study on Two-Dimensional Transition Metal Dichalcogenide-Based Semiconductor-Graphene Heterostructures

Se-Yang Kim

Department of Materials Science Engineering

Graduate School of UNIST

Study on Two-Dimensional

Transition Metal Dichalcogenide-Based

Semiconductor-Graphene Heterostructures

A thesis/dissertation

submitted to the Graduate School of UNIST

in partial fulfillment of the

requirements for the degree of

Doctor of Philosophy of Science

Se-Yang Kim

5. 31. 2019 of submission

Approved by

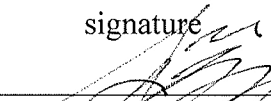—————————————————

Advisor

Soon-Yong Kwon

Study on Two-Dimensional Transition Metal Dichalcogenide-Based Semiconductor-Graphene Heterostructures

Se-Yang Kim

This certifies that the thesis/dissertation of Se-Yang Kim is approved.
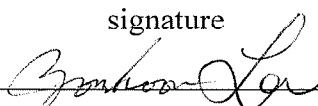
5/31/2019

signature

_____

Advisor: Soon-Yong Kwon

signature

_____

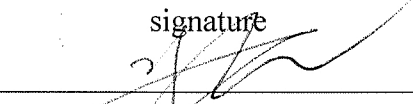Zonghoon Lee: Thesis Committee Member #1

signature

_____

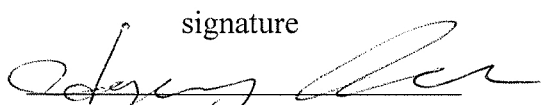Hyung-Joon Shin: Thesis Committee Member #2

signature

_____

Jung-Woo Yoo: Thesis Committee Member #3

signature

_____

Hyesung Park: Thesis Committee Member #4

ABSTRACT

Following the rise in popularity of various two-dimensional (2D) materials, e.g., graphene (Gr), hexagonal boron nitride (h-BN), phosphorene, and transition metal dichalcogenides (TMDs), the stacked structure of these layered 2D materials (called van der Waals heterostructures) has played an important role in overcoming the limitations of individual 2D materials and expanding the range of attainable properties for use in various fields.

In this thesis, we introduced the source contact geometry between a source and a substrate and optimized the direct growth method to obtain high-quality and uniform WS_2/Gr heterostructures with strong interlayer coupling. The obtained, epitaxially grown WS_2/Gr heterostructure possesses increased domain sizes and an enhanced coverage of monolayer WS_2 without compromising the quality of the WS_2 or significantly damaging the underlying graphene. Particularly, the symmetrical and narrow photoluminescence (PL) peak reveals the superior crystallinity of the grown WS_2. This result is in contrast to those obtained by different conventional methods, such as the exfoliation method and CVD growth with conventional opened geometries.

While they host many exciting potential applications, some of these 2D materials are subject to environmental instability issues induced by interaction between material and gas molecules in air, which poses a barrier to further application and manufacture. To overcome this, it is necessary to understand the origin of material instability and degradation processes in air, as well as developing strategies to extend air-stabilty. The long-term investigations on air stability indicate that the resulting WS_2/Gr heterostructures exhibit outstanding stability, in contrast to the general short-term degradation of 2H phase TMD (2H-TMDs) flakes grown on conventional substrates. This results not only describe the superior crystallinity of as-grown WS_2 on graphene, but electron microscopy images, X-ray photoelectron spectroscopy (XPS) results, and Photoluminescence (PL) spectra collected over months suggest that graphene serves a new role by obstructing the aging propagation.

This result shows how important interlayer interactions are in the stacking configuration of the vdW heterostructure. As an additional study, we show that the characteristics of the subsequent layer

in vertical van der Waals (vdW) heterostructure are considerably affected by the structural defects of the template layer, comparing two types of directly synthesized WS_2 flakes on CVD graphene; on the pristine basal plane of graphene (B-WS_2) and on graphene defects (D-WS_2). Both of WS_2 flakes show the same crystal structure without atomic displacement and lattice distortion. However, they strongly influenced by interlayer interactions between the stacked layers, affecting the physical and electrical properties including deformability, thermal stability, and junction property. Combined experimental and theoretical studies have shown that the difference in the properties of D-WS_2 flakes could be originated from the covalent bonds formed via W atomic bridges with hybridized orbitals at defect sites of graphene. These results suggest that it is importance to understand the interlayer interactions in 2D vdW heterostructures.

TABLE OF CONTENTS

LIST OF FIGURES

Figure 3.1 TEM and EDS results of 2H-MoTe$_2$ crystals. (a) A BF-TEM image and (b) corresponding atomic resolution image of MoTe$_2$ crystal. Inset: Intensity line profiles taken from a blue line in (b). (c) EDS spectra taken from several MoTe$_2$ crystals. (d)-(f) SAED patterns taken from (d) blue-, (e) red-, and (f) yellow-dotted circles in (a), respectively. Reproduced from ref [6].

Figure 3.2 Simple schematic illustrations showing a dry transfer process of MoTe$_2$ crystal to the target substrate using PDMS.

Figure 3.3 (a-f) SE and BSE mode SEM images of MoTe$_2$ crystal in time sequence. BSE mode images (b,d,f) are the zoomed-in surfaces obtained from each yellow box in SE mode images (a,c,e).

Figure 3.4 (a-c) BSE mode SEM images of severe degradation point on the aged MoTe$_2$ crystals. Each image is a representative image of (a) screw dislocation center, (b) crystal edge, and (c) grain boundary in the crystal. (d,e) SE and BSE mode SEM images on the 1 month aged MoTe$_2$ crystal.

Figure 3.5 (a-f) BSE mode SEM images measured on the surface of MoTe$_2$ crystals in time sequence.

Figure 3.6 (a) AFM topography image and height profile (white dotted line in topography image) measured on the same sample in Figure 3.5c. (b-e) Zoomed-in SE and BSE mode SEM images from white dotted boxes in Figure 3.5c and e, respectively.

Figure 3.7 (a,b) BSE mode SEM images of (a) as-grown and (b) 300-days-aged WS$_2$/Gr. (c) Low-magnification TEM image (HR-TEM image in the inset) of the suspended WS$_2$/Gr (aged for 300 days). (d,e) BSE mode SEM images of (d) as-grown and (e) 14-days-aged WS$_2$/SiO$_2$ (aged for 300 days in the inset). (f) Low-magnification TEM image (HR-TEM image in the inset) of the suspended WS$_2$/SiO$_2$ (aged for 7 days).

Figure 3.8 (a) PL spectra of WS$_2$/Gr, WS$_2$/SiO$_2$, and WS$_2$-tf-Gr. (b-e) Emission mapping images of (b-c) WS$_2$/Gr and (d-e) WS$_2$/SiO$_2$: (b, d) the intensity maps and (c, e) the position maps of the emission peaks.

Figure 3.9 (a) BSE mode SEM images of WS$_2$ flakes grown on graphene using a shorter growth time (20 min) to show various growth points as studied in Figure 2.6a. SEM images of (b) as-grown and (c-f) aged WS2/Gr. The images in (d-f) are zoomed-in images of WS$_2$ grown at (d) basal plane, (e) GBs, and (f) wrinkled region after aging for 180 days. The red and blue lines serve as guides for the GBs and wrinkles in graphene, respectively.

Figure 3.10 DF-TEM image (left) and Low HR-TEM images (right) of 180 days aged WS$_2$/Gr obtained at the normal edge (corresponding to the area in the green box in DF-TEM image).

of (f) and (g). Blue and red shaded areas in (g) indicate electron sharing between WS$_2$ flakes and graphene with W atomic bridge.

Figure 4.7 Low-loss EELS spectra in B-WS$_2$ flakes (blue curve) and D-WS$_2$ flakes (red curve) on graphene.

Figure 4.8 (a) The topography (height) image and (b) corresponding current image (recorded at +0.2V) of WS$_2$ flakes grown on graphene. (c) I-V curves recorded with Pt-Ir coated tip on B-WS$_2$ flakes (blue curve) and D-WS$_2$ flakes (red curve) on graphene.

LIST OF TABLES

CHAPTER 1

Introduction to Synthesis of Transition Metal Dichalcogenides

1.1 Introduction

Graphene, a representative two-dimensional material with atomic layer thickness, has drawn great attention from researchers over the past decade due to its excellent electrical, mechanical and optical properties that cannot be achieved with conventional three-dimensional materials.[1, 27-29] The excellent properties of graphene are attributed to semi-metallic electronic structures with zero-band gap, but they have limitations that are difficult to apply to semiconductor-based electronics industries such as silicon due to the disadvantage of not having band gaps in contradiction. Researches on gap-opening strategies have been actively carried out, but there is a problem that formation of band gap is limited, and charge mobility is drastically reduced upon formation of band gap.[30-32]

Thus, other 2D layered vdW materials having excellent semiconductor characteristics have been investigated beyond graphene in recent years. Especially, group 6 transition metal dichalcogenides, represented by the formula MX_2 (M = Mo and W, and X = S, Se, and Te), have opened new viewpoints for future applications.[4, 33, 34] For example, the field-effect transistors (FETs) fabricated with the monolayer MoS_2 flakes exhibited superior electrical performance with high on-off ratios of $\sim 10^8$ at room temperature (RT),[4] and it could be used in future circuits requiring low standby power. Also, Strong emission and large exciton binding energy from direct bandgap structure of monolayer MoS_2 layer can be utilized for superior optoelectronic applications.[33, 34] Theoretical and experimental results for these materials have strikingly increased in recent studies. Up to now, "top-down" methods (specifically, mechanical exfoliation) were used to obtain the best quality 2D vdW flakes.[3, 32] However, exfoliation methods are not only irregular in size, thickness, orientation, and phase, but also process is not suitable for large scale mass production.

Chemical vapor deposition (CVD) method is the most promising "bottom-up" approach for scalable synthesis of high crystallinity graphene[2] and other 2D vdW materials[6, 35, 36] with low defect concentration for practical applications, such as flexible electronic and optoelectronic devices, sensors, and catalysts. An evolutionary history of major experimental issues in CVD-based synthesis of 2D TMDs is shown in Figure 1.1, with the isolation of graphene[1] and MoS_2 flakes[4]. It is well known that CVD method produces films of high quality and uniformity that are scalable and cost less than those produced by chemical exfoliation. However, comparing the properties of CVD-produced 2D vdW films to those of exfoliated flakes, the latter continue to exhibit much better quality thus far.[37, 38] Currently, the controlled CVD growth of large-area, defect-free, and homogeneous films is important, especially for their optoelectronic and electronic applications. However, in CVD synthesis of 2D vdW films, different chemical reaction pathway and growth mechanism could be induced by slight changes in

growth parameters like precursor, growth temperature, pressure, substrate and flow rate[25, 39, 40]. Thus, in order to improve the fine control of 2D vdW synthesis with precise composition and crystal structure, a deeper understanding for the thermodynamics and kinetics associated with the chemical reactions and growth mechanisms are required. Furthermore, many difficulties remain in realizing pragmatic applications of 2D materials, such as the formation of vdW heterostructures with abrupt interfaces[8, 41] and the controlled concentration and carrier type in heterojunction devices.[42, 43]
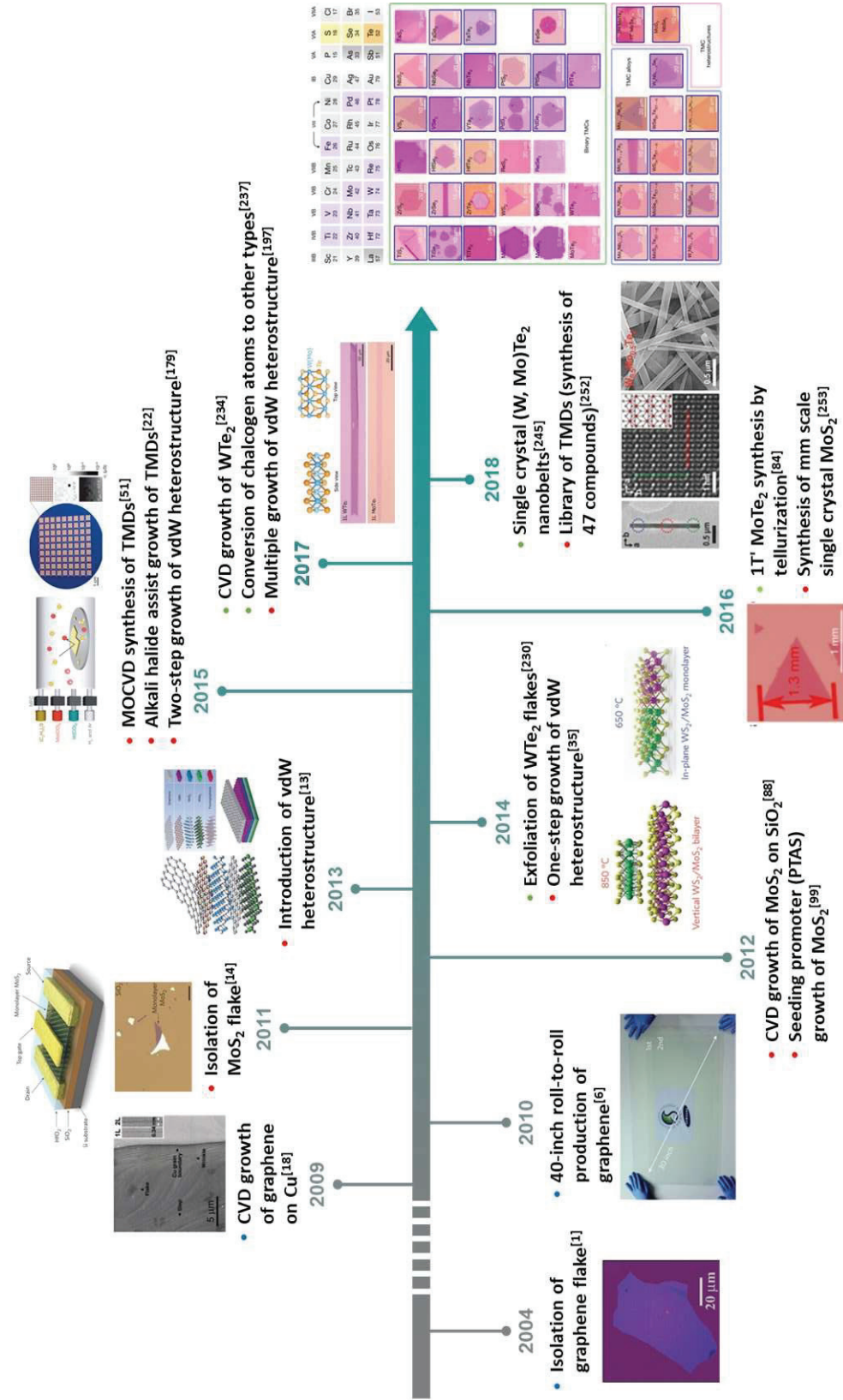
Figure 1.1 A chronological table of the major results in vapor phase synthesis of TMD materials. The first preparations of graphene and 2D TMD flakes (i.e., MoS$_2$) by mechanical exfoliation method are also included. Reproduced from ref [1-19].

3

1.2 Basic Growth Models of 2D Material Growth by CVD Method

In the CVD synthesis of 2D materials, various growth variables including temperature, pressure, flow rate, substrate are involved in the nucleation and growth. According to previous reports, there are three major growth models in 2D material synthesis: layer-by-layer (LBL), screw-dislocation-driven (SDD),[44] and dendritic growth models.[45] In addition, the determination of the growth modes depends on the supersaturation concentration of the reactants. Figure 1.2a shows LBL growth model, commonly observed in graphene and various 2D TMD synthesis. Because the nucleation of a layer requires overcoming high energy barriers, high supersaturation conditions are highly important for the initiation of nucleation and for the appropriate crystal growth rate for LBL model.[46] In the synthesis of 2D materials using CVD process, suitable concentration control of the reactants gives precise controllability of the number of layers and layered vertical heterostructures. Previously, SDD model was mainly presented in the synthesis of 1D oxides and nitrides in the solvent.[47] Meanwhile, recent reports have revealed that 2D materials are able to follow SDD model (Figure 1.2b) under low supersaturation environments in CVD system.[48, 49] The new layer occurs at the center of the first layer with a faster growth rate than the bottom layer, and stop growing when catch up with the bottom layer. As a result of this SDD model, the obtained 2D materials exhibit a pyramidal shape, and recent studies showed that their threading dislocation carry out the helical electrical transport in the vertical direction with the conductance enhancement.[50] These models are important as a potential strategy to control the rotation angle or number of stacking of layers in 2D materials.
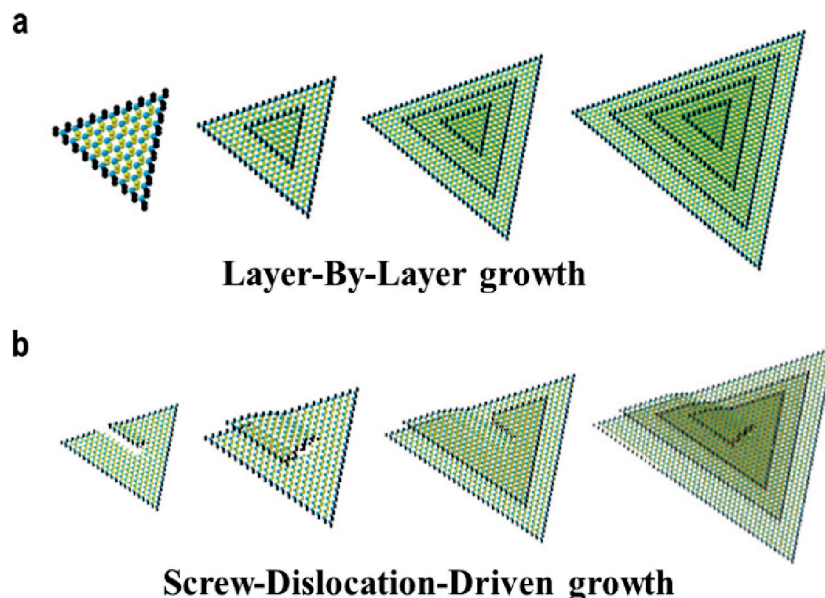
Figure 1.2 Schematic illustrations of (a) LBL and (b) SDD growth model, respectively. Reproduced from ref [20].

1.3 Major Variables in CVD Growth of 2D Materials

CVD is the process that includes the activations and chemical reactions of gaseous reactants, with their nucleation and growth on the target substrate. In particular, CVD process must be able to: i) transport the reactants with carrier gases into the growth chamber, ii) provide sufficient energy for the efficient progression of chemical reactions, and iii) transport and remove of by-products. Growth parameters for this CVD process are highly important because the structural features of obtained film (such as morphology, defect concentration, and phase), which can be controlled by growth parameters, greatly influence the characteristics of the 2D materials.

1.3.1 Reactants and Precursors

Molecular precursors play in a role in reactants for the process of CVD. In short, three reaction processes (thermal decomposition, chemical transport, and chemical synthesis) are commonly involved in converting precursors into the target products. Those precursors should be capable of thermal decomposition at the target temperature and enough volatility to have an acceptable growth rate. However, as a characteristic of CVD, the energy for activating the entire process varies depending on their types of precursors. Recently, CVD method was modified to accommodate the expandable growth for single crystalline graphene, and the layer thickness was reduced to a monolayer.[2, 5, 38] As C sources for graphene growth, various hydrocarbon precursors are generally applied, such as CH_4, $CH_2=CH_2$, and $CH\equiv CH$ (the reaction energy of dehydrogenation: 410, 443, and 506 kJ/mol).[51] The thermal activation of methane (CH_4) is particularly challenging because dehydrogenation in the gas phase of CH_x to CH_{x-1} is highly endothermic, with the calculated values of 4.85, 5.13, 4.93, and 3.72 eV required for the successive dehydrogenation to CH_3, CH_2, CH, and C, respectively.[51, 52] Owing to the strong TM-CH_{x-1} and TM-H interactions, there is a significant reduction in these values on catalytic TM surfaces such as Cu, Ni, Pt, and Pd (with activation energies ranging from 25 to 60 kJ/mol), and theoretical studies suggests that even exothermic dehydrogenation processes could occur over some TM surfaces.[51, 52] Currently, graphene growth by CVD using a CH_4 precursor is generally performed on TM surfaces at low temperatures (~900–1,050 C).[2, 5, 38] Besides, graphene can be doped with N or P atoms by introducing gaseous NH_3 or PH_3.[53, 54]

Molybdenum precursors	Melting temp. (decomposition)	Tungsten precursors	Melting temp.[°C] (decomposition)	Chalcogenide precursors	Melting temp. (decomposition)
Mo	2,623 °C	W	3,422 °C	S	120 °C
MoO_3	795 °C	WO_3	1,473 °C	Se	221 °C
MoO_2	1,100 °C	WO_2	1,700 °C	Te	450 °C
MoO_2Cl_2	175 °C	WO_2Cl_2	266 °C		Boiling temp.
$MoCl_5$	194 °C	WCl_6	275 °C	$(CH_3)_2S$	37.33 °C
$MoOCl_4$	101 °C	$WOCl_4$	211 °C	$(C_2H_5)_2S$	92.1 °C
$Mo(CO)_6$	150 °C	$W(CO)_6$	150 °C	$(CH_3)_2Se$	49.8 °C
Ammonium heptamolybdate	190 °C	Ammonium Metatungstate	100 °C	$(C_4H_9)_2Te$	50 °C

Table 1.1 Decomposition temperatures of transition metal and chalcogen precursors. Reproduced from ref [24].

In comparison, solid precursors are considerably used for the CVD-based synthesis of various TMDs at the moment. As described in Table 1.1, metal oxides $((Mo, W)O_x)$, oxychlorides $((Mo, W)O_xCl_y)$, chlorides $(MoCl_5)$, or metal thin films (or foils) commonly use as transition metal sources (Mo or W), while S, Se, or Te powders serve as chalcogen sources.[6, 7, 35, 36] Due to the different vapor pressures depending on the precursors, the parameters, such as temperature, pressure and carrier gas flow, should be carefully optimized to form a stable vapor flux in CVD process. The vapor pressures of solid precursors are also very sensitive to temperature, requiring accurate control of temperature. In particular, the controllable synthesis of W-based TMDs is known to be difficult because the sublimation temperatures of the W-containing solid precursor is much higher than the temperatures of the Mo-containing precursors.[55] Although gaseous precursors (i.e., $Mo(CO)_6$, $WOCl_4$, WCl_6, and H_2S) have been shown to enhance the uniformity of the synthesized TMD flakes or films, but the crystal quality or growth rate has been compromised.[9, 56]

1.3.2 Temperature and Kinetics

In the fabrication of optoelectronic and electronic devices, insulating and passivation films have to be evaporated to metallize device contacts and interconnects, or to encapsulate various parts of the internal circuitry. Since the upper limit temperature is about 450 °C, the processing temperature for semiconductor must be reduced.[21, 57] However, high-temperature is essential for the synthesis of high quality thin films. In a general theory of nucleation at the vapor-solid interface, a thermodynamic process is induced at the high synthesis temperature, while a kinetic process is induced at the low synthesis temperature.[57]
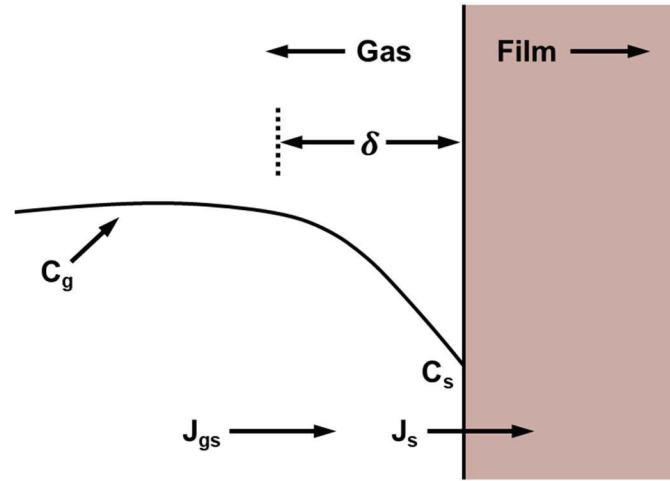
Figure 1.3 Schematic illustration of Grove model for vapor deposition. Reproduced from ref [21].

The temperature parameter in CVD generally affects the deposition rate and structural quality of products on the substrate as well as the chemical reactions of precursors in the gas phase. It is useful to revisit the treatment of the kinetics of thin film growth by Grove[21] to understand the effect of temperature. The basics of this simple model are shown in Figure 1.3, which shows the environment in the vicinity of the interface of the film grown by a gas-assisted process. A drop in the concentration of the reactant from C_g in the bulk of the gas to C_s at the interface occurs. The corresponding mass flux J_{gs} is given by

$$J_{gs} = h_g(C_g - C_s) = D_g(C_g - G_s)/\delta \quad (1.1)$$

where h_g is the gas-phase mass transfer coefficient and is relatively insensitive to variations in temperature ($h_g \approx D_g/\delta$, where D_g is the gas-phase diffusivity and δ is the boundary layer thickness). The mass flux J_s consumed by the surface reaction of the growing film is approximately proportional to C_s:

$$J_s = k_s C_s = AC_s exp(-E_a/kT) \quad (1.2)$$

where k_s is the rate constant for the surface reaction, A is a proportional constant and E_a is the activation energy of the surface reaction. In the steady state, $J_{gs} = J_s$, so

$$C_s = \frac{C_g}{1+k_s/h_g} \quad (1.3)$$

Equation (3) implies that i) if $h_g \ll k_s$, low gas transport through the boundary layer will limit the rapid surface reaction, a condition referred to as "mass transfer (diffusion) control"; ii) if $h_g \gg k_s$, the surface reaction will be stagnant even if sufficient reactant gases are available (i.e., C_s approaches C_g), referred to "surface reaction control". At low temperatures, film growth is surface-reaction-controlled, whereas at high temperatures, the film growth is mass transfer or diffusion-controlled. In a typical CVD process, actual film growth is carried out in the gas diffusion-controlled region, where the temperature response is relatively flat.

1.3.3 Growth Pressure

Before growth, the vacuum level should be minimized to obtain films with high purity. The low base pressure of the growth chamber reduces the concentration of residual gases, water molecules, and impurities.[21, 57] Previously, CVD strategies were used in low pressure (LP) systems of 0.1-1 Torr to synthesize high quality Si-based films, which improved the controllability of the contamination and stoichiometry. Practically, large batches of wafers can be processed at a time, and because of the generally high deposition rates, improved film thickness uniformity, better step coverage, lower particle density, and fewer structural defects, LPCVD has important advantages relative to atmospheric pressure (AP) (~760 Torr) CVD processing to grow wafer-scale TMD materials.[6, 35, 58] While no clear evidence has been reported that the partial pressure of a precursor can influence to the growth mode of 2D TMD films,[9] highly complicated processes and mechanisms with major growth variables are engaged in the growth pressure. Further investigations are required to reveal the impact of growth parameters for sure.

1.3.4 Substrate

In selecting the growth substrate, variables other than the material or its chemistry should be considered. Crystal structure and orientation, texture, single- and poly-crystalline character and grain size, surface morphology, and defects and impurities have proven to be crucial in the nucleation and growth of 2D materials. The substrate can be simply defined as the surface where the material is deposited in the CVD process; however, it does more. Catalytic metal substrates (i.e., Ni and Cu) are widely used as substrates for graphene synthesis as well as catalysts, because of their catalytic abilities and carbon solubilities.[2, 5, 38] Meanwhile, TMD materials are commonly synthesized on the conventional inert substrates without catalytic effect, like sapphire and SiO_2. Thus, the synthesis is easily affected by the substrate treatment before the growth.[6] Especially, the microstructure and crystal lattice of the substrate have critical effects on the vapor phase synthesis of TMDs. For instance, because of the specific lattice orientation of c- sapphire with the atomically smooth terraces, the synthesized TMDs on c-sapphire substrate showed preference for certain orientation, related to the crystal symmetry and the surface terraces of the substrates.[39, 55] Meanwhile, in the use of metal foil as a substrate, the crystallography of substrate metal can mediated a strong effect on the nucleation and domain size of TMDs by selecting different facets. This preferential growth on certain facets are explained by different binding energy between TMDs and substrates depending on the facet.[59] Furthermore, the arrangement of substrate plays an important role in the morphological control. For instance, MoS2 flakes grew into a continuous film with large domain sizes of ~20 μm on the target substrate in the vertical position of the system, as compared to the horizontally arranged substrate, due to the enhanced uniformity of the precursor.[60]

1.4 Strategies for Vapor Phase Synthesis for 2D TMDs

Many researches have been focused on the development of scalable synthesis methods for semiconducting TMD monolayer production with large crystals using various growth techniques such as PVD, pulsed laser deposition (PLD), ALD, MBE, and CVD. Among these "bottom-up" synthesis methods, CVD is most likely to achieve high-quality, wafer-scale 2D TMDs at a low cost. Presently, the CVD synthesis of TMD films can be largely categorized into the following three pathways, depending on the precursor supply method: i) direct vapor-phase chalcogenation of pre-deposited TM sources, ii) vapor deposition, and iii) metal-organic chemical vapor deposition (MOCVD).

1.4.1 Direct Chalcogenation of Solid Phase Sources

A simple strategy for obtaining TMD films is the direct chalcogenation of pre-deposited TM precursor films. The reaction mechanism used to synthesize TMDs can be understood based on the simple and direct chemical reaction. Taking the synthesis of MoS_2 as an example, Tarasov *et al*. reported thermal annealing of a pre-deposited Mo film on SiO_2 in S vapors for the preparation of wafer-scale single- and few-layered MoS_2 films (Figure 1.4a).[61] By controlling the thickness (1-5 nm) of the Mo film, they showed that the thickness of the atomic MoS_2 layer depends only on the thickness of the pre-deposited Mo film. This indicates that direct sulfurization is an easily scalable and controllable method for depositing atomically thin MoS_2 layers on target substrates. However, the MoS_2 layers synthesized using this method showed poor carrier mobilities ranging from 0.004 to 0.04 $cm^2V^{-1}s^{-1}$ at RT, due to the formation of MoS_2 layers with small grains of 10 to 30 nm and the presence of unreacted metal impurities.[62] Similarly, Lin *et al*. reported an alternative strategy that involves replacing the Mo metal with a MoO_3 thin film.[63] MoO_3 thin films of the desired thickness were prepared by thermal evaporation on a sapphire substrate to produce wafer-scale MoS_2 thin films. First, the MoO_3 film was reduced to MoO_{3-x} at 500 °C with an H_2 flow, and then MoS_2 layers were achieved over a 1×1 cm^2 substrate by sulfurization at 1,000 °C in a sulphur-rich environment. The as-grown MoS_2 film was transferred to the target substrates for electronic device fabrication, and it showed a relatively high on/off ratio of ~10^5 (tri-layer). Hussain *et al*. used radio frequency (RF) magnetron sputtering to deposit MoO_3 films, which were sulfurized at 650 °C to prepare MoS_2.[22] The thickness of the MoS_2 film can be controlled by varying the sputtering time. Sputtering times were set to 50, 80, 100 and 150 s using a RF power of 150 W, and the results were matched to monolayer, bilayer, trilayer, and few layers of the MoS_2 based on photoluminescence (PL) and Raman measurements.
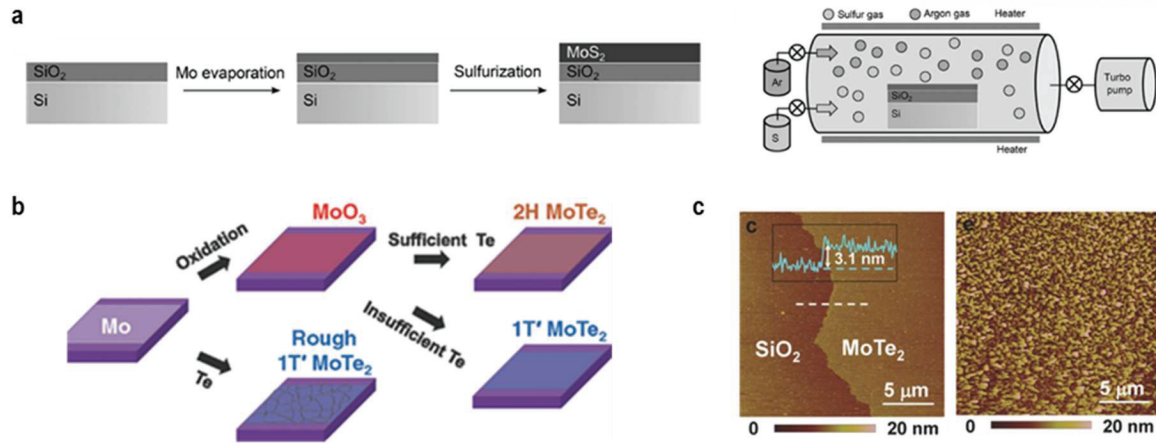
Figure 1.4 (a) Typical setup for the direct chalcogenation of the pre-deposited Mo film. Reproduced from ref [22]. (b) A schematic illustration of the growth process for 1T′ and 2H MoTe₂ using Mo and MoO₃ as precursors with controlled concentration of Te. (c) AFM images of the 1T' MoTe₂ films obtained from MoO₃ (left) and from Mo (right). (b, c) Reproduced from ref [23].

A similar strategy has also been adopted for the synthesis of other TMDs (i.e., MoSe₂, WS₂, and WSe₂) layers.[64] Moreover, Zhou *et al.* synthesized high-quality 2H and 1T' MoTe₂ films with high homogeneity.[23] Previously, the synthesis of high-quality 1T' MoTe₂ was difficult due to its inherent metastability at ambient conditions (details of TM ditellurides are presented in Section 4), with a small ground-state energy difference (~35 meV/unit cell) sensitive to the excess or deficiency of Te.[65, 66] Therefore, it is important to develop a feasible synthesis method of 1T' MoTe₂ with high crystal quality. Using the controlled tellurization of MoO₃, as shown in the schematic illustration of Figure 1.4b, 2H MoTe₂ would be obtained with a sufficient Te source and 1T′ MoTe₂ would be obtained under insufficient Te.[10] Zhou et al. also found that the TM precursor determines the quality and morphology of the as-grown 1T′ MoTe₂. 1T′ MoTe₂ grown from MoO₃ has higher quality and better uniformity than the 1T′ MoTe₂ grown from Mo film (Figure 1.4c), due to the different sublimation temperature and atomic migration behavior.

To obtain high-quality TMDs with the desired number of layers and wafer-scale uniformity, the thickness of the pre-deposited TM precursor needs to be precisely controlled. However, it is difficult to achieve uniform and precise thickness of the pre-deposited TM or TM oxide thin films. Furthermore, the as-synthesized film is generally polycrystalline with a grain size of several nanometers (~20 nm), due to limited surface diffusion (or migration) of the TM precursors.[62, 64]

In addition to the aforementioned methods, TM precursors have been deposited by dip-coating, sputtering, electron-beam evaporation, or ALD in order to find a suitable deposition condition for uniform wafer-scale chalcogenation. By controlling the number of cycles of ALD for WO₃ deposition,

Song *et al.* achieved WS_2 layers with controlled thickness.[67] However, the use of ALD precursors such as $WH_2(iPrCp)_2$ is not easy or practicable. In addition, growth is also limited to specific substrates.

In an effort to increase the grain size, Tai *et al*. introduced pre-annealed Mo foil as a TM precursor and obtained MoS_2 monolayer with a large domain of more than 50 μm in size at 600 °C within 1 min.[68] The high temperature pre-annealing process was used to enlarge the grains of Mo and improve the overall sample cleanliness, similar to the pretreatment performed during graphene growth.[69] According to the solid-state crystal growth theory, the S atoms around the Mo foil surface will first precipitate when the surface diffusion rate of S atoms on the Mo foil is higher than the bulk diffusion rate. Then, the S atoms reach super-saturation and finally react with the top layer of Mo atoms on the Mo foil.[70] They also presented the effect of crystal orientation of Mo on the synthesis of MoS_2 thin films (preferential growth of MoS_2 on the Mo(100) facets), due to the higher binding energies of S atoms on Mo(100) (3.799, 3.038, and 2.599 eV) than on Mo(111) (2.888, 2.875, and 1.939 eV) calculated by placing the S atom on the surface of a (1×1), (2×1), and (2×2) unit cell of Mo slabs, respectively.

1.4.2 Vapor Deposition

The vapor deposition method is one of the widely studied strategies for producing large-area and high-quality TMD thin films in order to meet the demands of optoelectronic and electronic applications and future scale-up fabrication. Therefore, considerable effort has been expanded to fully understand the growth of TMDs using vapor deposition. Figure 1.5a presents a typical experimental setup for vapor deposition. Each TM and S precursor (MoO_3 and S powders, representatively) was placed in a quartz tube. The reaction process for the vapor deposition of 2D TMDs using MoO_3 as a TM precursor is as follows: i) the evaporated metal oxide precursor is initially reduced by S vapor to form a volatile MoO_xS_y intermediate phase; ii) MoO_xS_y diffuses from the carrier gas onto the target substrate; iii) on further reaction with the S vapor during the migration, MoO_xS_y initiates nucleation and forms MoS_2 flakes. As a result, the concentration of individual chemical species and their ratios, the flow rate of the carrier gas, the growth temperature, and the source–substrate configuration are key parameters governing the quality as well as uniformity of the TMDs grown. The control and optimization of these factors pose challenges for controlling the nucleation density and sheet size of the 2D TMD materials. In particular, the source–substrate configuration, including precursor methods, is very crucial because it can control all the factors listed above. With regard to the configuration of the target substrate with respect to TM precursor, there are three different approaches as shown in Figure 1.5b: i) point-to-face,[6, 25, 71] ii) horizontal,[37, 55] and iii) face-to-face.[72, 73]
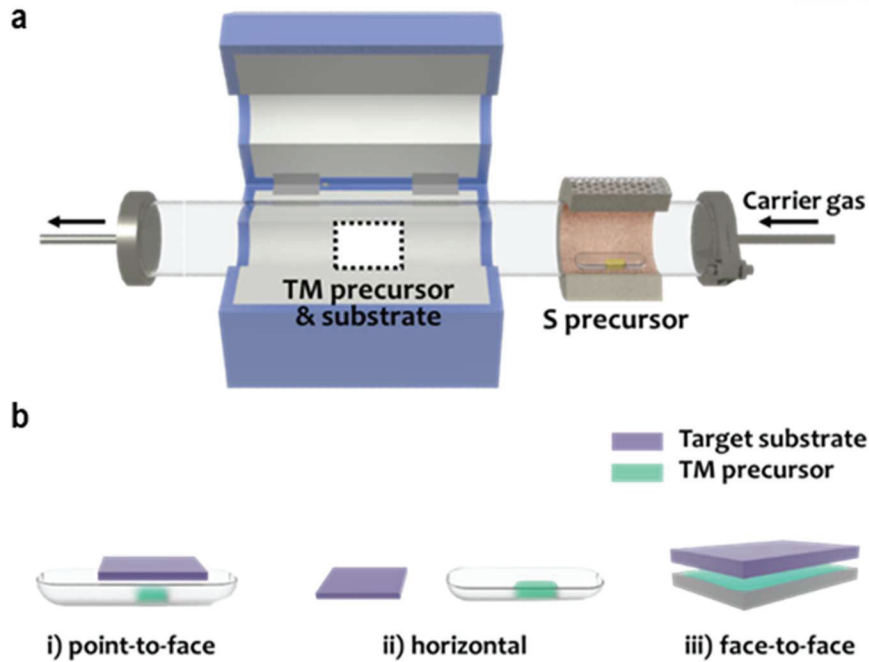
Figure 1.5 (a) Experimental setup of the vapor deposition furnace. (b) Schematic illustrations of three configurations of the target substrate with respect to metal precursor: point-to-face, horizontal, and face-to-face. Reproduced from ref [24].

In the early stage, point-to-face and horizontal precursor supply approaches have been proposed for growing TMD monolayers with controllable thickness and large grain size. These approaches have involved the use of a solid TM oxide powder as a precursor (e.g., MoO_3). Lee *et al*. proposed a point-to-face precursor supply approach to grow large-domain TMDs with controllable thicknesses. They reported the successful synthesis of single-crystalline MoS_2 flakes directly on SiO_2 substrate by facing downwardly towards the MoO_3 precursor. It has been widely used as a framework for the fabrication of TMD films.[6] However, with the point-to-face configuration, it is not easy to reproducibly obtain uniform large-area monolayer films by using this powder-based approach. This is attributed to the inhomogeneous distribution of the MoO_3 powder and the limited control over the nucleation density from the fast-kinetic reactions at high temperatures.[25, 74] In this regard, Wang *et al*. and Rajan *et al*. studied intensively the relationship between the mass ratio of the precursor to the morphology evolution of MoS_2 and the temperature and flow rate.[39, 71] As shown in Figure 1.6a, the MoO_3 vapor concentration varies depending on the Mo source and the growth position on the substrate, based on which the ratio between Mo and S varies in the reaction, as shown in Figure 1.6b.
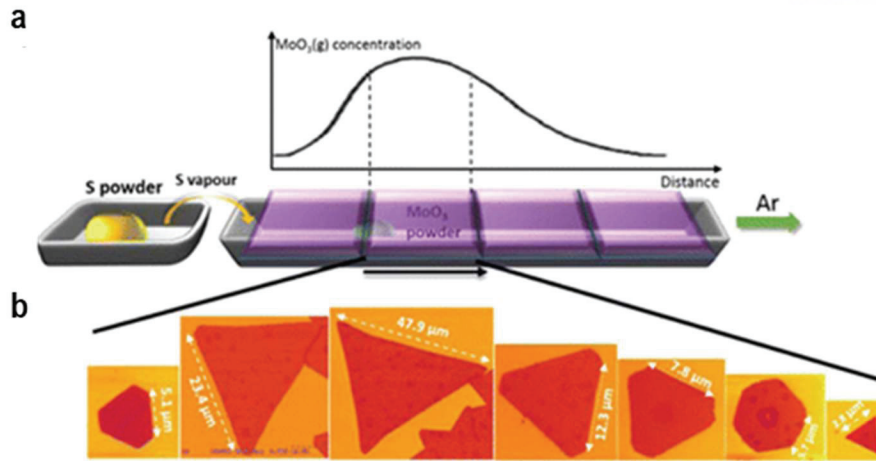
Figure 1.6 (a) Schematic diagram of point-to-face CVD process showing the spatial sectioning of the growth substrate with various MoO_3 vapor concentrations as a function of distance between Mo source and substrate. (b) AFM images for shape evolution of MoS_2 crystals depending on the spatial location of the substrate. (a, b) Reproduced from ref [25].

As a result, the shape and size of the grown MoS_2 differs depending on the location. Based on the results of these studies, strategies are needed to deliver TM precursors sufficiently and uniformly because the point-to-face structure is difficult to be applied to a variety of reactor types and conditions and has limited reproducibility.

In order to demonstrate the synthesis of triangular domains and continuous MoS_2 films, Najmaei *et al.* used a horizontal supply configuration instead of the point-to-face configuration, by placing MoO_3-nanoribbon-covered plate alongside the target Si substrates.[37] However, the MoS_2 flakes obtained using horizontal configuration were also irregular and showed a position-dependent result with low coverage.[75] Both the configurations have shown that controlling the nucleation reaction at the initial growth stage is one of the important factors for obtaining a large domain size. Özden *et al.* showed that larger flakes can be obtained even with the point-to-face approach by using closed crucibles to achieve a higher transition metal precursor confinement effect in the growth zone.[76] In their study, they were able to control the size and shape of the flakes by changing the substrate crucible types and adjusting the S/MoO_3 ratio.

To address this issue, Wang *et al.* oriented the growth substrate in a vertical position with its surface perpendicular to the gas flow direction and improved the uniformity of the precursor feed-stock compared to the horizontally positioned growth substrates.[77] Such vertically loaded substrates can decrease the thickness of the boundary layer (δ) and reduce the diffusion energy barrier for precursors to reach the substrate. In contrast, with a horizontally positioned substrate, the boundary layer is much

thicker than that with a vertical substrate, resulting in a sharp reduction in the precursor concentration as it passes through the boundary layer, which limits the growth of the TMD films.

Unlike transition metal or transition metal oxide precursors, which have a high melting temperature (see Table 1.1), volatile compound precursors (such as $Mo(CO)_6$, $MoCl_5$, and WCl_6) have a high vapor pressure even at rather low temperatures (<500 °C), thus having a higher pressure than that of TM precursor in the atmosphere.[78] For instance, Yu et al. used $MoCl_5$ as a precursor to synthesize MoS_2 over a wafer-scale. Depending on the partial pressure of $MoCl_5$, they also obtained MoS_2 films with the controlled layer numbers. They suggested that the growth mechanism of uniform MoS_2 films using $MoCl_5$ source is a "self-limiting" process, which is assumed to be the formation of gaseous MoS_2 followed by diffusion to the substrate and further precipitation to the MoS_2 flakes.[79] However, the quality and growth rate of the grown material were reduced,[7, 9] for example, the carrier mobilities of the MoS_2-based FETs were only 0.003–0.03 $cm^2V^{-1}s^{-1}$. Furthermore, transition metal halides and hexacarbonyls can release highly corrosive HCl and carbonaceous residues upon decomposition, respectively, and these residuals can cause degradation of the grown crystals.[9, 78]

O'Brien et al. proposed a face-to-face geometry for the growth of MoS_2 monolayers by using liquid exfoliated MoO_3 nanosheets as the TM precursor.[80] This close proximity precursor supply was achieved by drop-casting the MoO_3 nanosheets onto the substrates, and then placing the growth substrates face down on top of them.

1.4.3 Metal-Organic Chemical Vapor Deposition (MOCVD)

As described earlier, solid-phase precursors such as TM oxide and S powders have been used for both direct vapor-phase chalcogenation and vapor deposition.[73, 75] However, solid-phase precursors have limitations in the continuous and constant supply of precursors during the growth process, since it is difficult to control the vaporization of the solid precursor with temperature.[25, 58] Consequently,   the thickness and coverage of the grown TMD films exhibit undesirable variations.

On the other hand, a gas-phase precursor has the advantage of providing controllability.[81] Though a gas-phase precursor for Mo and W has not yet been reported, a liquid-phase precursor can be an alternative. MOCVD has been used widely for the synthesis of III-V semiconductors (such as (Al, Ga, In)(N, P, As)) using liquid precursors with a bubbler system.[82] Kang et al. reported the MOCVD growth of highly homogeneous and 4-inch scale MoS_2 and WS_2 at a growth temperature of ~550 °C using a combination of diethyl sulfide (($C_2H_5)_2$S, liquid phase with a melting point of 92.1 °C) and molybdenum hexacarbonyl ($Mo(CO)_6$, solid phase with a low melting point of 150 °C) (Figure 1.7a).[9] The resulting films showed highly constant electrical properties over the entire 4-inch area (the average grain size increases from hundreds of nanometers to more than 10 μm by controlling H_2 flow), including a high electron mobility of 30 $cm^2V^{-1}s^{-1}$ for MoS_2 and 18 $cm^2V^{-1}s^{-1}$ for WS_2 at RT. Using monolayer MoS_2

film, they fabricated wafer-scale FETs with a 99% device yield and vertically stacked transistor devices through multi-level fabrication for 3D circuitry. This work suggested the feasibility of wafer-scale batch fabrication of high-performance devices and next-generation integrated circuits (ICs) with TMD monolayers (Figure 1.7b). However, the growth time for the complete monolayer MoS_2 film was long, ~27 h; this case brings into question the whole purpose of the MOCVD process and therefore, it is still necessary to find new development strategies. In addition, carbon-based contaminations from the metal-organic compounds in precursors could be introduced during the reaction, which may be undesirable for electronic applications.

In an effort to resolve the issue of growth time, Kalanyan et al. proposed a pulsed MOCVD method.[83] The pulsed injection strategy contributed to achieving layered MoS_2 at a comparatively low reaction temperature of 591 °C and short deposition times (approximately 90 s for few-layer films). They also grew films of various thicknesses by varying the number of injected pulses. This relatively low temperature and fast processing could be advantageous for applications requiring thermal compatibility with flexible glass substrates and low cycle times for roll-to-roll processing. However, the grain sizes of these continuous films are still limited to a few micrometers, which undermine their performance and applications in electronics because of the scattering of carriers at GBs.
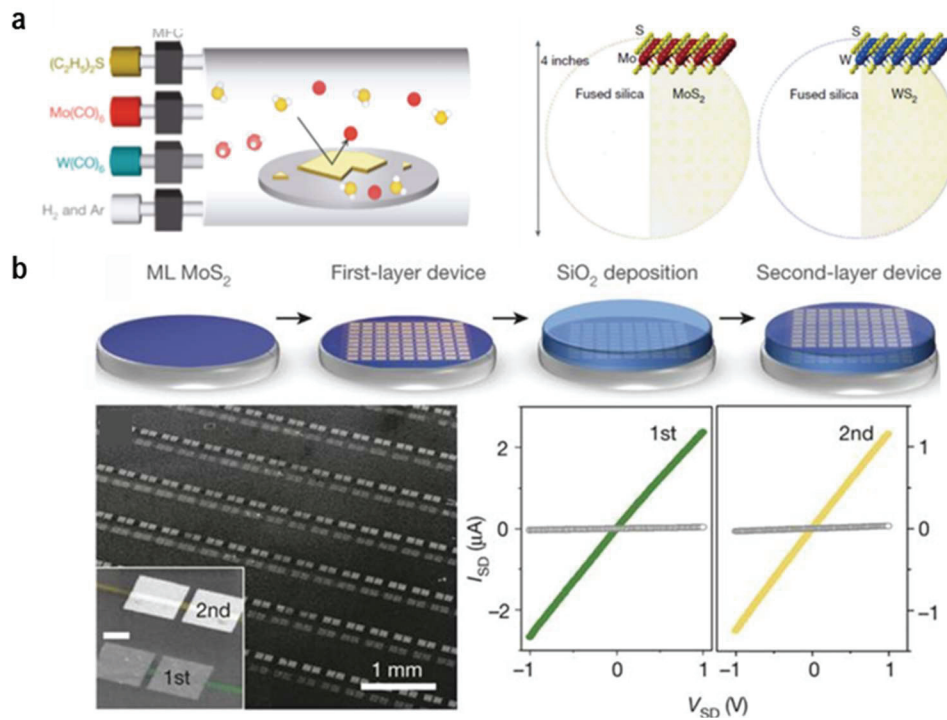
Figure 1.7 (a) Diagram of MOCVD growth setup and photographs of monolayer MoS_2 and WS_2 films grown on 4-inch fused silica substrates with bare silica for comparison. (b) Schematic illustration for multilayer device fabrication of MoS_2 device/SiO_2 by alternating MOCVD process (top). False-color SEM image of two-layer MoS_2 FET arrays, and $I_{SD}-V_{SD}$ curves obtained from the first and second layers of MoS_2 FETs, respectively (bottom). Reproduced from ref [9].

CHAPTER 2

Synthesis of 2D TMDs on Graphene for Vertical vdW Heterostructures

2.1 Vapor-Phase Growth of TMDs-Based Vertical Heterostructures

These atomically thin TMDs can also be combined with other 2D materials such as graphene, *h*-BN, and different TMDs materials to form vdW heterostructures, in which multiple layers of 2D material are vertically stacked layer–by–layer or stitched together seamlessly in a plane to form lateral heterojunctions. Heterostructures based on 2D materials have recently emerged as a new area of research in condensed matter physics and materials science. Many novel physical properties, related to electron–electron bonding and electron–phonon bonding due to layer–layer interactions, have been explored in these vdW heterostructures. In addition, the energy band alignment and charge carrier mobility of such heterostructures can be adjusted by selecting the components of the heterostructure that meet various application requirements. Thus, new materials and systems can be designed by accurately designing the components and sequences used to construct heterostructures.

There are generally two types of 2D heterostructure materials: a vertical heterostructure in which different 2D materials are stacked vertically without overlapping between layers, and a lateral heterostructure, where different 2D materials are perfectly bonded to one another in the same plane via covalent bonds. In the case of vertical 2D heterostructures, multiple step layer–by–layer stacking was easily implemented because interlayer interactions are mainly due to the vdW heterostructure and there is little or no demand for lattice matching between the different layers. Yu *et al*. reported a typical example of a vertical transistor developed by combining exfoliated graphene and MoS_2 flakes.[84] They proposed a new device structure, instead of a conventional device structure that horizontally connects the electrodes, and reported that the Schottky barrier formed between graphene and MoS_2 can be efficiently controlled to have a high current density over 5000 A/cm^2. As another example, single layer MoS_2/WSe_2 heterostructures were obtained by transferring flakes of different materials to a flake of another material using a poly(methyl methacrylate) (PMMA)–assisted method.[85]

However, the aligned stacking of individual exfoliated or transferred flakes is time consuming and suitable only for manufacturing one device at a time, which is disadvantageous to mass production. In addition, contamination caused by trapped impurities or residues at the interface and damage during the transfer process can adversely alter the intrinsic properties of each individual material and the resulting heterostructures. Therefore, the development of CVD-based methods to prepare 2D heterostructures has been explored to not only prevent contamination at the interlayer interface but also to control the lamination direction, which greatly affects the electrical and optical properties of the structures.[8, 86]

2.1.1. TMD-Based Vertical Heterostructures with Different TMDs

TMD/TMD heterostructures have attracted much attention because the stacking of different TMDs can be used to form several types of heterostructures owing to their wide bandgap and electron affinity. To fabricate artificial TMD/TMD vertical heterostructures with atomically clean and sharp interfaces, a one-step CVD method was developed with the addition of Te for accelerating the melting of W powder during the growth process.[8] In this study, MoO_3 powder is placed in front of a bare SiO_2/Si wafer for growing MoS_2, while a mixed powder of W and Te is scattered on the wafer for growing WS_2 (Figure 2.1a-c). The differences in nucleation and growth rates cause the sequential growth of MoS_2 and WS_2, instead of $Mo_xW_{1-x}S_2$ alloy formation, and the precise reaction temperature determines the structure of the final product. At high temperatures (~850 °C), WS_2 monolayer was epitaxially grown on top of MoS_2 and predominantly vertically stacked with the preferred 2H stacking order.[8] Several similar reports of CVD growth for various vertical heterostructures, such as WS_2/MoS_2, WSe_2/$MoSe_2$, WSe_2/MoS_2, and MoS_2/WSe_2, have been demonstrated through the simultaneous reaction of either TM-based precursors or chalcogens.[87, 88] Furthermore, the sequential two-step synthesis of TMD heterostructures was also reported by Gong *et al*. for the first time, where $MoSe_2$ was synthesized first, followed by the epitaxial growth of WSe_2 on the edge and on the top surface of $MoSe_2$. Their two-step growth process generated well-defined 2H and 3R stacking in the WSe_2/$MoSe_2$ bilayer regions.[89]
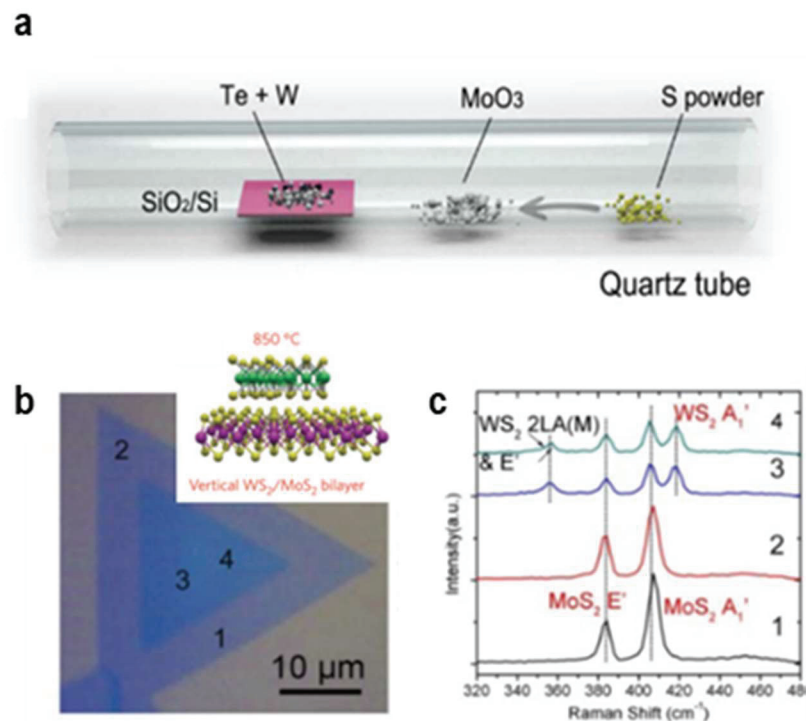
Figure 2.1 (a) Schematic of the synthesis process for both vertical and lateral heterostructures. (b) Optical image of the WS_2/MoS_2 vertical heterostructure (synthesized at 850 °C) for Raman characterization. (c) Raman spectra measured on the four points in b). (a-c) Reproduced from ref [8].

17

However, these heteroepitaxy-based CVD-grown 2D TMD heterostructures have limitations in that their location, size, thickness, and uniformity cannot be controlled. A chalcogenation of TM precursor films can provide scalability and patternability to the resulting vertical heterostructures.[90, 91] Through a two-step individual chalcogenation process, Xue *et al*. obtained periodic arrays of MoS_2/WS_2 vertical heterostructures by preventing the phase mixing of TMDs effectively in an unpredicted manner.[91]

2.1.2 TMDs-Based Vertical Heterostructures with Graphene or *h*-BN

TMDs/Graphene-based semiconductor/metal vertical heterostructures are noted in that they utilize both the advantages of TMDs with a wide choice of compositions and band gaps and graphene with tunable work function, excellent electrical and mechanical properties. Accordingly, these heterostructures show unique characteristics in electronic and optoelectronic applications.[92, 93] When considering that the most commonly used mechanical exfoliation and aligned stacking methods are difficult and only available for individual device fabrication, it is highly important to develop the CVD-based fabrication method for heterostructure.

However, at the typical growth temperatures for high-quality graphene or *h*-BN over 1000 ˚C, TMDs can possibly decompose (see **Table 2.1**).

	in air	LP (10^{-9} to 10^{-6} torr)		in air	LP (10^{-9} to 10^{-6} torr)
MoS_2	350 °C	1090 °C	WS_2	440 °C	1040 °C
$MoSe_2$	400 °C	980 °C	WSe_2	350 °C	930 °C
$MoTe_2$	400 °C	700 °C	WTe_2	427 ºC	700 °C

Table 2.1 Dissociation temperatures of group VI TMDs. Reproduced from ref [24].

Moreover, metal substrates such as Cu or Ni, which are most commonly used for graphene growth, can be corroded by the chalcogen vapor at an elevated temperature. Thus, there is no way but to synthesize TMDs on transferred graphene or *h*-BN for CVD-based heterostructure synthesis.[94, 95] One of the earliest reported attempts to fabricate the MoS_2/graphene heterostructure was by Ago *et al*. using APCVD.[26, 96] Figure 2.2a-b shows that the orientation of MoS_2 coincides with the orientation of the graphene template, exhibiting heteroepitaxial growth.[26]
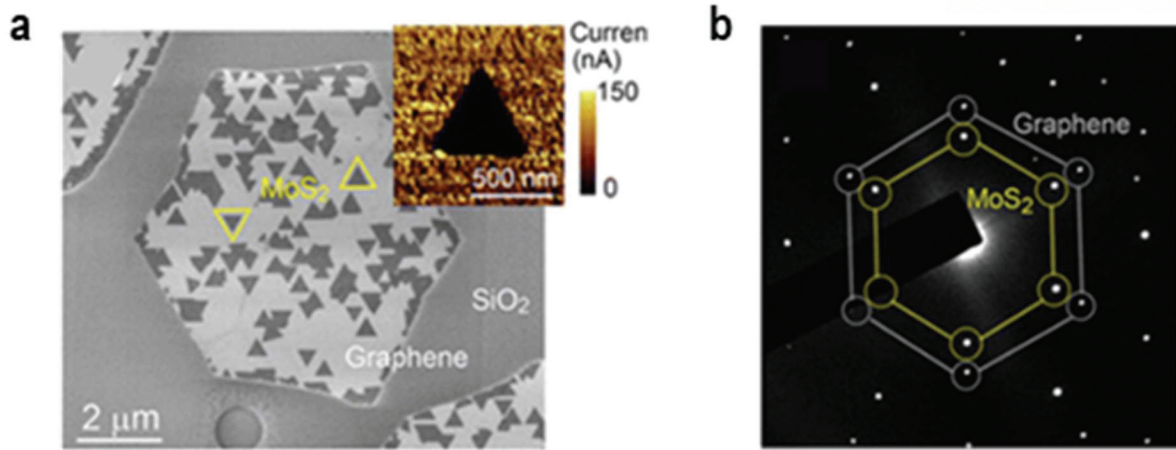
Figure 2.2 (a) SEM image of the obtained MoS_2/graphene heterostructure. Inset: a current map of the MoS_2 grain. (b) Selected-area diffraction from one MoS_2 grain. (a, b) Reproduced from ref [26].

Similarly, Wang *et al*. reported a scalable CVD method for achieving MoS_2/*h*-BN vertical heterostructures. A large-area *h*-BN film was grown on a Cu substrate by the CVD method and transferred onto a SiO_2/Si substrate. Then, MoO_3 and S powders were used as precursors to grow the individual MoS_2 domains directly on the entire *h*-BN surface.[94] Yan *et al*. also reported the direct growth of monolayer MoS_2 on *h*-BN flakes exfoliated by scotch tape.[97] The as-grown MoS_2/*h*-BN heterostructure showed considerably stable electrical environmental scattering and a high potential.

However, regardless of the target structure, these previous reports have shown common difficulties associated with a localized growth area and a limited flake size of approximately several hundred nanometers because of the high-energy barrier from the inert surface of the growth template. Therefore, the growth should be further studied to obtain large-area, uniform heterostructures of high crystal quality for potential applications. In addition to the uniformity and crystal quality, efficient interlayer interactions are another critical factor for the preparation of the heterostructures. In particular, for the photodetectors and photovoltaic devices that use TMDs as the light absorption layer and graphene as the charge-transport layer, the generated photocarriers are effectively transferred from the TMDs to graphene before recombination.

In here, we introduced the source contact geometry between source and substrate and optimized direct growth method for high quality and uniform WS_2 flakes on graphene with strong interlayer coupling. This approach allows the formation of WS_2/graphene heterostructure having increased domain sizes and enhanced coverage of monolayer WS_2 without a compromise with the quality of WS_2 and significant damage on graphene. Particularly, the symmetrical and narrow photoluminescence peak reveal the superior crystallinity of grown WS_2, compared to that obtained by different conventional method, such as exfoliation method and CVD growth with opened geometries. Our efforts to synthesize

high quality and enlarged size of TMD layers directly on Graphene with high-surface coverage can pave the way for various applications in the future of TMD heterostructures.

2.2 Experimental Methods

Preparation of graphene substrate

Graphene was grown on 25-μm-thick Cu foils (Alfa Aesar, 99.8% purity) that had been previously cut with razorblade into 4 cm × 4 cm strips, using a homemade hot-walled CVD system. These strips were electrochemically polished in phosphoric acid for 15 min to clean the bare Cu surface and were subsequently rinsed with distilled water followed by isopropyl alcohol. Then the Cu strips were loaded into a 4 inch quartz tube followed by evacuating the chamber to ~3 mTorr; the temperature was then increased to 1,000~1,050°C under an H_2 environment (H_2 flow rate of 5 sccm). After annealing of the Cu strips for 10 min, the graphene was synthesized by introducing methane gas (CH_4 flow rate of 10 sccm) and then cooling the Cu strips under the same conditions. Following the growth, graphene layers were transferred onto SiO_2/Si for further investigation using a conventional wet-transfer method assisted by poly(methyl methacrylate) supporting layer and an aqueous solution of 1M ammonium persulfate.

Direct synthesis of WS_2/Gr heterostructures

Growth of WS_2 was carried out on using a two-zone furnace system with a WO_3 thin film as the W source and S powder (99.998%, Sigma-Aldrich) as the S source. For the uniform source, 1 nm of WO_3 thin film was evenly deposited onto SiO_2/Si using an e-beam evaporator (WO_3 pellets, Tae Won, 99.99%). The obtained graphene substrate was placed face-to-face on top of WO_3 film. This WO_3/Gr assembly was loaded at the center of the heat zone of the furnace, with S powder containing boat at the upstream of the furnace. Before heating, the whole furnace system was purged with 500 sccm Ar gas (99.999 %). Then, 30 sccm Ar was introduced into the system as a carrier gas and the system was gradually heated up to 950 ℃. After reaching 950 ℃, S powder was started to melt (heated to 200 ℃) using the equipped heating jacket and kept constant for whole growth process (40 min).

Characterizations

SE mode and BSE mode SEM measurements were performed using a Cold FE-SEM (Hitachi SU-8220) with an accelerating voltage of 1kV. The surface morphologies of WS_2/Gr samples were observed using an AFM (Bruker Multimode 8) operating in tapping mode. The optical absorbance of a WS_2/Gr that was transferred onto a glass substrate was measured using UV-vis spectroscopy (Varian, Cary 5000) between 200 to 800 nm in dual-beam mode. The Raman spectroscopy and mapping were obtained using a WiTec Alpha 300R M-Raman system equipped with a computer-controlled x-y translation stage and a 532 nm excitation source. During the measurements, the laser power was kept below 0.5 mW at the sample to avoid laser-induced thermal effects or damage. The XPS spectra were measured by a K-alpha spectrometer (Thermo Fisher) using a non-monochromatic aluminum Kα X-ray excitation source operated at a power of 72 W; the diameter of the analysis area was ~0.4 mm and the pass energy for the electron analysis was 50 eV. The base pressure of the analysis chamber was less than ~1×10^{-9} mbar.

For TEM observations, the WS_2/Gr heterostructures and individual WS_2 flakes grown on SiO_2/Si were transferred onto TEM grids by wet transfer method. High-resolution (HR-TEM) images and the corresponding SAED patterns of the samples were obtained on a FEI Titan cube G2 60-300 at UNIST, which was equipped with an image-aberration corrector and monochromator. The microscope was operated at an acceleration voltage of 80 kV to decrease beam damage to the samples.

PL spectra were collected using the 514.5 nm (2.41 eV) line of an Ar ion laser as the excitation source. For micro PL measurements, the laser beam was focused onto a sample by a 50× microscope objective lens (0.8 NA), and the scattered light was collected and collimated by the same objective lens. The laser power was kept below 100 μW. To investigate the temperature dependence of the PL signal, we used a macro-PL system in quasi-back scattering geometry. The laser beam was focused with a spherical lens to a spot of ~50 μm size. The sample was mounted in a closed-cycle-refrigerator (CCR), and the temperature was varied from 10 to 298 K. The laser power was maintained below 1 mW for all of the measurements. The scattered signal was dispersed by a Jobin-Yvon Horiba iHR550 spectrometer (300 grooves/mm) and detected with a liquid-nitrogen-cooled back-illuminated charge-coupled-device detector.

2.3 Epitaxial Growth of TMDs on CVD-Grown Graphene using Contact Mode

Figure 2.3a presents a schematic of a two-zone furnace system for the direct growth of WS_2 layers on graphene with WO_3 thin film as a tungsten source and S powder as a sulfur source. For the uniform source supply, 1 nm of WO_3 thin film was deposited evenly using electron-beam evaporator, then it placed on graphene substrate with face-to-face contact (Figure 2.3a) for increasing the evaporated mass ratio per area in surface source model by decreasing the source-substrate distance.[57, 80]

Prior to a deeper analysis of the grown WS_2 or its heterostructure using the source contact geometry, the directly grown heterostructure was compared to different WS_2/Gr heterostructures prepared using an opened geometry and indirect growth, as depicted in Figure 2.3a: (type B) the direct growth of WS_2 on Gr/SiO_2/Si using WO_3 powder evaporation with an opened geometry; and (type C) the growth of WS_2 flakes on bare SiO_2/Si using the contact geometry and the subsequent transfer of those flakes to Gr/SiO_2/Si.
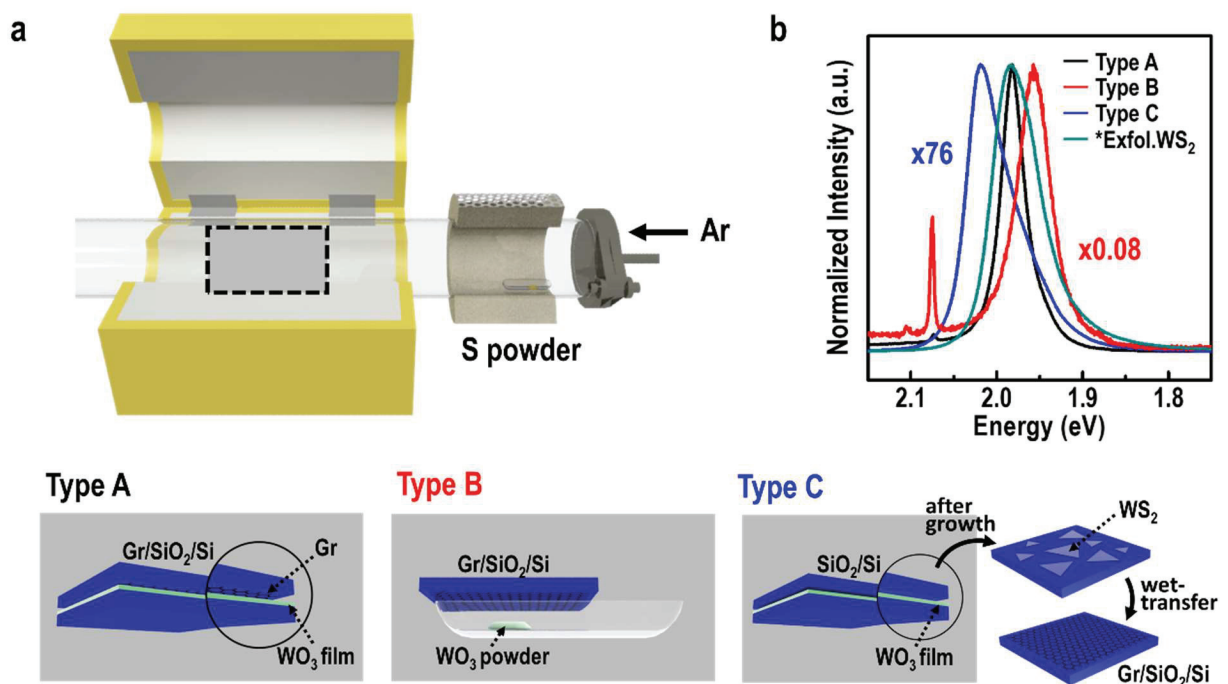
Figure 2.3 (a) Schematic of the various setup for preparing three different types of the WS_2/Gr heterostructures: (type A) the direct growth of WS_2 on Gr/SiO_2/Si using the source contact geometry and (type B) the direct growth of WS_2 on Gr/SiO_2/Si using WO_3 powder evaporation with an opened geometry, and (type C) the growth of WS_2 flakes on bare SiO_2/Si using the contact geometry and the subsequent transfer of those flakes to Gr/SiO_2/Si. (b) The normalized PL spectra of three types of the WS_2/Gr heterostructures, and the exfoliated WS_2 monolayer flake.

As a powerful tool for the characterization of crystal quality and optical properties, PL spectroscopy was used to characterize and compare these heterostructures (Figure 2.3b). All of the heterostructures show a strong emission peak at approximately 2 eV, which indicates the presence of monolayer WS_2. The smallest full-width at half-maximum (FWHM) of ~28 meV for the emission was obtained for type A, which was prepared using the source contact method; this narrow FWHM indicates a crystalline quality superior to that of the other samples and even superior to that of mechanically exfoliated WS_2. In the case of type C, an emission that was much stronger than others was observed because of the inefficient charge transfer. This relatively weak interlayer coupling and broad FWHM suggest that impurities from the wet-transfer process are the main drawback of the type C heterostructure. The higher peak center for type C is consistent with previous reports of thermally induced strain effect during high-temperature growth;[98] this strain effect is described below. Meanwhile, type B shows a relatively weak emission at lower PL energy (~1.95 eV), which matches the result for bilayer WS_2.[99] This result indicates the growth of few-layered WS_2 and suggests a poor uniformity in the type B heterostructure. On the basis of the aforementioned results, the direct growth with the source contact geometry is the most promising method for preparing high-quality TMD-based heterostructures. For a deeper understanding and evaluation of WS_2 and the heterostructures grown using the source contact geometry, we characterized these heterostructures using various techniques.
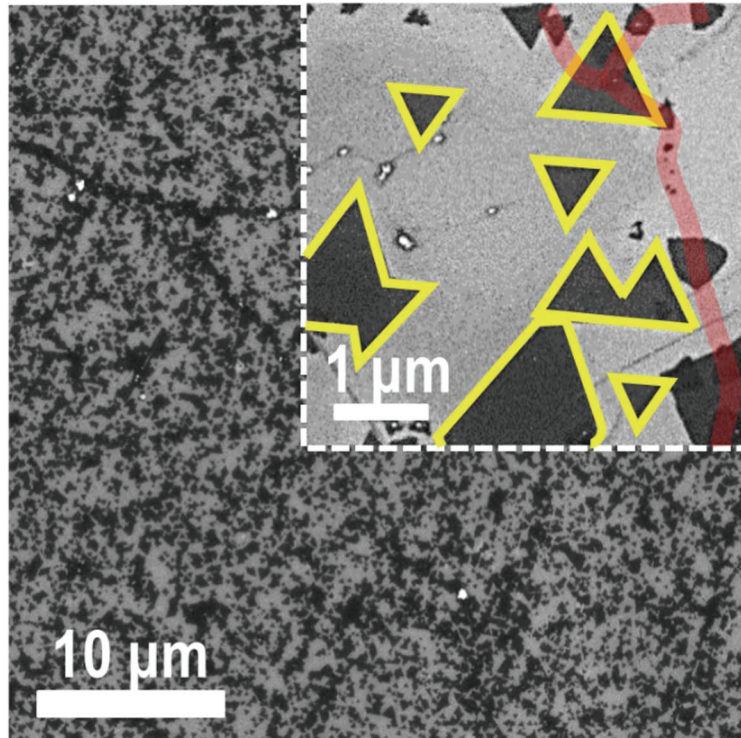
Figure 2.4 SEM image of WS_2 flakes directly grown on graphene using the source contact geometry. Inset is the magnified SEM image.

A representative secondary electron microscopy (SEM) image of the WS_2 flakes grown on graphene is depicted in Figure 2.4. The inset image reveals two types of WS_2 flakes: relatively small irregular flakes nucleated in line (marked with a red line) and large triangular flakes with sharp and parallel edges (marked with yellow lines). Furthermore, the color-coded dark-field transmission electron microscopy (DF-TEM) image shows the presence of WS_2 flakes at various points of growth (Figure 2.5), which could be occasionally found in the samples: such as the basal plane (bordered with the yellow line), seed nanoparticles (marked by the black arrow), graphene wrinkles ~2 nm in height (marked by the blue dotted line), and graphene grain boundaries (GBs) (marked with the red line), as confirmed by SE mode and backscattered SE (BSE) mode SEM images in Figure 2.6. To clearly observe the early stage of the growth, we obtained Figure 2.5 and Figures 2.6 after a reduced growth time (20 min).
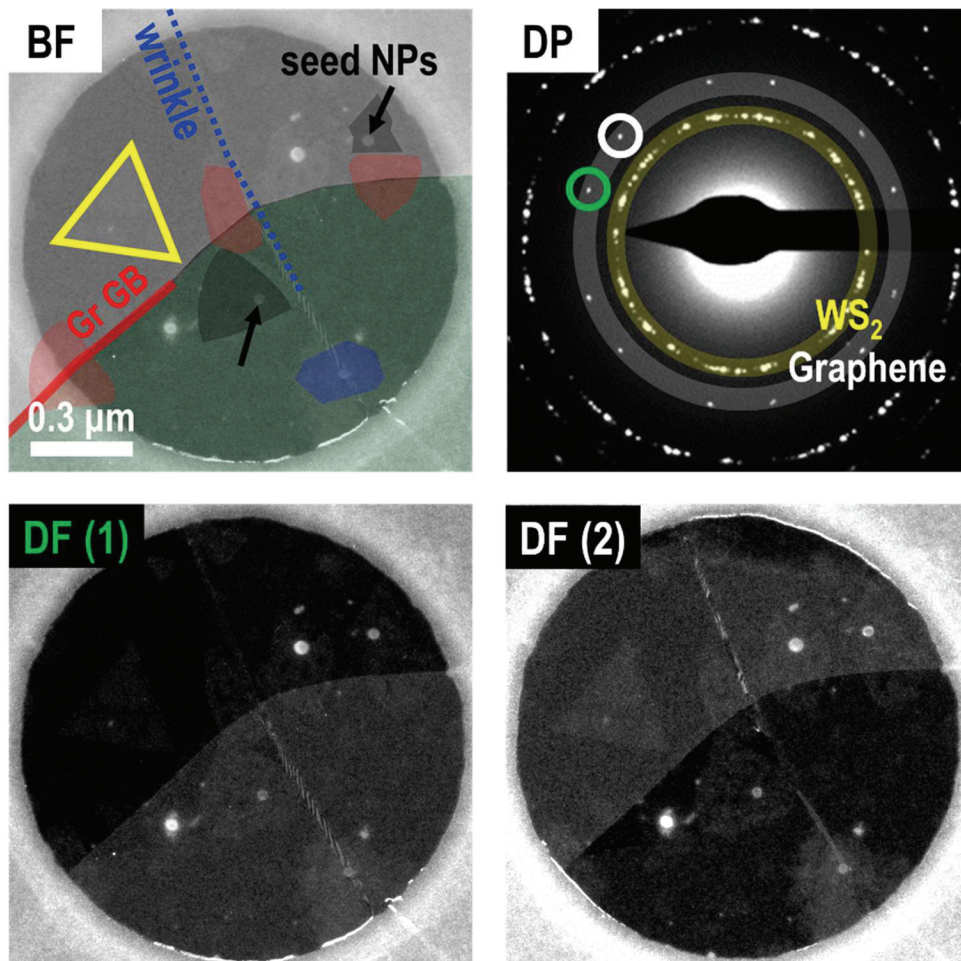
Figure 2.5 Color-coded BF-TEM image, SAED pattern, and DF-TEM images (corresponding to the white- and green-circled diffraction spots) of WS_2 grown on graphene, which show the presence of WS_2 flakes on various points of growth.
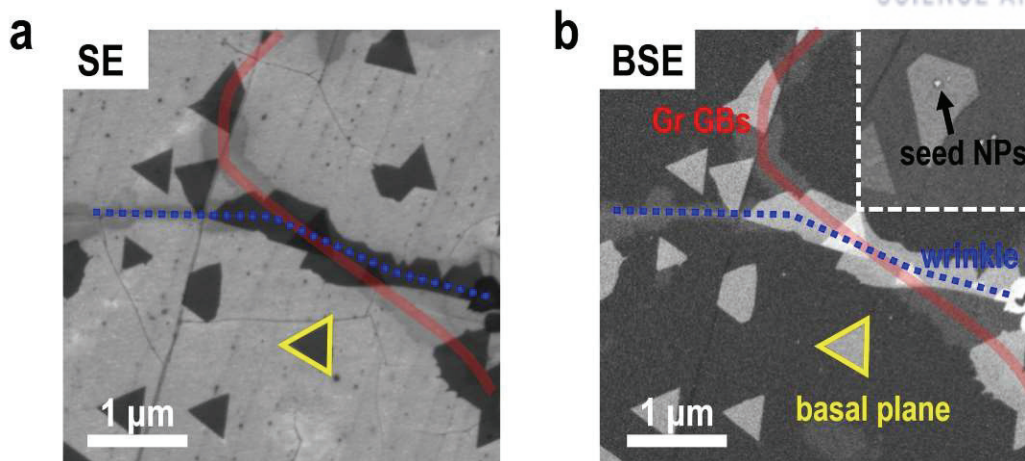
Figure 2.6 (a) SE mode and (b) BSE mode SEM images of WS_2 flakes grown on graphene using a shorter growth time (20 min).

So far, the nucleation and growth processes on the basal plane of graphene are known to proceed with great difficulty because of the weak van der Waals energy.[100] Instead, the structural line defects of graphene (*e.g.,* wrinkles or GBs) are viewed as prevalent nucleation sites for common growth and adsorption because of the higher reactivity of the strained sp^2 bond and exposed dangling bonds.[101, 102] However, the large binding energy of those defect sites is intimately related to a high diffusion barrier, which further hinders growth on graphene. In addition, the large roughness of wrinkles makes the growth difficult and inhibits the van der Waals epitaxy,[103] which is the basic growth principle of the 2D heterostructure. As a result, in previous reports on the direct synthesis of TMDs on graphene, the limited coverage and limited size of flakes with irregular edges were unavoidable because of the preferential adsorption onto the structural line defects of graphene.[104] This phenomenon is consistent with the WS_2 flakes on the red line in the inset of Figure 2.4. Nevertheless, in our growth geometry, a high portion of relatively large and parallel triangular flakes were initiated on the graphene basal plane without certain structural defects, as shown in Figure 2.4 and 2.5. This result can also be explained by the merits of the source contact geometry. Similar to the results of Subhedar *et al.*'s study on graphene growth, the closely contacted geometry may trap the applied sources and flux in the interlayer space. As a result, during the whole growth time, the slow accumulation of evaporated WO_x and S vapor can behave quasi-statically on the graphene surface. The vapor in this configuration is more highly concentrated than those of opened geometries, such as type B in Figure 2.3a, and where the distance between the source and substrate is substantial.[105] A high surface concentration is known to facilitate nucleation through supersaturation; therefore, nucleation and growth of WS_2 flakes likely occur equally at flat surfaces and defective sites.[106] Furthermore, the relatively large domain size of the basal plane, unlike the case of initiation at defect sites, enabled the enhanced coverage; we consequently obtained a nearly complete WS_2/Gr structure by decreasing the distance between the WO_x assembly and the S powder (Figure 2.7).
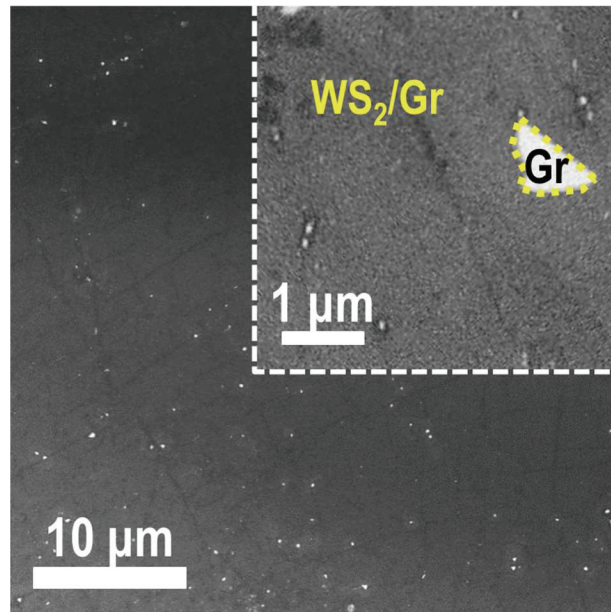
Figure 2.7 SEM image of the fully grown WS_2/Gr heterostructure generated by narrowing the distance between the WO_3 assembly and S source. Inset is the magnified SEM image.

The inset of Figure 2.7 shows a magnified image of the fully grown WS_2, revealing the contrast with the underlying graphene layer (the bright region bordered with a yellow dotted line). This result exemplifies the exceptional coverage of the TMD/Gr 2D heterostructure obtained with the direct growth method. To clarify the merits of the source contact geometry in terms of the growth on an inert surface, we conducted a comparative study with the evaporation of WO_3 powder in the opened geometry (type B) under the same conditions. As expected, the density of the WS_2 flakes substantially decreased and the irregularly shaped WS_2 was attained following the structural line defects of graphene (Figure 2.8).
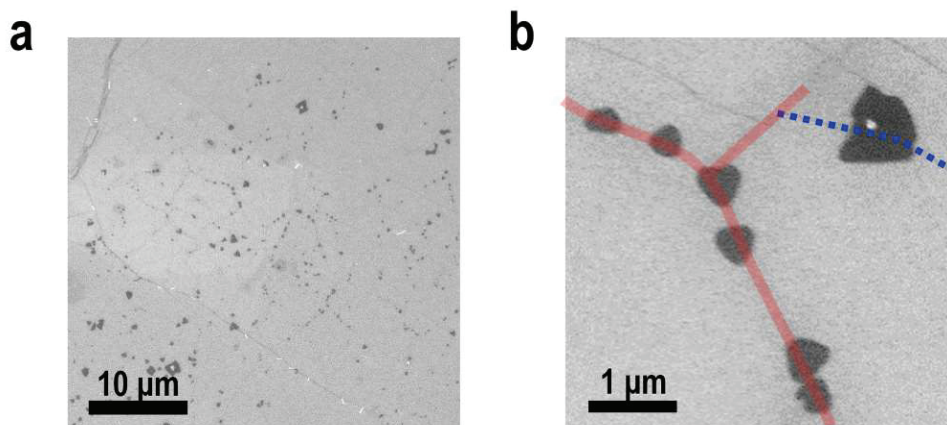
Figure 2.8 (a) Representative SEM images of the WS_2/Gr heterostructure obtained using the powder evaporation method (type B in Figure S1a). (b) A high-magnification SEM image of (a).

Figure 2.9a shows an atomic force microscopy (AFM) image and height profile of the WS$_2$ flakes. Most of the triangular WS$_2$ exhibited little color contrasts, consistent with the uniform thickness. The height profile along the white-dashed arrow indicates a thickness of ~0.8 nm, suggesting the formation of monolayer WS$_2$. Raman spectroscopy was also conducted; the spectrum is presented in Figure 2.9b. This spectrum shows the unique in-plane E$^1_{2g}$ (356.3 cm^{-1}) and out-of-plane A$_{1g}$ (419.1 cm^{-1}) vibration modes of WS$_2$ with a frequency difference of ~62 cm^{-1} between E$^1_{2g}$ and A$_{1g}$, which corresponds to that of monolayer WS$_2$.[107] Figure 2.9c shows a typical PL spectrum for evaluating the thickness and quality of WS$_2$. It shows a distinct emission at 1.98 eV, which well matches the previously reported bandgap of monolayer WS$_2$. Furthermore, the sample emitted a very symmetric and narrow PL peak, without a low-energy tail, suggesting that the emission from neutral excitons is stronger than that from charged excitons. Thus, these results indicate a dominant population of neutral excitons and the growth of high-quality WS$_2$ with low densities of defects and charged impurities.[108]
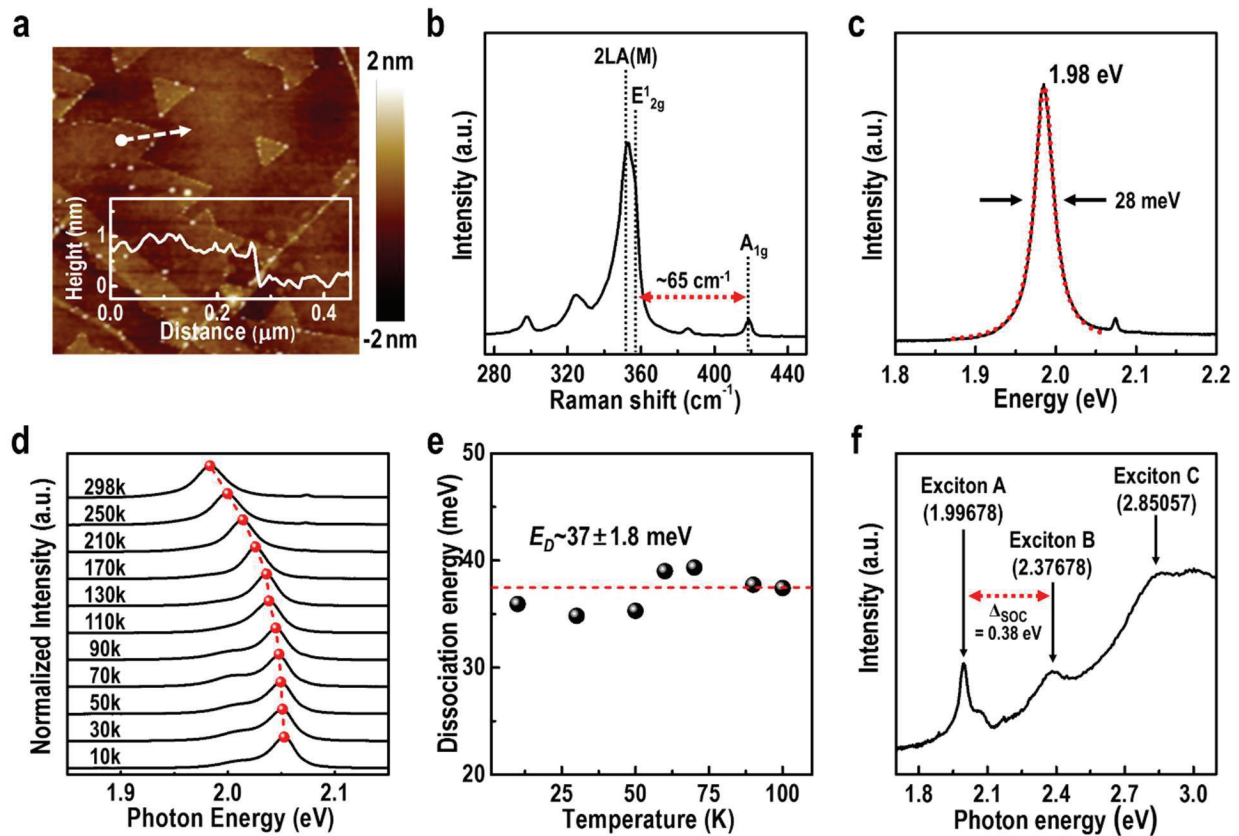
Figure 2.9 (a) An AFM image, (b) Raman spectrum, and (c) PL spectrum of WS$_2$ grown on graphene. (d) The temperature dependence of the PL from 10 to 298 K. (e) The dissociation energy obtained from the measured temperature dependence PL in (d), and (f) the absorbance spectrum.

The temperature dependence of PL spectra is a helpful tool for studying the structural defects in crystals. Figure 2.9d presents the normalized PL spectra of WS_2 grown on graphene; the spectra were collected at temperatures from 10 to 298 K. Consistent with the spectra of common semiconductors, the spectra show an upshift of the peak position and a sharper peak width with decreasing temperature.[109] Below 100 K, the spectra contain an emission peak from trions (charged excitons, X^-) in addition to that from neutral excitons (X^o). A dissociation energy of 37 ± 1.8 meV is deduced from the splitting value between X^o and X^- as a function of temperature in Figure 2.9e; this result agrees well with previously reported values.[110] Otherwise, the defect-related levels in previous reports[111] are not observed, even at high temperatures. This fact indicates that our WS_2 sample grown on graphene has minimal charged impurities and defects. The absorbance in Figure 2.9f exhibits three distinct peaks related to the characteristic excitons from direct transitions at the K point (exciton A and B)[112] and from the optical transitions between the valence band and the conduction band (exciton C) of WS_2.[113] The energy difference between exciton A and B is ~380 meV, which is attributed to the energy splitting induced by the spin-orbit coupling.[114]

Another striking feature is that most of the WS_2 flakes have parallel edges with a specific rotation angle on individual domains of graphene (as marked with the yellow lines in Figure 2.4). This observation indicates that the growth of WS_2 flakes was epitaxial, following the most energetically preferred orientations on graphene. To study in detail the lattice orientations and atomic structure of WS_2 on graphene, TEM was employed for examining various regions of the sample (Figure 2.10). Figure 2.10a shows a representative bright-field (BF) TEM image of a WS_2 flake and graphene supported on an Au TEM grid. The selected-area electron diffraction (SAED) pattern of the triangular flake in Figure 2.10a was collected, as shown in Figure 2.10b. Two sets of well-arranged six-fold symmetry diffraction spots indicate the good quality and the single crystallinity of both crystals. The six spots of the inner set (marked as '1') correspond to WS_2 ($a = 0.272$ nm), and the six spots of the outer set (marked as '2') correspond to graphene ($a = 0.213$ nm). These two sets of diffraction spots are well-aligned in the same orientation. Generally, it is difficult for two highly mismatched lattices to commensurate their lattice orientations because of the large induced strain between the two layers. Nevertheless, it is possible because all of the remaining strain is expected to be accommodated in the van der Waals gap, which is called van der Waals epitaxy.[100] We recorded DF-TEM images by setting the aperture to WS_2 (Figure 2.10c) and graphene (Figure 2.10d) diffractions in the SAED pattern. Notably, a clear and uniform contrast of the entire triangular flake indicates that the grown WS_2 flake consists of a single domain with no misoriented or defective regions. In addition, a typical high-resolution (HR) TEM image (Figure 2.10e) shows the periodic hexagonal arrangement of WS_2 atoms and the absence of any observed atomic defects or voids. These observations support the high quality and single crystallinity of triangular WS_2 flakes grown on graphene.
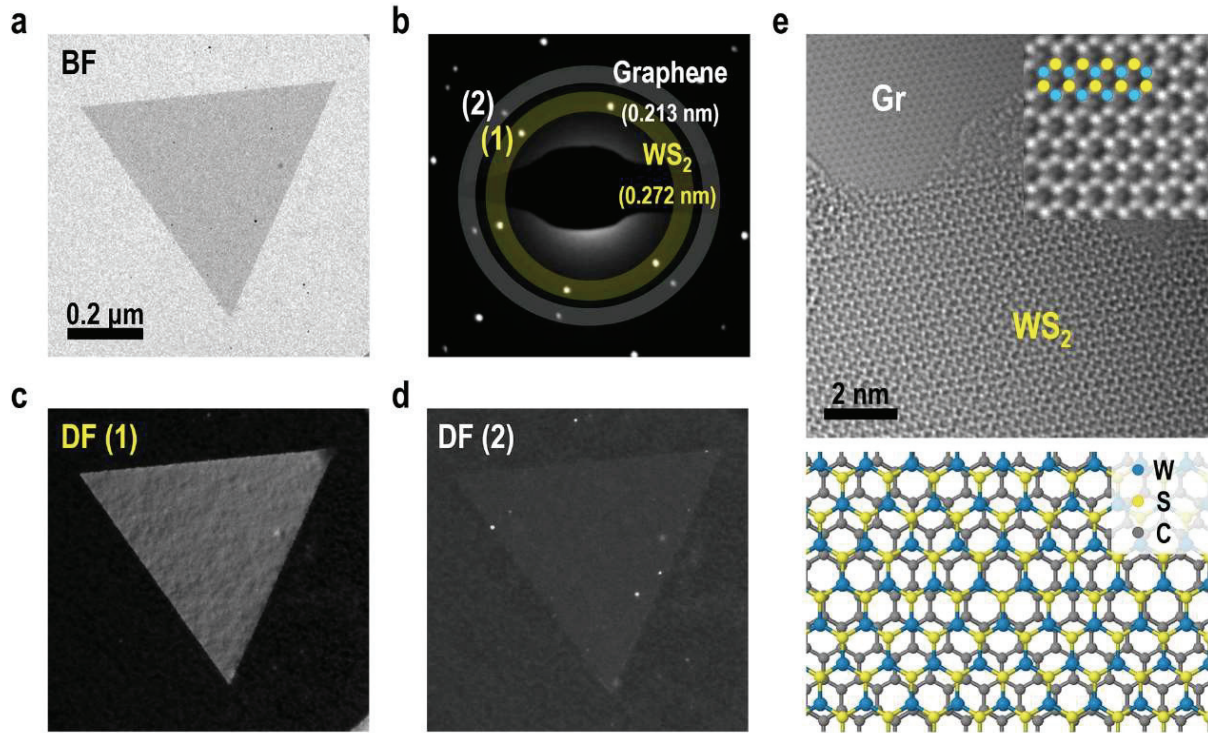
Figure 2.10 Crystallinity investigation and growth study of WS_2 on graphene. (a) A BF-TEM image, (b) SAED pattern, and (c, d) DF-TEM images of WS_2 grown on graphene. The two DF images were obtained by setting the aperture to colored diffraction spot (c) 1 and (d) 2 in the SAED pattern. (e) A HR-TEM image and atomistic model of the WS_2/Gr heterostructure.

2.4 Additional Strategies for Enhancing Lateral Growth of TMDs on Graphene

The thin film growth mechanism depends on the surface energy and chemical potentials of the deposited layers and their substrates.[115] When the surface adhesive force is stronger than the adatom cohesive force, layer growth is preferred. Otherwise, island growth is dominant, since the evaporation of the source during growth is inevitable due to the poor adhesion of the source to the inert substrate. As a strategy for overcoming poor adhesion, certain substances such as graphene-like seeding promoters or salt additives have been increasingly used to promote the layered 2D growth of TMDs.

Especially, salt additives such as alkali metal halides (NaCl, KI, and KCl), sodium cholate, and NaOH have been increasingly used to promote the growth of TMDs. Initially, alkali metal halides were proposed to decrease the high growth temperature of TMDs. Li *et al.* reported that various alkali metal halides react with TM oxides to form volatile TM oxyhalide species, thereby promoting the transport of TM to the growth substrate.[7] In addition, remarkably suppressed nucleation in the presence of alkali metal halides was observed.[9, 116] Kang *et al.* assumed that alkali halides would reduce the concentration of water in the vapor-phase environment of the MOCVD system encouraging the 2D growth of nuclei.[9] To confirm this, Kim *et al.* investigated the effects of $CaCl_2$ and CaO, which are known to be more effective desiccants than alkali metal halides, but they did not observe significant suppression of nucleation density.[116] This result inferred that alkali metal halides act as seeding promoters (not as a dessicant) and increase the lateral size in the growth stage, since their geometry can stabilize the 2D nuclei of TMDs. Consequently, it was confirmed that alkali metals play a role not only in suppressing nucleation but also in promoting adsorption of Mo in the pre-exposure step.
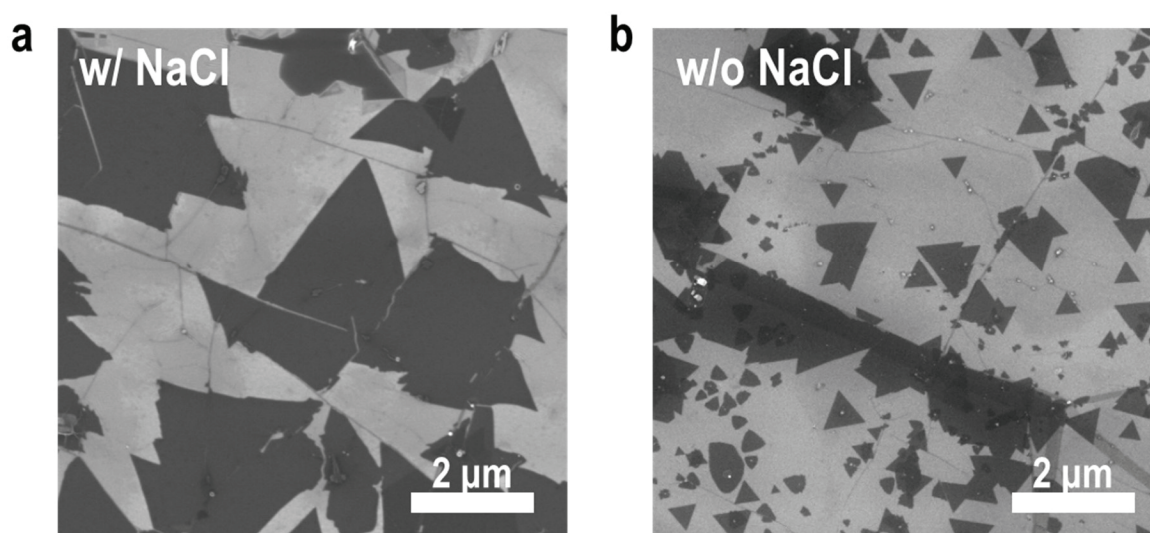
Figure 2.11 (a,b) SEM images of the MoS_2 monolayer grown onto graphene (a) with and (b) without NaCl, respectively.

To increase the flake size of TMDs on graphene for practical applications with easy handling, NaCl, one of alkali salts, has tried to introduce into the growth process. Figure 2.11 shows SEM images of MoS_2 flakes grown on CVD-grown graphene with NaCl. In 10 minutes, which is very short compared to the previous one, we could see the average flake size and area increased by more than three times. However, the deposition of alkali-metal residual particles or layers onto the substrate surface is unavoidable. Figure 2.12 is SEM images of MoS_2 layer grown onto SiO_2 substrate using NaCl as an additive. Residual salt crystals of various sizes remain below the MoS_2 layer and cause wrinkles to MoS_2 layer. In addition, the optical images in Figure 2.13 also show that MoS_2 layer is completely gone when it is dipped in water. This suggests that a water-soluble residual layer is formed under MoS_2 during the growth process, and XPS spectra (Figure 2.14) clearly shows a strong Na 1s, also suggesting that NaO_x or NaS_x layer is deposited on the SiO_2 surface.
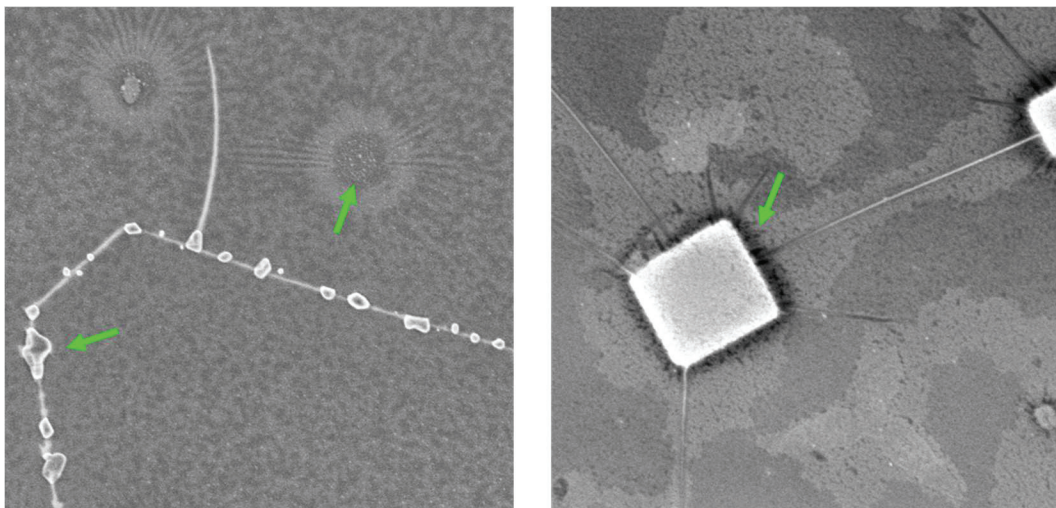
Figure 2.12 SEM images of the residual salts remaining with MoS_2 layer grown with NaCl.
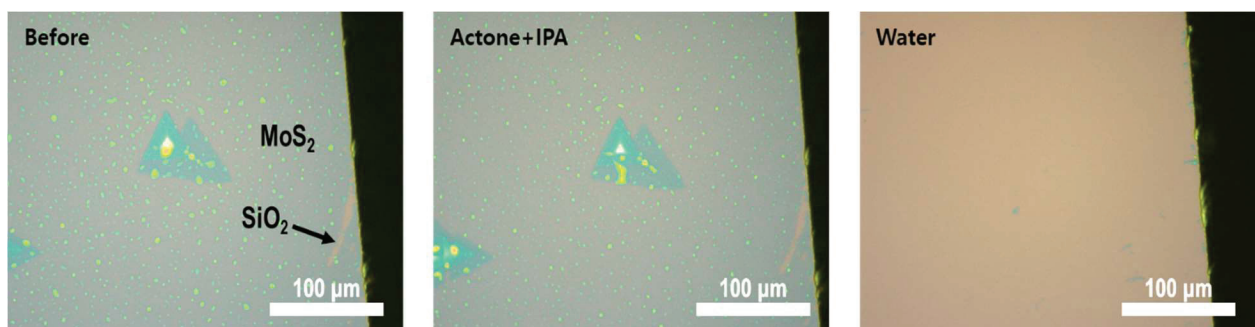
Figure 2.13 Optical images of MoS_2 after immersed in Acetone and IPA, and immersed in water, respectively.
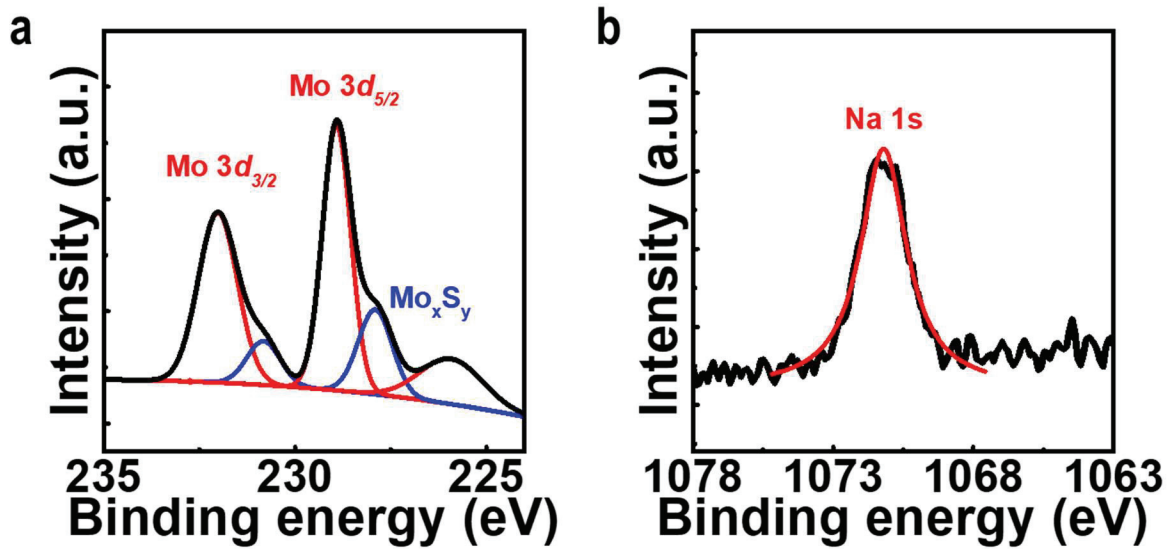
Figure 2.14 XPS spectra of the as-grown MoS_2 flakes using NaCl additives. (a) Mo 3d and (b) Na 1s core-level peak of MoS_2 flakes, respectively.

Due to the complexity of the CVD process, the underlying mechanism or role of alkali metal halides has not been clearly established. Furthermore, there is also a concern that the introduction of alkali metal halides may lead to the formation of impurities and loss clean interfaces, which may affect the electron and photon characteristics of composite semiconductors.[9, 116] In addition, alkali metals such as potassium (K^+), can cause degenerate doping of TMDs.[117] Thus, a large area heterostructure synthesis using alkali metals requires a deeper understanding of the roles and mechanisms of alkali metal halides, including negative effects, and future works are also needed to discover other new strategies.

2.5 Summary and Outlook

By virtue of their natural sizable and tunable bandgap,[4, 33, 34] 2D TMDs can potentially serve as a viable nanotechnology or semiconductor fabrication platform with multiple physical features for applications ranging from fundamental research to future optoelectronic and electronic applications. The diversity of TMD materials (with around 40 different types of compounds) and their versatile and tunable properties permit a wide degree of control for designing efficient and on-demand heterojunction devices.[3] Lately, layer-by-layer stacking of monolayer MX_2 and Gr has aroused more scientific concerns. Many intriguing physical issues have been detected in such heterostructures, and novel devices (tunneling transistors and light-emitting diodes, etc.) with unprecedented performance have been constructed.

The construction of MX_2/Gr vertical heterostructures with clean interfaces is prerequisite for preserving their unique properties. For the moment, layer-by-layer stacking of mechanically exfoliated MX_2 and Gr with scotch tapes is commonly used for the heterostructure construction.[118] However, this method usually leads to the adsorption of polymeric impurities, primarily at the heterostructure interfaces, and affords little control over the film thickness and domain size (MoS_2 and Gr), undoubtedly resulting in degrading device performances.[119] In this regard, it is logical to develop a reliable synthetic approach for directly obtaining large-scale, thickness controllable/uniform, and high quality MX_2/Gr vertical heterostructures.

In summary, by exploiting an all-CVD approach, we developed an optimized CVD-based method for the synthesis of high-quality TMDs and TMD/Gr heterostructures with highly enhanced coverage. Especially, by introducing source contact geometry, we achieved a uniform nucleation of TMD flakes with minimal charged impurities and defects, even on the inert graphene basal plane. This uniform nucleation results in a genuine van der Waals epitaxy without the interruption of locally strained defect sites and also promotes charge transfer between the two layers because of the uniform contact throughout the interface. The availability of large scale MX_2-graphene heterostructures will stimulate investigations into photonic, electronic, and spintronic properties of this new structure and will be a benefit to the scientific community.

CHAPTER 3

Air-Stability Enhancement of TMDs depending on the Substrate

3.1 Environmental Stability of TMDs

Unlike the fast degradation of black phosphorus in air,[120] TMDs have been considered as air-stable semiconductors under ambient conditions.[121] However, some reports indicate the decomposition of TMDs in extreme conditions such as temperatures above 250 ° C and exposure to ultraviolet light, heat and moisture.[122] In recent study, severe surface degradation has occurred through preferential oxidation along the less stable grain boundaries (GBs) and crystal edges during long-term observations of the surface of MoS_2 and WS_2 flakes exposed to air.[123] This result motivated that the weak air stability of TMDs and improvement strategy have attracted considerable attention because stable device fabrication and operation is required for most applications under ambient environmental conditions.

Prior efforts at shielding TMDs from the environment have been primarily motivated by the need to prevent molecular adsorbates and charge traps from affecting the carrier mobility of TMDs. In one approach, Gao *et al*. introduced polymer-based encapsulation methods and demonstrated delayed aging of these materials.[123] However, not only does the inevitable water permeability of polymer films disturb the thorough protection by causing distinct degradation after a year,[124] but polymer encapsulation can also add another restriction on some applications such as by demanding high temperature conditions. Moreover, to prevent surface contamination with adsorbates, a few studies have suggested the use of surface shielding methods, such as the transfer of h-BN layers[125] and metal oxide deposition via atomic layer deposition.[120] However, these methods are also imperfect because of limitations such as crack generation under strain or the inevitable contamination during the encapsulation process.[126] Therefore, it is important to find a new pathway towards air-stable TMDs.

In this chapter, based on the observed oxidation behavior of 2H-phase TMDs using $MoTe_2$ single crystals, increasing the quality of fabricated TMDs might be key for enhancing their stability. In ongoing studies for developing high-quality monolayer TMDs, the growth substrate is regarded as the most important factor. In particular, many studies have identified graphene as an ideal substrate for high-quality TMDs.[127] In this light, compared to the common short-term degradation of TMD flakes grown on SiO_2/Si substrate (representatively, WS_2/SiO_2), we investigated the air stability of WS_2 grown on graphene (WS_2/Gr) and confirmed the predicted relation between defects and the aging phenomena. Furthermore, electron microscopy images, x-ray photoelectron spectroscopy (XPS), photoluminescence, and Raman spectra collected over 300 days suggest that graphene plays a unique role by obstructing the air degradation. By demonstrating the direct growth of high quality and highly stable TMDs on graphene and proposing the consistent contribution of the charge transfer effect to the prevention of aging, our work can pave the way for practical TMDs applications with optimized performance.

3.2 Air-Degradation Observation of 2H Phase TMDs

3.2.1 Sample Preparations

Growth of 2H-MoTe$_2$ Crystals

A more detailed procedure for the synthesis of MoTe$_2$ crystal has been described in elsewhere.[17] MoTe$_2$ single crystal was selected as a representative material for the analysis of oxidation behavior of 2H-TMDs for long time tracking in ambient air condition. For the synthesis of 2H-MoTe$_2$ single crystal, the growth experiments were carried out using Te-rich eutectic metal alloys as a Te reservoir. This Cu/Mo/substrate multilayer sample in conjunction with Te powder (~0.1 g) was then sealed in a quartz tube filled with inert Ar gas (500 sccm) and simply heated for 10 min at 600°C. During crystal growth, a Cu film functions as a Te reservoir by forming a liquid-like, Te-rich eutectic alloy, *i.e.* Cu$_x$Te$_y$(l), which prevents the Te deficiency in the resulting MoTe$_2$ crystal. This characteristic allows M atoms to effectively diffuse into the Cu$_x$Te$_y$ matrix during growth and then to rapidly react with sufficient Te atoms, leading to the formation of high-yield, single-crystalline nanostructures of MoTe$_2$ within the Cu$_x$Te$_y$ droplets. Following the growth, the by-products related to various Cu$_x$Te$_y$ phases were completely etched away using a 1M ammonium persulfate (APS) aqueous solution leaving behind high-density MoTe$_2$ crystal on the substrate.

Characterizations

Using HR-TEM imaging and SAED analysis on a MoTe$_2$ crystal of a BF-TEM image in Figure 3.1a, as-grown MoTe$_2$ crystals were shown to be single-crystalline 2H structures (Figure 3.1b and 3.1d-f). Also, by comparing relative angles in three SAED patterns obtained from different regions in a crystal, we confirmed that as-grown crystals were also single-crystalline. The combined TEM-EDS studies (Figure 3.1c) confirm that Mo$_x$Te$_y$ crystals are highly stoichiometric with an atomic ratio of (x:y) ~ (1:2).

Transfer

To avoid the effect from residual metal film used for growth process, as-grown MoTe$_2$ crystals were transferred on the target substrate. We used an all-dry transfer method that relies on viscoelastic PDMS stamps to avoid external contamination of the fabricated structures and crystals were transferred with this method without employing any wet chemistry. At first, the piece of PDMS is gently placed and pressed on the substrate with MoTe$_2$ crystals. In order to transfer the flake to the acceptor surface, the PDMS is pressed against the surface and it is peeled off very slowly. After PDMS stamp is aligned to the target substrate, a simple pressing step make to release the MoTe$_2$ crystal, as shown in Figure 3.2.
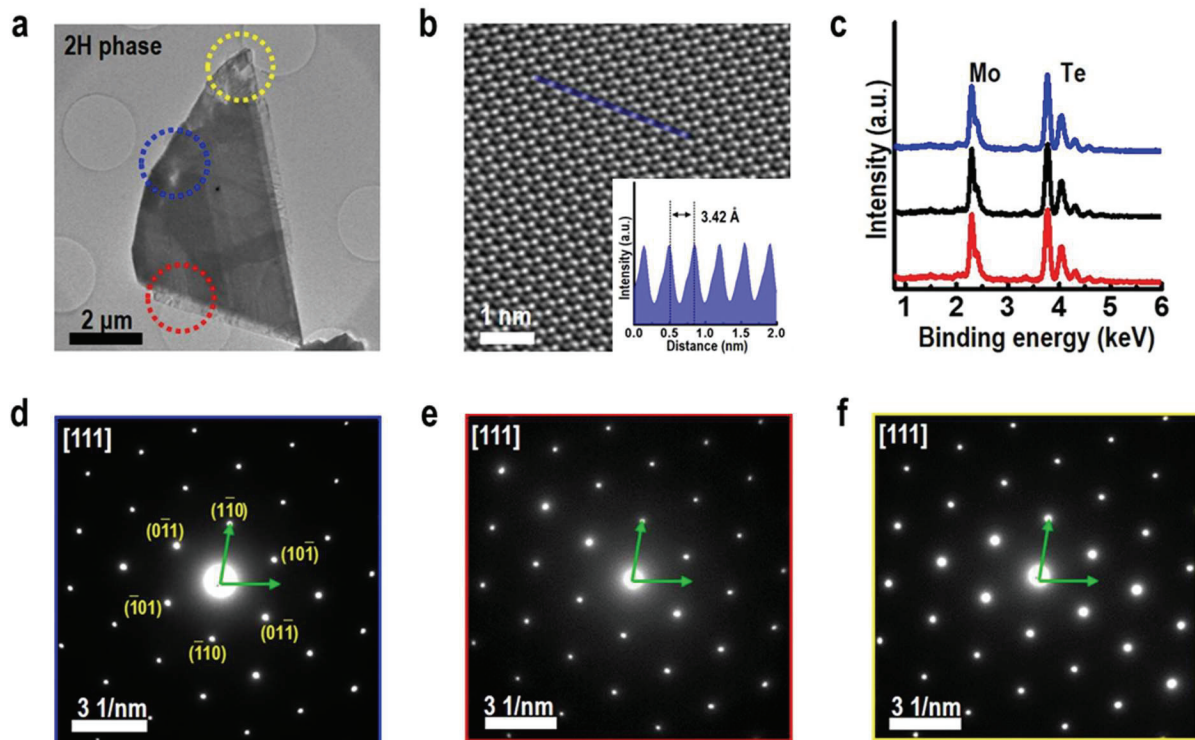
Figure 3.1 TEM and EDS results of 2H-MoTe$_2$ crystals. (a) A BF-TEM image and (b) corresponding atomic resolution image of MoTe$_2$ crystal. Inset: Intensity line profiles taken from a blue line in (b). (c) EDS spectra taken from several MoTe$_2$ crystals. (d)-(f) SAED patterns taken from (d) blue-, (e) red-, and (f) yellow-dotted circles in (a), respectively. Reproduced from ref [6].
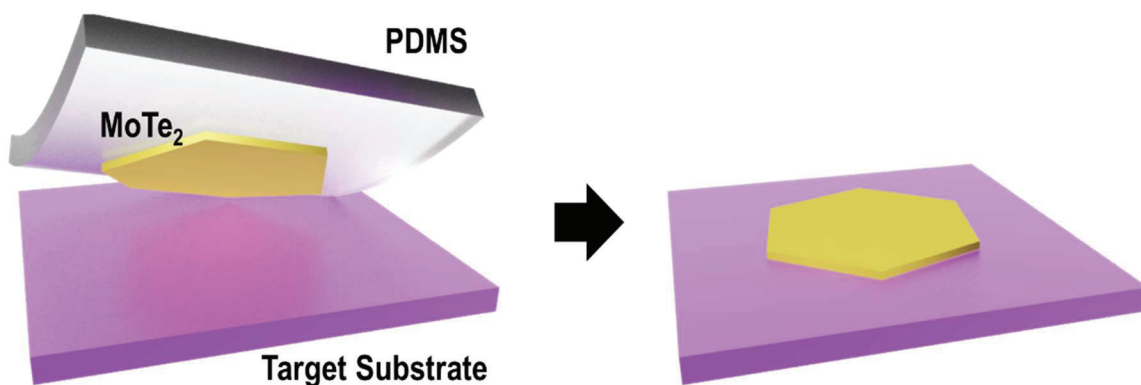
Figure 3.2 Simple schematic illustrations showing a dry transfer process of MoTe$_2$ crystal to the target substrate using PDMS.

3.2.2 Tracking Air-Degradation Behaviors of 2H TMDs Crystals

As-grown 2H-MoTe$_2$ crystals on SiO$_2$/Si were fabricated with size of tens of micrometers, as shown in Figure 3.3a. The BSE mode SEM image in Figure 3.3b present that the surface of as-grown crystal is uniform and clean. However, after being stored at room temperature (~25 ℃) without desiccant (relative humidity ~40%) for 3 months, a significant surface degradation with triangular or hexagonal pits was observed as shown in Figure 3.3c. Several shallow pits also can be found on the surface through the zoomed-in BSE image (Figure 3.3d), although they are not observed in the SE image. This degradation phenomenon was observed to be progressively worse over time as shown in Figure 3.3e and f.
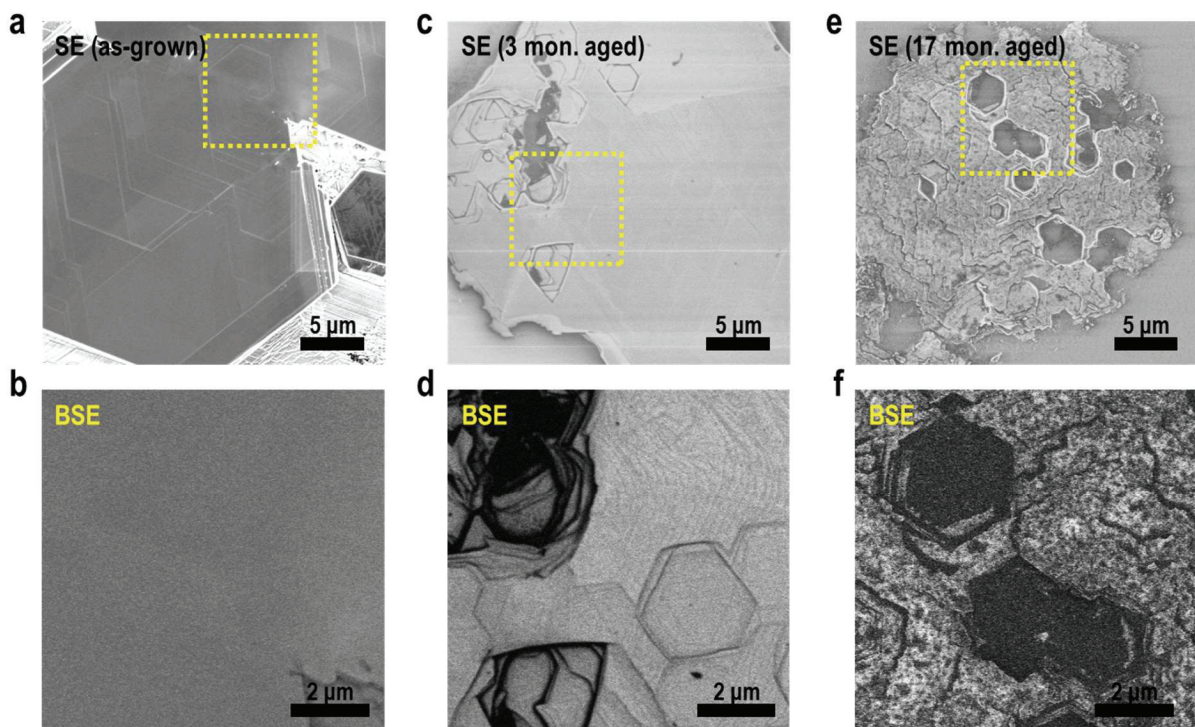
Figure 3.3 (a-f) SE and BSE mode SEM images of MoTe$_2$ crystal in time sequence. BSE mode images (b,d,f) are the zoomed-in surfaces obtained from each yellow box in SE mode images (a,c,e).

In particular, by observing many samples, it was confirmed that the degradation phenomenon occured faster and more severely in structural defects such as screw dislocation, grain boundary and crystal edges (Figure 3.4a-c). In addition, it can be estimataed that the etch pits of surfaces that are not directly associated with structural defects were caused around vacancy defects (red arrow in Figure 3.4c). To study the expansion of these pits, SEM images (Figure 3.4d) from the previous point in time were compared. SE mode SEM image in Figure 3.4d shows that agglomerates forming in hexagonal

and triangular shallow pits (cyan colored lines). In BSE mode image (Figure 3.4e), those agglomerates shows darker contrast compared to homogeneous $MoTe_2$ surface area.
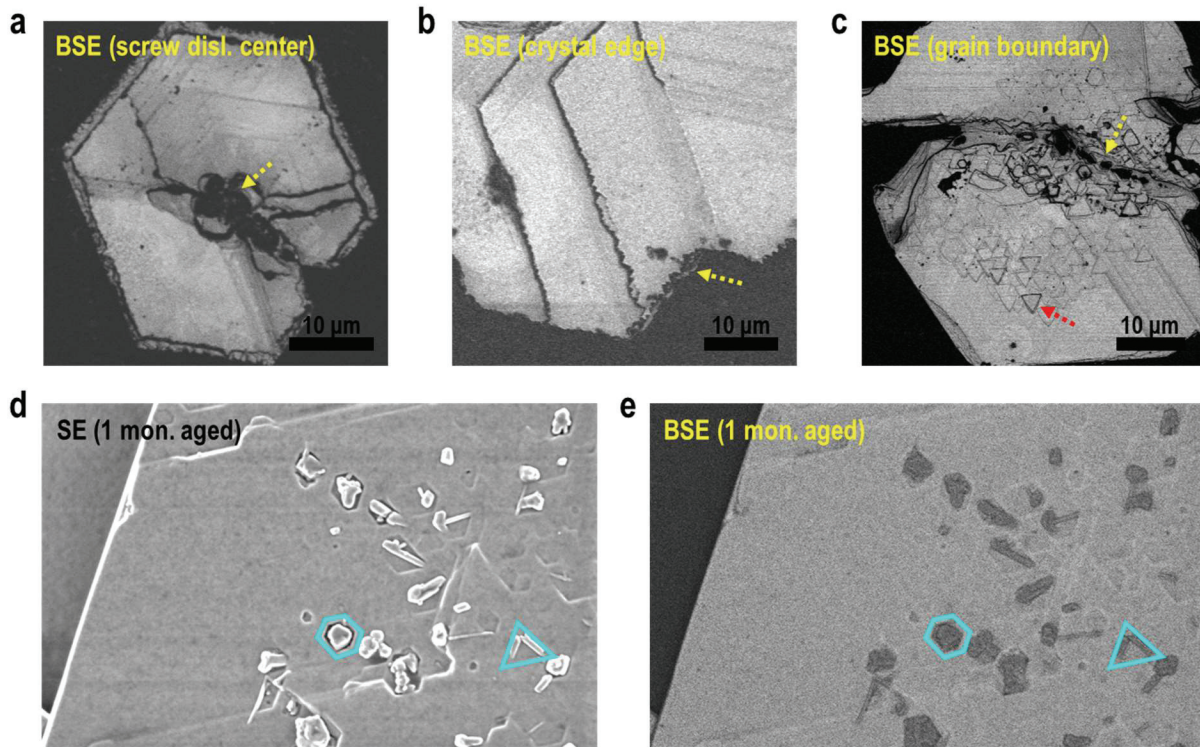
Figure 3.4 (a-c) BSE mode SEM images of severe degradation point on the aged $MoTe_2$ crystals. Each image is a representative image of (a) screw dislocation center, (b) crystal edge, and (c) grain boundary in the crystal. (d,e) SE and BSE mode SEM images on the 1 month aged $MoTe_2$ crystal.

The BSE mode primarily detects elastically scattered electrons formed during interaction between an accelerated electron beam and a sample; therefore, the contrast in a BSE-SEM image is more sensitive to the atomic number (Z) of the sample than to its surface morphology reveals. Therfore, since the heaviest element in $MoTe_2$ is Te which determines the contrast, it can be interpreted that the darker contrast of agglomerates means the relative defficiency of Te. Until now, the mechanism for the loss of chalcogen atom (X) is not clear at this point and will require additional study. One assumption raised in previous study is that O is first bonded to X, followed by breaking of the X–metal bond, followed by substitution of the X by O or OH radicals.[123] The possible reactions are as follows:[128]

$$2MoS_2 + 7O_2 \rightarrow 2MoO_3 + 4SO_2 \qquad (3.1)$$

$$MoO_3 + 2OH^- \rightarrow MoO_4^{2-} + H_2O \qquad (3.2)$$

$$MoS_2 + 9/2O_2 + 3H_2O \rightarrow MoO_4^{2-} + 2SO_4^{2-} + 6H^+ \qquad (3.3)$$
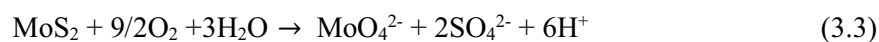
From these result, it can be inferred that degradation process is preferentially initiated and expanded at structurally unstable regions (such as defects and grain boundaries) with O or OH substitution, and then gradually propagated deeply by making agglomerates and decomposing them into air.

Besides, according to above equation (3.1)-(3.3) and based on lower formation energy of chalcogen vacancy,[129] plain surfaces also experience air degradation over time, although it is relatively slow than structural and morphological defect sites. Figure 3.5 presents the BSE-SEM images of the crystal surface in sequence. In these images, dark spots occur over time on the crystal surface that used to have a bright and uniform contrast (Figure 3.5a), and are eventually completely covered as shown in Figure 3.5f. Along with the zoomed-in SE image of Figure 3.6b, an AFM topography image (Figure 3.6a) measured on the same sample in Figure 3.5c shows that those dark spots are triangular shaped hillock with small aggregates (marked by blue arrows) at the center (~2 nm of height). Especially, BSE mode image (Figure 3.6c) indirectly suggested that these small aggregates are the most Te-deficient. These aggregates expand within the triangular hillocks as the degradation intensifies, as shown in Figure 3.6d and e.
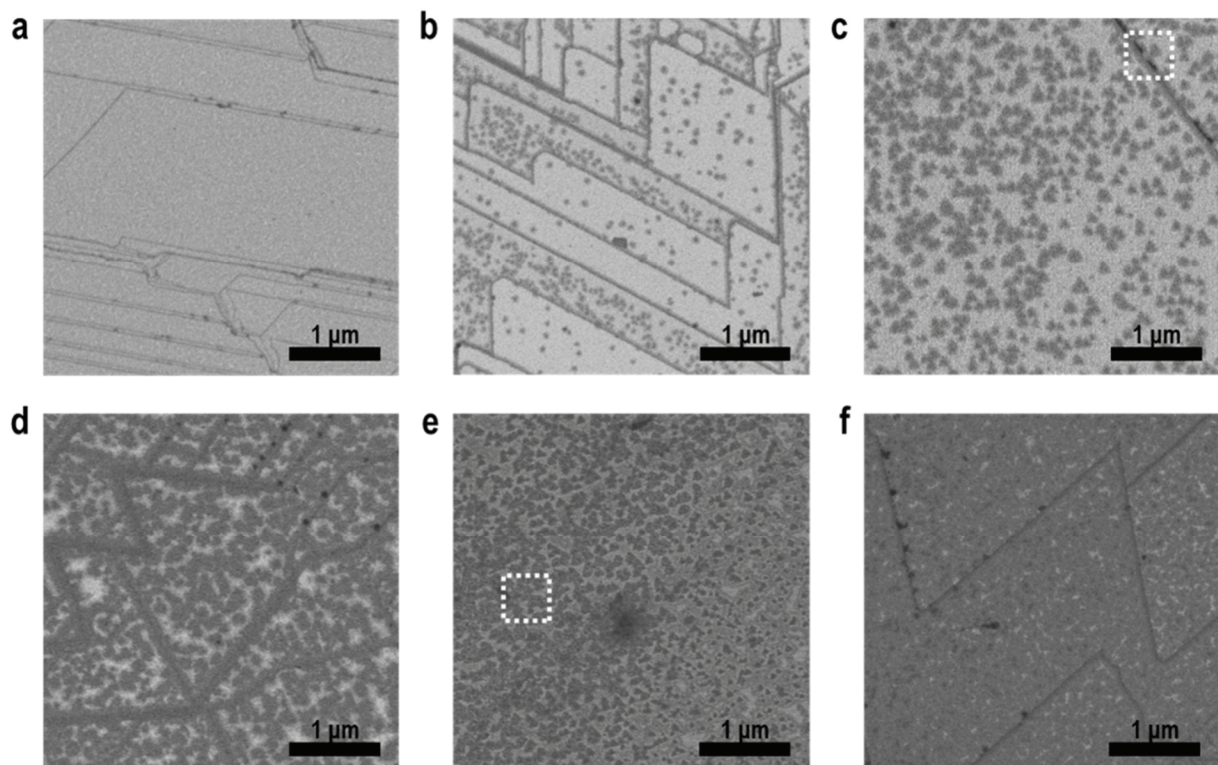
Figure 3.5 (a-f) BSE mode SEM images measured on the surface of MoTe$_2$ crystals in time sequence.
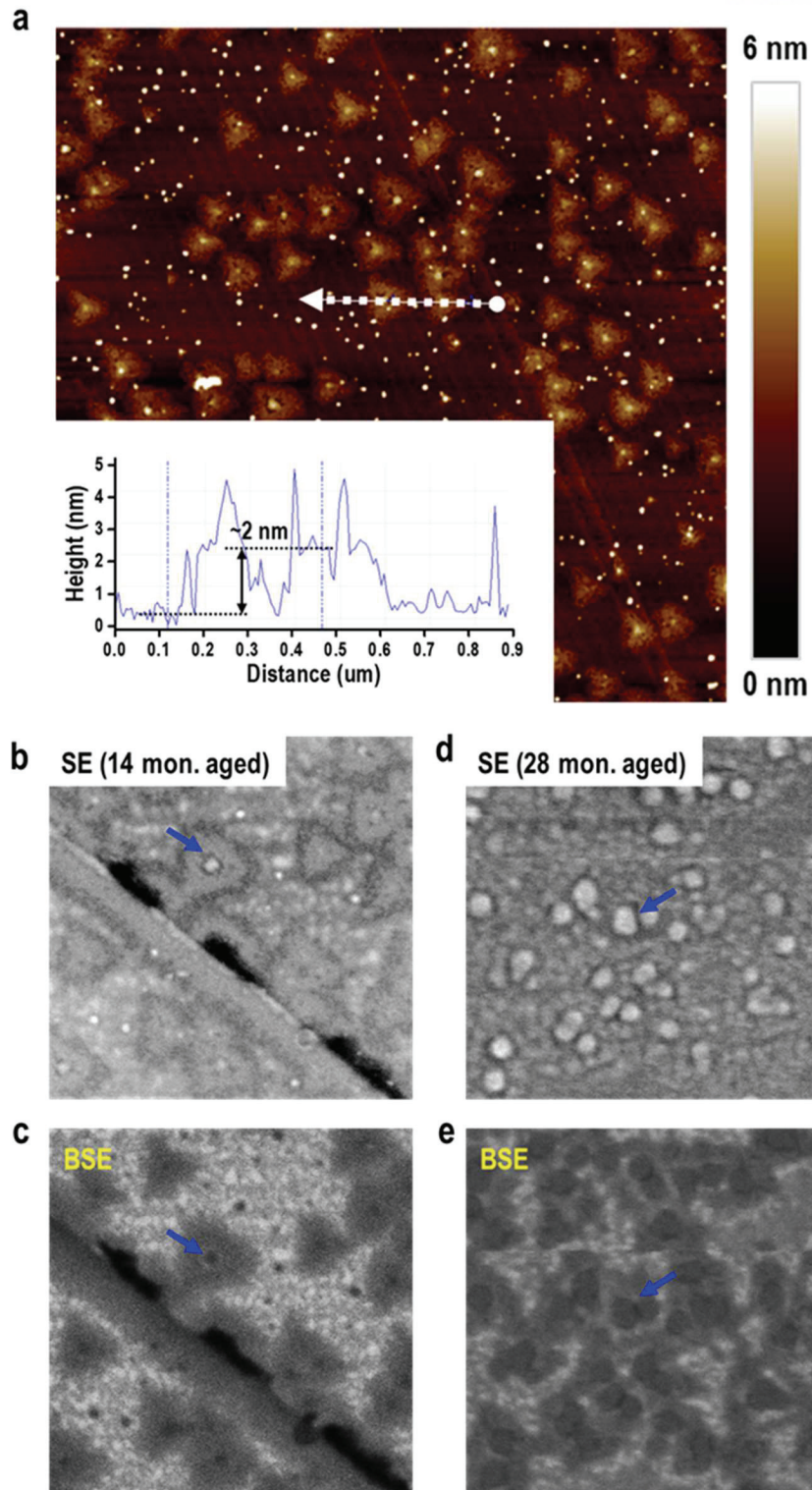
Figure 3.6 (a) AFM topography image and height profile (white dotted line in topography image) measured on the same sample in Figure 3.5c. (b-e) Zoomed-in SE and BSE mode SEM images from white dotted boxes in Figure 3.5c and e, respectively.

3.3 Strategy for Air-Stability Enhancement of TMDs using Graphene Substrate

This chapter was mostly copied from reference [130].

Considering the neutral defects that initiate aging, as predicted in previous chapter, increasing the quality of fabricated TMDs might be key for enhancing their stability. In ongoing studies for developing high-quality monolayer TMDs, the growth substrate is regarded as the most important factor. Thus, we investigated the air stability of this stacked sample (WS_2/Gr) at room temperature in ambient air without desiccant (relative humidity ~40%) and compared the sample with WS_2 flakes grown on a SiO_2 surface. As shown in Figure 3.7a and d (the bordered dot-line is included for easy viewing), both the as-grown WS_2 monolayers on CVD-Gr and SiO_2 have clean and uniform surfaces. After exposure for over 300 days without any encapsulation, the WS_2/Gr samples maintained their uniform surface and pristine atomic lattice (Figure 3.7b and c). However, in the case of the samples grown on SiO_2, severe surface degradation started after only 14 days, which left behind several triangular-shaped holes both on the basal planes and edges of WS_2 and progressed to the complete disappearance of the surface after over 300 days (Figure 3.7e and f).
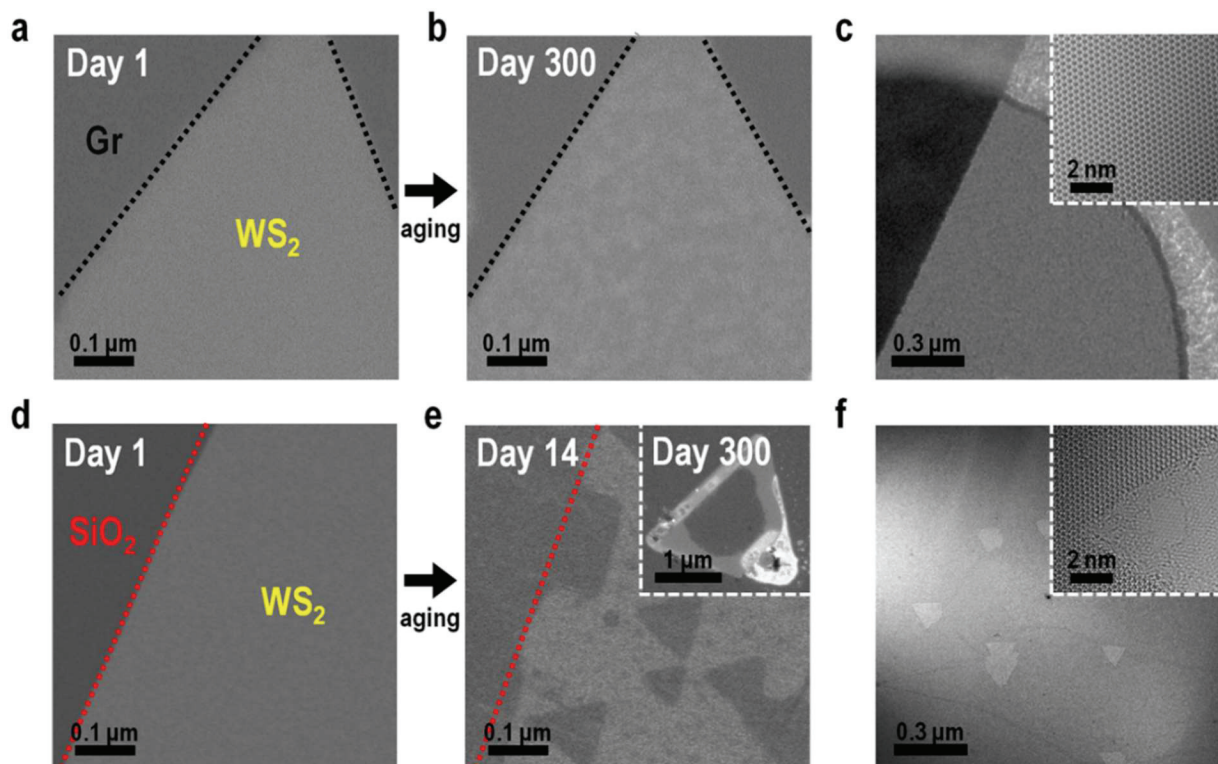
Figure 3.7 (a,b) BSE mode SEM images of (a) as-grown and (b) 300-days-aged WS_2/Gr. (c) Low-magnification TEM image (HR-TEM image in the inset) of the suspended WS_2/Gr (aged for 300 days). (d,e) BSE mode SEM images of (d) as-grown and (e) 14-days-aged WS_2/SiO_2 (aged for 300 days in the inset). (f) Low-magnification TEM image (HR-TEM image in the inset) of the suspended WS_2/SiO_2 (aged for 7 days).

Previous studies have proposed that the surface degradation is mainly initiated at the reactive edges and structural defects of TMDs.[123, 131] However, subsequent experimental and theoretical results to elucidate the concrete mechanism for the aging-related deterioration in TMDs have not yet demonstrated this. To verify the previous prediction and this significant discrepancy in the air-stability of WS_2/Gr flakes, we paid significant attention to the high crystallinity and low defect density of WS_2/Gr flakes. First, we compared the intrinsic defect concentration in both crystals using the defect-related levels in the emission properties of the samples. Figure 3.8a shows a distinct PL emission of WS_2/Gr at 1.98 eV, which matches well with the previously reported bandgap of monolayer WS_2. It has a very symmetric and narrow PL peak (FWHM of ~28 meV) consisting of a single Lorentzian line without a low-energy tail, which indicates that the emission from neutral excitons is stronger than that from charged excitons. Compared to the PL spectra of WS_2/SiO_2 (FWHM of ~51 meV), this result demonstrates that charged impurities and structural defects have extremely small impact on WS_2/Gr. However, the broadening of the PL peak is not only due to the crystal quality, the substrate effect also plays an important role. For dielectric materials, charged impurities in the substrate are closely connected to doping. The high density of charged impurities in SiO_2 may influence the phonon vibration compared to graphene with few charged impurities.[132] However, the WS_2/SiO_2 flakes still show broad PL emission peaks even after they are detached from SiO_2 using HF solution and then transferred onto CVD-Gr substrate (WS_2-tf-Gr). Thus, we can propose that the narrower emission reflects the high quality of WS_2/Gr with a low concentration of defects and charged impurities and excludes the effect of the substrate.[108] In addition, we observe a small PL emission at 2.08 eV, which matches well with the reported 2D vibration mode of graphene (2,680 cm^{-1}) when PL spectra are collected using the 514.5 nm line of an Ar laser as the excitation source.[133]

Apart from the intrinsically generated defects in as-grown crystals, additional defects can be formed and propagated over time by the existence of localized strain within the crystal.[134] Thus, to evaluate the applied local strain in both crystals, we utilized PL and Raman mappings and compared the color contrasts induced from the shifts of each signal. For both the intensity and position mappings, WS_2/Gr shows homogeneous contrast through the entire single flake (Figure 3.8b-c), which contrasts with the inhomogeneous map of WS_2/SiO_2 within a single domain (Figure 3.8d-e). In a previous study, a significant mismatch in the thermal expansion coefficient (TEC) causes a large difference in the contraction between each layers. Thus, since SiO_2 has a significantly smaller TEC (0.60 μ/K) than WS_2 (10.1 μ/K), inhomogeneous tensile strain may be applied to the WS_2 lattice during the cooling process.[98] Though graphene also has a large difference in TEC (-8.0 μ/K), WS_2 is essentially free from friction and lateral strain during the growth process because of the atomically flat surface of CVD-Gr.
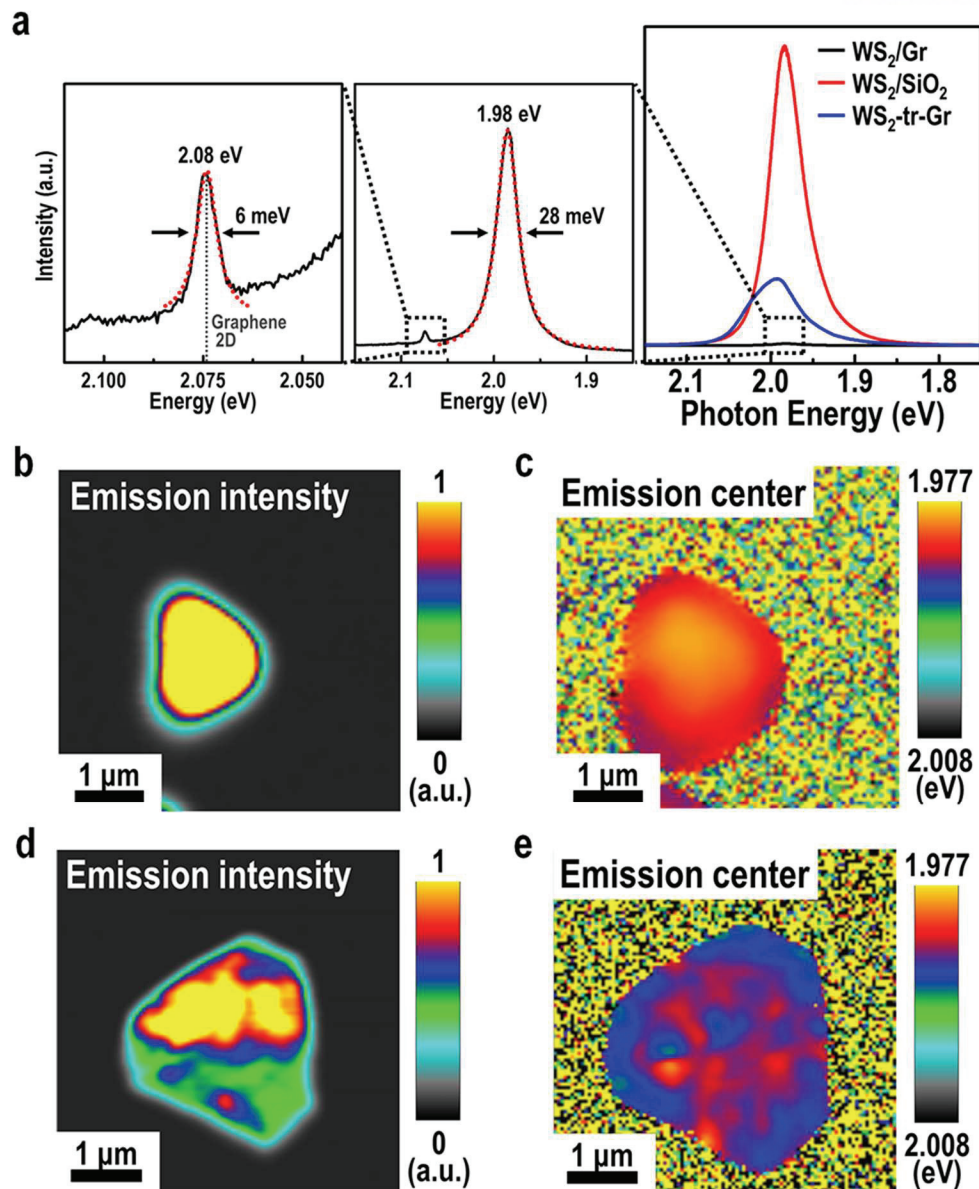
Figure 3.8 (a) PL spectra of WS$_2$/Gr, WS$_2$/SiO$_2$, and WS$_2$-tf-Gr. (b-e) Emission mapping images of (b-c) WS$_2$/Gr and (d-e) WS$_2$/SiO$_2$: (b, d) the intensity maps and (c, e) the position maps of the emission peaks.

Although most of the WS$_2$/Gr flakes exhibit high air stability, as shown above, a partial degradation occurred in a few small flakes after 180 days (Figure 3.9c). Using SEM at various growth points of WS$_2$/Gr (Figures 3.9d-f), we confirmed that those small flakes all nucleated at the structural defects (*e.g.,* wrinkles or GBs) of graphene. However, the large binding energy of those defect sites is intimately related to a high diffusion barrier, which further hinders their growth on graphene. In addition, as noted in a recent report, the structural defects of the substrate layer can promote a structural disorder in the overlayer during growth.[100, 135] Unlike the basal plane, the locally strained C-C bonding of a structural

defect can strongly influence the crystal quality of the overgrown WS_2 flakes. These results imply that high crystallinity with extremely low density of intrinsic defects and negligible spatial strain play a significant role in the excellent air stability of WS_2/Gr.
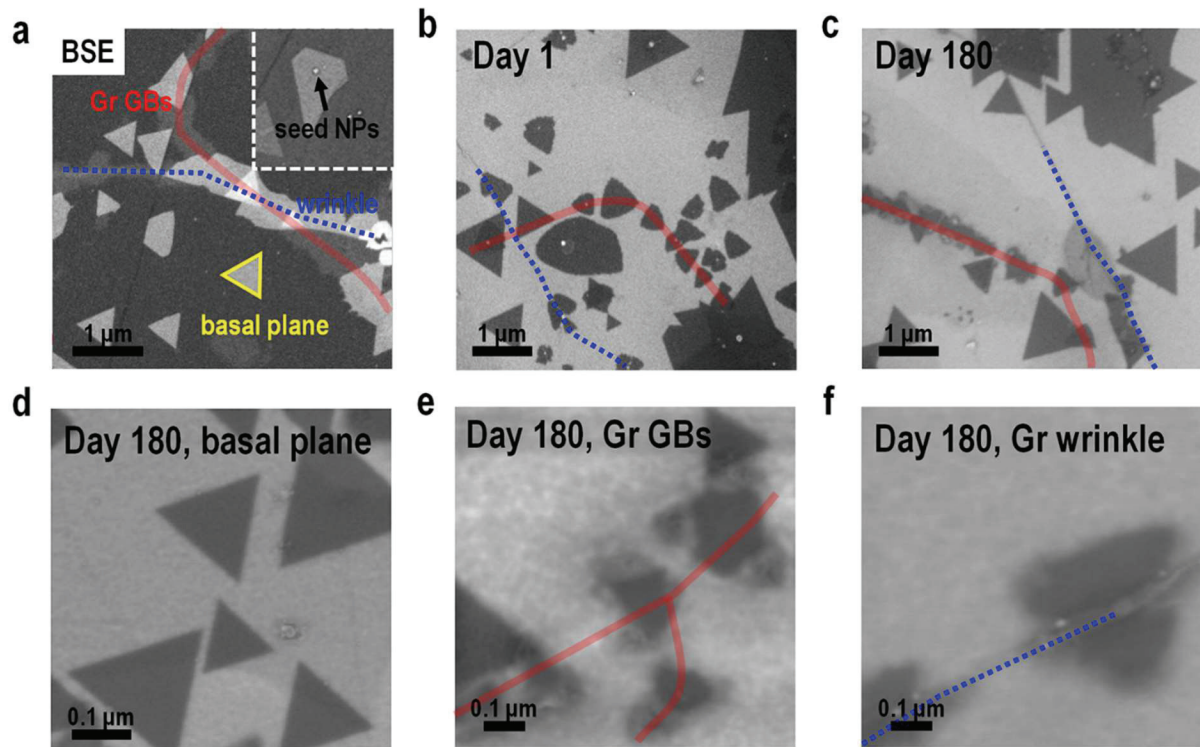
Figure 3.9 (a) BSE mode SEM images of WS_2 flakes grown on graphene using a shorter growth time (20 min) to show various growth points as studied in Figure 2.6a. SEM images of (b) as-grown and (c-f) aged WS2/Gr. The images in (d-f) are zoomed-in images of WS_2 grown at (d) basal plane, (e) GBs, and (f) wrinkled region after aging for 180 days. The red and blue lines serve as guides for the GBs and wrinkles in graphene, respectively.

3.4 Charge-Transfer-Induced Doping Effect

However, although the results above provide a reasonable explanation for the stable inner crystal of WS_2/Gr, they are insufficient in explaining the absence of degradation in the sheet edges (Figure 3.10) despite the high reactivity at these edges. Furthermore, in clear contrast to the nearly vanished WS_2 flakes of the same sample aged for 300 days (Figure 3.7e and bottom area in Figure 3.11), the delayed aging in the defect site-nucleated WS_2/Gr flakes (along the blue line in Figure 3.11) and WS_2-tf-Gr flakes (Figure 3.12) provides insight into the comparative influence of graphene as a substrate for preventing the propagation of aging.
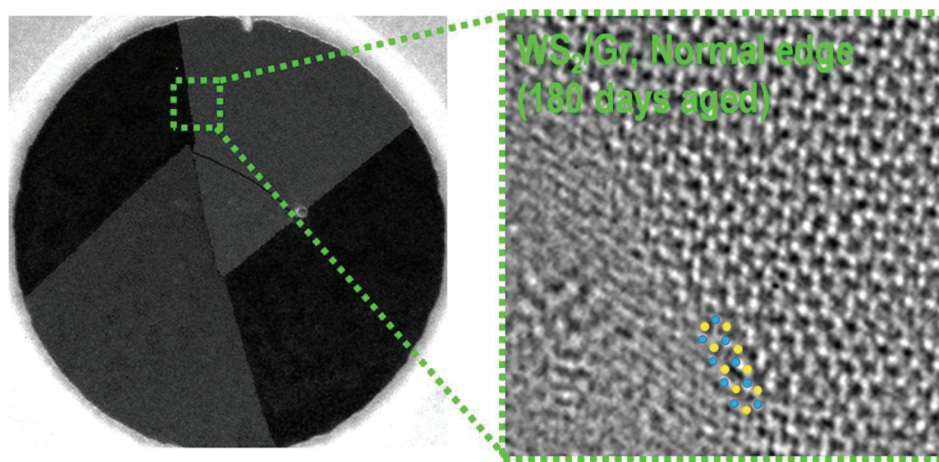
Figure 3.10 DF-TEM image (left) and Low HR-TEM images (right) of 180 days aged WS_2/Gr obtained at the normal edge (corresponding to the area in the green box in DF-TEM image).
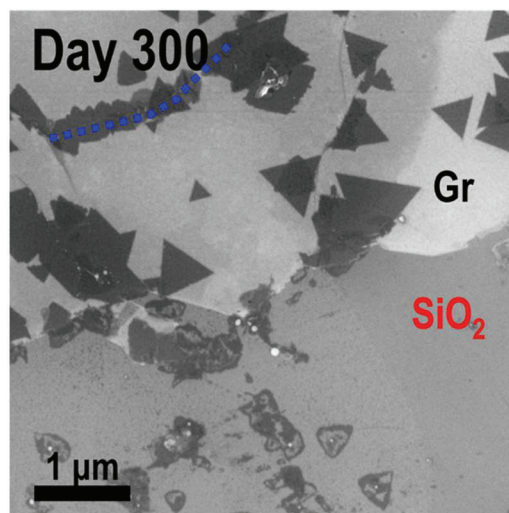
Figure 3.11 SEM images of 300 days aged WS_2/Gr and WS_2/SiO_2, obtained from the region of partially transferred graphene with uncovered SiO_2 substrate. The blue lines serve as guides for the wrinkle in graphene.
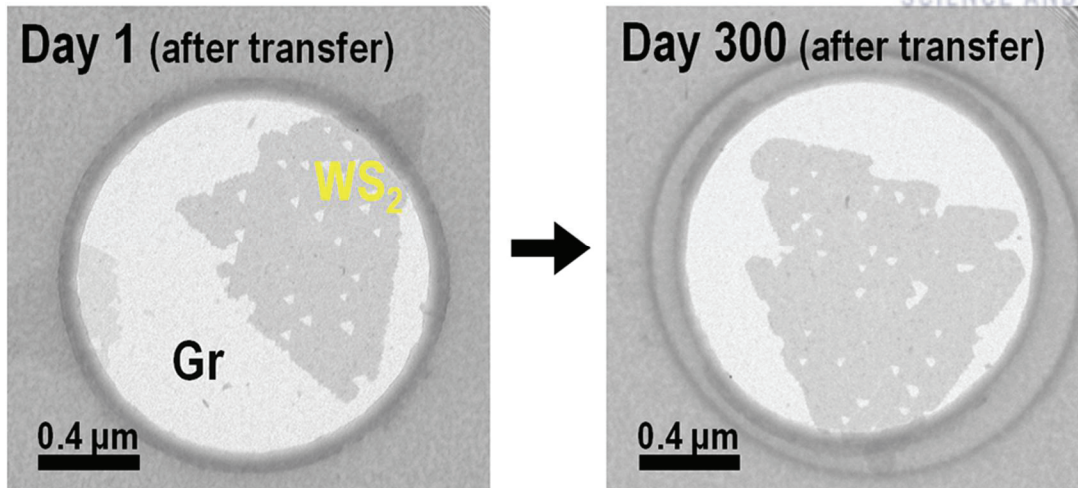
Figure 3.12 BF-TEM images of the transferred WS_2/SiO_2 (7 days aged) onto graphene supporting layer after removing SiO_2 using HF solution; measured (left) at initial transfer and (right) after another 300 days of aging.

In addition, we notice a fast charge transfer as a result of the strong interlayer interaction between WS_2 and graphene, as confirmed by the intensive quenching in the emission spectra of WS_2/Gr (Figure 3.8a), which is in agreement with the previous theoretical and experimental reports.[136] Thermodynamically, the S vacancies or W edges have high molecular affinities and bond with absorbing species in ambient air, such as H_2O and O_2, to compensate the unsaturated charges of the W 5d orbitals.[137] In the case of WS_2/Gr, we propose that the transferred extra charges may compensate the unsaturated W orbitals by strong binding between the two layers, such as a strong charge-transfer-induced doping effect.[138] As a result, WS_2/Gr may be stable without adsorption of external charged molecules. To demonstrate the chemical binding as time elapsed, we investigated the as-grown and aged WS_2 flakes using XPS. The W 4f spectra for the as-grown WS_2/Gr (Figure 3.13a) and WS_2/SiO_2 (Figure 3.13b) consisted of three main peaks (W $4f_{5/2}$, W $4f_{7/2}$, and W $5p_{3/2}$) that indicate the growth of WS_2 flakes. After aging, those peaks of the aged WS_2/SiO_2 exhibit a shift toward lower binding energies such as a p-doping effect, which indicates an increase of S vacancy sites and partial oxidation. However, it is noted that aged WS_2/Gr shows a ~0.35 eV peak shift toward higher binding energies. It is proposed that graphene progressively donates electrons to WS_2 via charge transfer, which leads to an n-doping effect over time.[138] Consequently, the PL intensity of the aged WS_2/Gr becomes weaker after the aging process, which indicates that the excess electrons could be bound to photo-excited electron-hole pairs to form trions (Figure 3.13c).[139]

We also observed the aged WS_2/Gr sample in the atomic scale using HR-TEM analysis. The dark field TEM image in Figure 3.13d) showed WS_2 flakes with torn regions. In contrast with the previous predictions and observations,[140] the torn edge of WS_2/Gr has a W-terminated Klein edge without S

passivation despite the high reactivity of bare W edges, as shown in Figure 3.13e. Moreover, defective edges of 2D materials are generally enlarged by the 80 kV e-beam irradiation after a few seconds.[141] However, dramatic reconstruction or expansion of torn edges was not observed in our WS$_2$/Gr samples under continuous e-beam exposure (Figure 3.13f). The presence of stable W edges, even without S passivation or oxidation from the absorbents, supports the idea that the surface charge transfer from graphene effectively compensates the unsaturated metal orbitals.
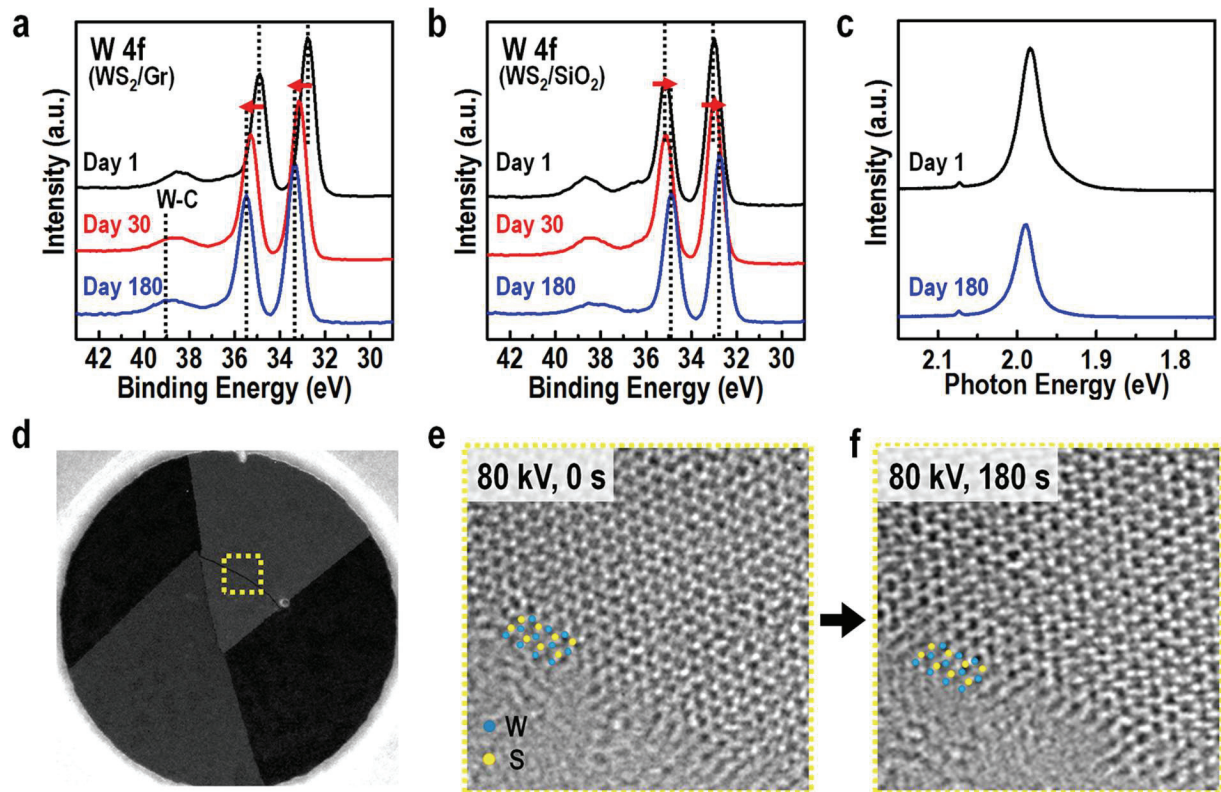
Figure 3.13 (a, b) W 4f XPS spectra of the as-grown and aged (a) WS$_2$/Gr and (b) WS$_2$/SiO$_2$, respectively. (c) The representative PL spectra of the as-grown WS$_2$/Gr and the sample aged for 180 days. (d) DF-TEM image of 180-days-aged WS$_2$/Gr. (e, f) HR-TEM images of (e) the initial and (f) electron irradiated-aged WS$_2$/Gr (for 180 days) obtained at the torn edge corresponding to the area in the yellow box in (d).

3.5 Summary and Outlook

To conclude, we have shown that chemical vapor deposited monolayer TMD materials are not air stable under ambient conditions (room temperature and atmospheric pressure) and are prone to environmental degradation over a period of several months. The gradual oxidation of these atomically thin materials in ambient conditions occurs due to the presence of oxygen and moisture. Then we have presented an epitaxial growth of remarkably air-stable TMDs monolayers obtained by simply utilizing graphene as a substrate without encapsulation; that is in contrast to the common short-term degradation of TMD flakes grown on the conventional dielectric substrates observed in recent reports. We showed that graphene causes the uniform nucleation of monolayer WS_2 flakes, which results in a genuine vdW epitaxy with negligible lateral strain and strong interlayer coupling in the uniform WS_2/graphene heterostructures. Because of the high crystallinity and charge transfer effect, the WS_2/graphene samples have a clean, uniform surface without any encapsulation even after 300 days in ambient air conditions. Moreover, we propose the possible mechanism for the lack of aging-related deterioration in our encapsulation-free WS_2/graphene samples. Our results can pave the way for the realization of high-performance and air-stable vdW heterostructure-based electronic and optoelectronic devices.

Future work should investigate the air-stability of TMDs with chalcogens other than S, as well as careful optimization of the capping or encapsulation layer for prolonged stability under ambient conditions. Another factor that needs to be studied in detail is the role of the substrate. Substrates that give better epitaxy for TMDs could render them more robust against ambient attack. Also, the wettability or surface charge of the substrate could also play an important role. For example, subtrates that are significantly more hydrophobic than SiO_2/Si could be far more resistant to environmental attack under wet and humid conditions. Most importantly, in-depth modeling and simulation work of corrosion in monolayer TMD materials to understand the mechanisms by which sulfur is lost and replaced by oxygen is necessary.

CHAPTER 4

Different Properties of vdW Heterostructures Depending on Defects in Template Layer

This chapter was mostly copied from reference [142].

4.1 Introduction

As the family of two-dimensional (2D) materials expands, vertical or in-plane van der Waals (vdW) heterostructures are of great interests[3, 143] due to the novel fundamental properties and wide range of capabilities of these 2D materials. A unique characteristic of these 2D materials is the facile formation of vdW heterostructures by stacking layers of different materials and thicknesses. The properties and performances of the vdW heterostructures are significantly affected by their stacking geometries and interlayer coupling (including interlayer charge transfer and energy transfer), and their application in devices like transistors[143] and diodes[144] have triggered a great deal of enthusiasm. However, the large-scale formation of high-quality vdW heterostructures with atomically clean and sharp hetero-interfaces, essential for preserving optoelectronic properties generated by interlayer coupling, remains a critical technological issue.

Chemical vapor deposition (CVD) has so far been utilized for the synthesis of layered 2D materials and their heterostructures,[8, 87, 145] which are regular and scalable in principle. In essence, typical films of large-scale 2D materials produced by CVD are polycrystalline in nature and contain a high density of atomic and structural defects like vacancies, adatoms, wrinkles, and line defects, which are associated with a broken lattice symmetry, a modified energy landscape, and quantum confinement.[38, 146] Particularly, these localized heterogeneities strongly affect the electronic properties of 2D materials (*e.g.,* electron scattering, transport, excitation, *etc*.).[147] In addition, defects in the template layer can have a profound effect on the nucleation and growth of heterostructures, because dangling bonds at vacancy defects, curved wrinkles, and grain boundaries (GBs) are more reactive and have interaction strengths different from that of a pristine region.[100] However, the effects of atomic and structural defects on the interlayer properties or configuration have not previously been considered. Instead, previous theoretical and experimental studies have considered only the defect-free templates.[87, 148]

Herein, the effects of atomic and structural defects on the interlayer properties in vertically-stacked van der Waals Heterostructures were rationalized using two types of WS_2 grown on polycrystalline graphene; WS_2 flakes on the graphene defects (D-WS_2) and pristine basal plane (B-WS_2). Interestingly, although B- and D-WS_2 flakes exhibit different layer deformability, thermal stability and physical and electrical properties, both types of WS_2 flakes have the same crystal structure despite the atomic displacement and lattice distortion beneath the D-WS_2 flakes. This discrepancy in material properties suggests that the defects of the underlying template (graphene) have a strong influence on the interlayer interactions between the stacking layers of WS_2 and graphene, an observation is supported by a

combination of theoretical and experimental results. Furthermore, D-WS$_2$ flakes have more effective charge transport at the interface than that of B-WS$_2$ flakes because of covalent bonding and larger orbital overlap compared to van der Waals (vdW) contacts. This result can readily be applicable to other 2D vdW heterostructures and unravels the importance of understanding interlayer coupling and its effect on obtaining desirable properties.

4.2 Experimental Methods

Preparation of WS$_2$/Gr heterostructures

B- and D-WS$_2$ flakes were simultaneously synthesized by direct growth on CVD graphene, which had been transferred on SiO$_2$/Si substrate. A detailed description of the preparation method is presented in Chapter 2.2.

Characterizations

We performed SEM measurements in SE and BSE modes using a cold field emission SEM (FE-SEM) (Hitachi SU-8220) with an accelerating voltage of 1 kV. The Raman spectroscopy and mapping were obtained using a WiTec Alpha 300R M-Raman system equipped with a computer-controlled *x-y* translation stage and a 532 nm excitation source. During the measurements, the laser power was kept below 0.5 mW at the sample to avoid laser-induced thermal effects or damage.

All AFM experiments were performed using a commercial AFM instrument (Multimode 8, Bruker) equipped with a scanner (100 × 100 μm^2) under ambient conditions. The topology and phase imaging were recorded using the tapping mode and antimony-doped silicon tips with the normal resonance frequency of ~300 kHz and a spring constant of ~40 N/m. Electrically conductive platinum-iridium coated tips with the normal resonance frequency of ~13 kHz and a spring constant of ~0.2 N/m were used in contact mode to measure the current map and I-V curve. Both electrical characterizations were operated at 0.5 V DC bias.

WS$_2$/Gr heterostructures were analyzed using an aberration-corrected FEI Titan cube G2 60-300 with a monochromator. It was operated at 80 kV and typical electron beam densities were approximately 5 × 10^5 e$^-$/nm^2 in order to reduce beam damage to the specimen. Selected area electron diffraction (SAED) and dark-field TEM (DF-TEM) mode were applied for analysis of the GB in graphene. In addition, a sub-angstrom resolution STEM image with probe-aberration correction was analyzed for the atomic structure of B-WS$_2$ and D-WS$_2$ flakes with Z contrast. Low-loss EELS analyses were carried out for comparing electronic structures. The energy resolution was ~1.0 eV and energy dispersion was 0.1 eV.

DFT calculations

Spin-polarized DFT calculations were carried out using Vienna ab-initio simulation package (VASP) code.[149] The calculations were performed within the generalized gradient approximation (GGA) of the Perdew–Burke–Ernzerhof (PBE) functional[150] and vdW interaction was considered using DFT-D3 scheme.[151] Basis set contains plane waves up to an energy cutoff of 400 eV for ionic relaxation and 600 eV for cell relaxation and all the structural relaxations were performed until the total energy differences between each relaxation steps are smaller than 10^{-6} eV. We modeled two types of supercell to investigate interactions between WS$_2$ monolayer and graphene. The first model is a hexagonal supercell which was made of 4 × 4 graphene and 3 × 3 WS$_2$. The second model is an orthorhombic supercell which was

made of one of the most stable large-angle GB structure of graphene[152] (misorientation angle ~32.2°) and 6×3 orthorhombic WS_2 structure. Vacuum region of ~23 Å was also contained in the perpendicular direction of graphene and WS_2. We chose the appropriate size of supercell to reduce both lattice mismatch and computational cost. Lattice mismatches are 3.3% for a hexagonal supercell and 6.4%, 7.0% (x and y directions, correspondingly) for an orthorhombic supercell but it does not have significant effect on the results. Monkhorst-Pack scheme[153] was used to sample the Brillouin zone with $4 \times 4 \times 1$ grid for a hexagonal supercell and $2 \times 4 \times 1$ grid for an orthorhombic supercell.

4.3 Classification of TMDs/Gr Heterostructure According to Morphological Differences of Graphene

A representative scanning electron microscopy (SEM) image of WS_2 flakes simultaneously grown on graphene is depicted in Figure 4.1a, revealing two types of WS_2 flakes: relatively small irregular flakes (D-WS_2 flakes, marked with a red circle) that appear along line features and large triangular flakes with sharp and parallel edges (B-WS_2 flakes, marked with a blue circle).
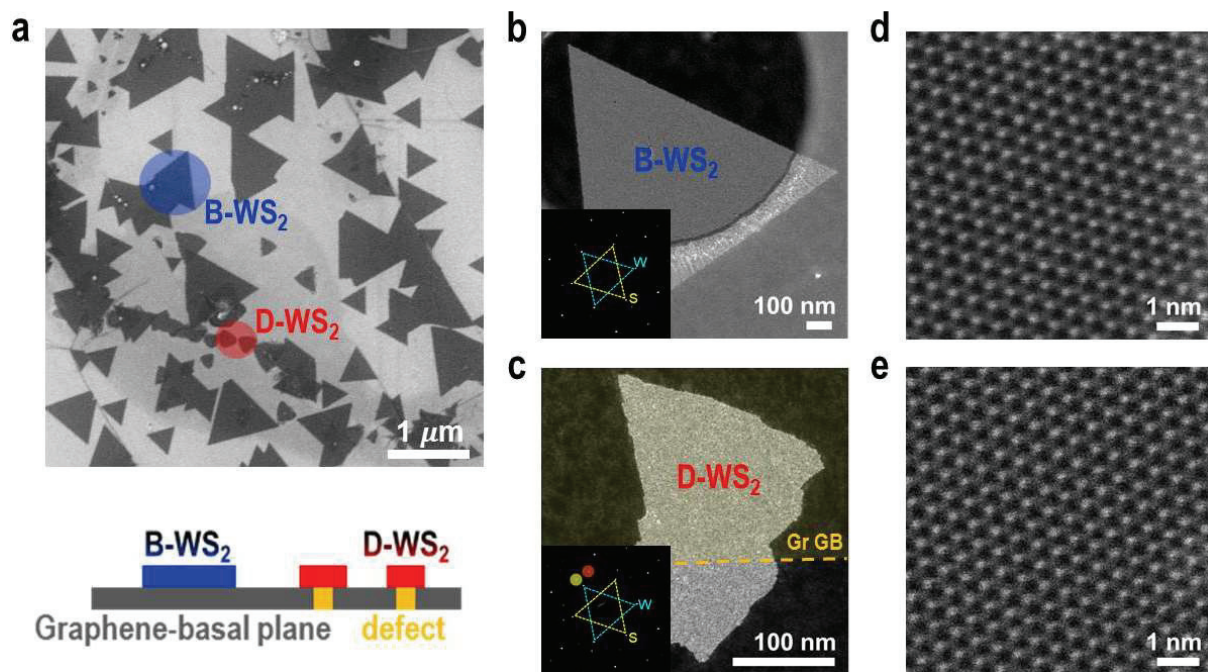
Figure 4.1 (a) SEM images of WS_2 flakes directly grown on a graphene template. Inset: the corresponding schematic illustration for B- and D-WS_2 flakes, marked (a) using blue and red circles, respectively. (b, c) Low-magnitude TEM images with SAED patterns and (d, e) atomic-resolution STEM images of (b, d) B- and (c, e) D-WS_2 flakes.

The structural defects of graphene (*e.g.,* vacancies, wrinkles and GBs) are common nucleation sites for growth and adsorption because of the high reactivities of the strained sp^2 bond and exposed dangling bonds.[102] Therefore, nucleation of D-WS_2 flakes is achieved earlier than that of B-WS_2 flakes, as observed early in the growth process (Figure 4.2). Instead, the large binding energy of these defect sites is intimately related to a high diffusion barrier that further hinders the growth and enlargement of D-WS_2 flakes. Transmission electron microscopy (TEM) was used to characterize the crystal structure and quality of both types of WS_2 flakes on graphene. Figures 4.1b and c show low-magnification TEM images and the corresponding selective area electron diffraction (SAED) patterns of B- and D-WS_2

flakes, respectively. The inset image in Figure 4.1b depicts two well-arranged sets of hexagonal diffraction spots: the inner set from WS$_2$ flakes (a = 0.272 nm) and the outer set from graphene (a = 0.213 nm). This figure confirms that the crystal quality is good and both B-WS$_2$ and graphene are single-crystals with the same orientation as expected from epitaxial growth. The SAED pattern from the yellow dotted line in Figure 4.1c is in good agreement with Figure 4.1b, although the two sets of diffraction spots indicate a GB between two graphene grains. Figures 4.1d and e show the representative atomic-resolution scanning TEM (STEM) images from the same flakes as shown in Figures 4.1b and c, respectively. No noticeable defects or structural modulation is observed in either of these images, suggesting that both B-WS$_2$ and D-WS$_2$ flakes possess high crystallinity.
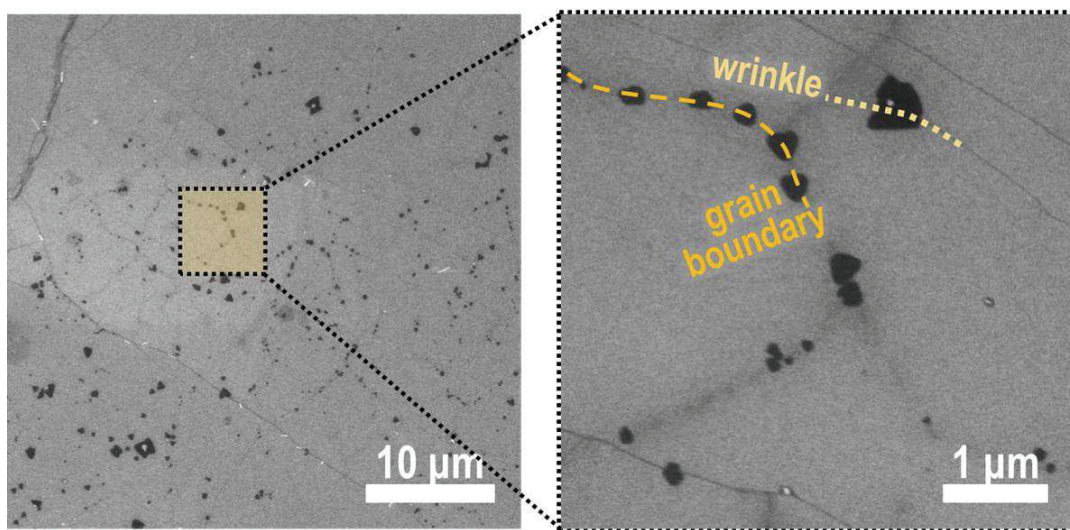
Figure 4.2 (a) Representative SEM images of WS$_2$ grown on graphene obtained at the early stage of growth with a reduced growth time (10 min). (b) A high-magnification SEM image of (a).

4.4 Impact of Defects on Properties of TMDs/Graphene Heterostructures

4.4.1 Comparative Study of Physical Properties in Heterostructures

An AFM topography image is also presented in Figure 4.3a to study the morphologies of the as-grown WS_2 flakes. The uniform color contrast indicates that the thickness of the grown WS_2 flakes is homogeneous. The corresponding height profiles in two types of WS_2 flakes display an average height of ~0.7 nm relative to that of graphene (Figure 4.3b), verifying the formation of monolayer WS_2;[154] however, an obvious contrast difference is observed in the phase image (Figure 4.3c) that was simultaneously acquired with Figure 4.3a using tapping mode AFM. Compared to both B-WS_2 flakes and an exposed graphene surface, D-WS_2 flakes show much brighter contrast. A phase image is obtained by recording the phase shift between the excitation force and the tip response. Presently, this AFM technique is a versatile tool for mapping variations in the composition, friction, viscoelasticity, and adhesion of surfaces with nanoscale spatial resolution. The phase shift angle ($\Delta\varphi$) is related to the local energy dissipation (E_{dis}) on the surface,[155] according to the following Equation (4.1):

$$E_{dis} = \left[\sin\left(\frac{\pi}{2} - \Delta\varphi\right) - \frac{A_{sp}}{A_0} \right] \times \frac{\pi k_{sp} A_0}{Q} \qquad (4.1)$$

where A_{sp} is the amplitude set-point of the AFM cantilever oscillations, A_0 is the free-oscillation amplitude, and k and Q are the force constants of the AFM cantilever and quality factor, respectively. Based on Figure 4.3c, the measured $\Delta\varphi$ of B-WS_2, D-WS_2, and graphene are 4º, 0º, and -1º, respectively. This measurement was performed simultaneously with the same AFM cantilever and imaging condition, so Equation (4.1) is determined only by the value of $\Delta\varphi$. As a result, the brighter phase contrast of D-WS_2 flakes indicates a smaller value of E_{dis}, suggesting that D-WS_2 flakes are less deformable than B-WS_2 flakes and the exposed graphene area. However, according to the previous studies that used multilayered vdW materials, the top layer is prone to deformation and has a larger contact area that dissipates more energy.[156] This discrepancy suggests that D-WS_2 flakes have an unusually tight interaction with the underlying graphene without significant disorders and defects as observed in Figure 4.1e, unlike B-WS_2 flakes and other typical vdW stacked materials.

Previous studies reported layer-by-layer thermal etching of TMDs from top to bottom when exposed to air at temperatures over 300 ºC due to the strong covalent bonding within the TMD layer and the weak interaction between the stacked layers.[157] Figures 4.4a and b show backscattered electron (BSE) mode SEM images of WS_2 flakes on graphene before and after annealing at 500 ºC in ambient air. Figure 4.4b shows that B-WS_2 flakes are removed completely after a thermal treatment for 1 h, as expected. However, under the same conditions, D-WS_2 flakes are thermally stable on graphene with just a little broadening of the Raman peaks (Figure 4.4c). This result also suggests that the interlayer interaction exists between D-WS_2 and graphene, different than that of B-WS_2 and graphene.
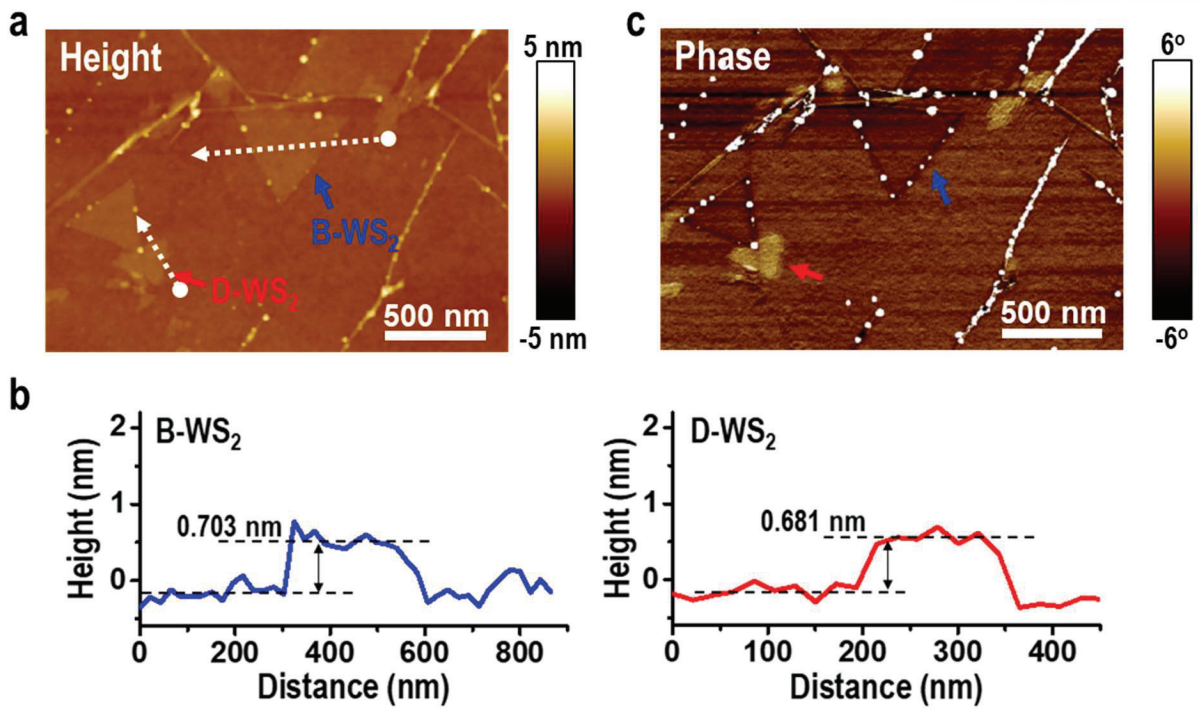
Figure 4.3 (a) The topography (height) image and line profiles across isolated B-WS$_2$ flakes (blue line) and D-WS$_2$ flakes (red line). (c) The phase image of WS$_2$ flakes grown on graphene measured using the tapping mode AFM.
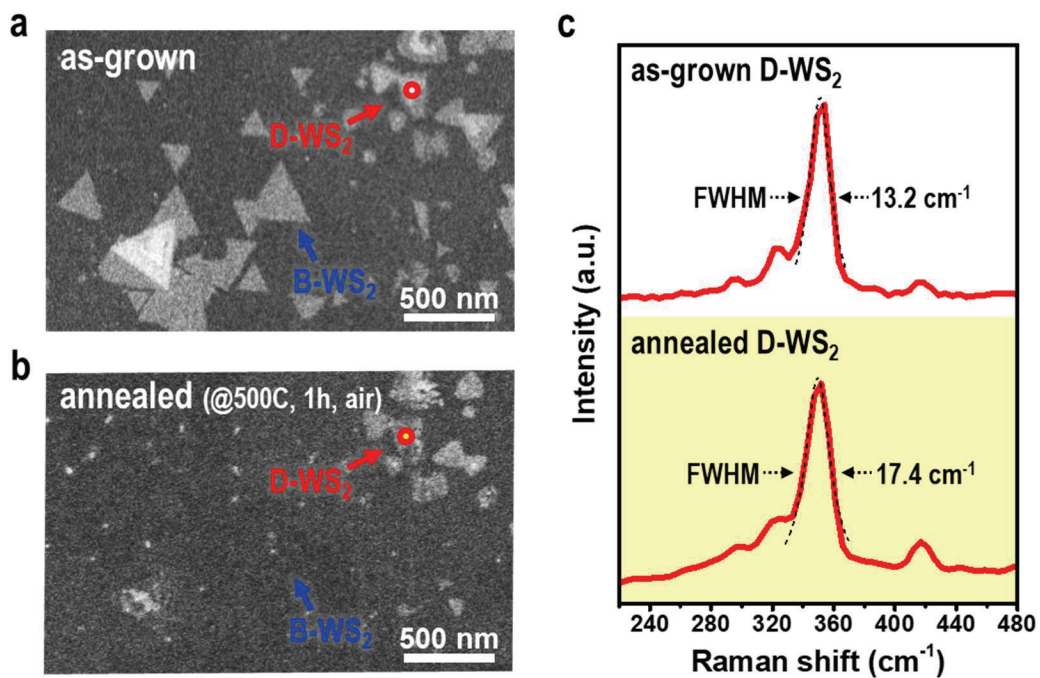
Figure 4.4 (a,b) SEM images of B- and D-WS$_2$ flakes (a) before and (b) after annealing at 500 °C in air for 1 h. (c) Raman spectra measured on D-WS$_2$ flakes before and after annealing.

57

Additional evidence comes from the beam damage test. Figure 4.5 shows the knock-on damaged HR-TEM images of $B-WS_2$ and $D-WS_2$ flakes. Knock-on damage refers to the process involving direct elastic collisions between imaging electrons and target atoms induced by high electron energy. This damage is substantial in 2D materials because the accelerating voltage in TEM is comparable to the threshold energy of knock-on damage, such as 86 kV for carbon[158] and 80 kV for sulfur.[159] Knock-on damage from TEM is particularly dominant in the bottom layer due to transmitted electrons. Because transferring the sample to the TEM grid creates a flipped-over structure, knock-on damage is prevalent in the WS_2 layer. Therefore, as shown in Figure 4.5a, the graphene lattice is observed in the damaged WS_2 region with the missing atoms from the $B-WS_2$ layer. On the other hand, $D-WS_2$ flakes in Figure 4.5b exhibit damage from e-beam irradiation, meaning that both WS_2 flakes and graphene are damaged simultaneously. Previous work reported that the rate of knock-on damage reflects the extent of interatomic bonding.[160] Ionic or covalent bonding with sp^3 hybrid orbitals is weaker than interatomic bonding with sp^2 hybrid orbitals. Thus, we can predict how the difference in the interatomic bonding between the two types of WS_2 flakes and graphene results in substantially different knock-on damage.
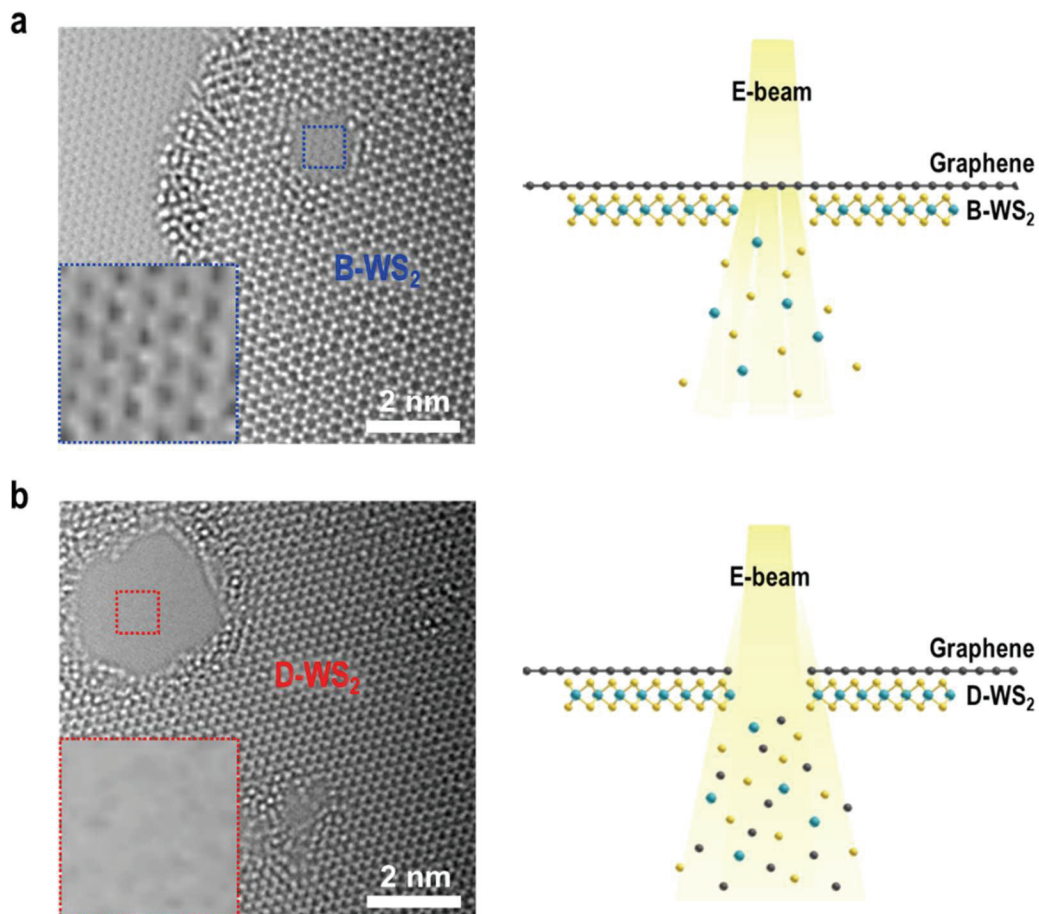
Figure 4.5 (a,b) Atomic resolution TEM images of knock-on damaged area in (a) B- and (b) $D-WS_2$ flakes, respectively, with simple schematic illustrations.

58

4.4.2 Understanding Interfacial Geometries

To unravel the different interfacial properties of D-WS$_2$ flakes, the binding energies between WS$_2$ and graphene GBs (Gr-GBs) were investigated using spin-polarized DFT calculations including vdW correction (Grimme's D3 method).[151] The binding energy is defined as following Equation (4.2):

$$E_b = E_{WS_2} + E_{graphene} - E_{total}, \qquad (4.2)$$

where E_{WS_2}, $E_{graphene}$, and E_{total} denote the total energy of isolated WS$_2$, graphene, and WS$_2$/graphene system, respectively. We first consider the B-WS$_2$ case using a periodic 3 $\times$ 3 supercell of WS$_2$ and defect-free 4 × 4 of graphene (Figure 4.6a). The binding energy (E_b) per functional unit (0.18 eV) indicates that interaction between WS$_2$ and defect-free graphene is vdW force, as described in previous reports. For D-WS$_2$, we take the orthorhombic supercell (Detailed information seen in experimental section) which was made of one of the most stable large-angle GB structure of graphene[152] (misorientation angle ~32.2°) and 6 × 3 orthorhombic WS$_2$ structure. Besides the pristine Gr-GB, defective Gr-GBs with vacancies or substitutional atoms are also common in graphene due to the high reactivity and adsorption energy of Gr-GBs.[161] Therefore, calculations were performed to investigate the optimized geometries of pristine Gr-GBs and GBs with defects, *e.g.,* vacancies and source atoms (W and S) substituted vacancies.
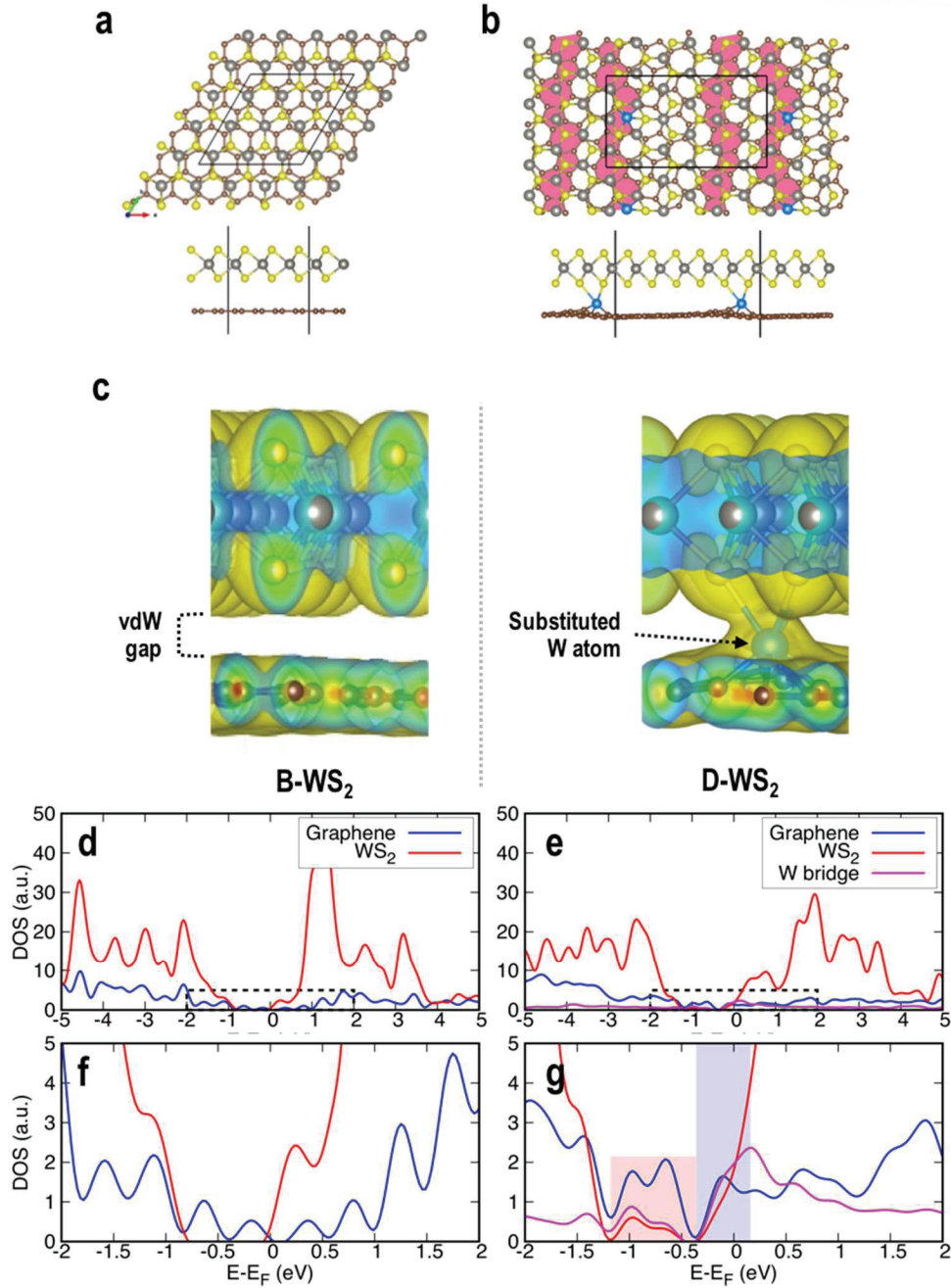
Figure 4.6 (a,b) The optimized structure of (a) WS_2 on pristine graphene (B-WS_2 case) and (b) WS_2 on W-substituted Gr-GB (D-WS_2 case) after full relaxation. Solid lines denote boundary of each supercell. GBs of graphene are indicated with pink colored regions. (c) The isosurface maps of charge density for the optimized structure in (a) and (b), respectively. The isosurface level is 4.9×10^{-6} e/a_0 (a_0 is a Bohr radius). (d-g) Density of states (DOS) of (d,f) WS_2 on pristine graphene and (e,g) WS_2 on W-substituted Gr-GB near the Fermi level. Dotted rectangular regions in (d) and (e) are shown in the magnified view of (f) and (g). Blue and red shaded areas in (g) indicate electron sharing between WS_2 flakes and graphene with W atomic bridge.

60

	Perfect Gr basal plane	Pristine Gr-GB	Gr-GB with vacancy	S-substituted Gr-GB	W-substituted Gr-GB
Binding E per f.u. (eV)	**0.18**	0.17	0.17	0.15	**0.23**
Bond between graphene and WS_2	**vdW**	vdW	vdW	vdW	**Covalent**

Table 4.1 Computed binding energies and bonding predictions of WS_2 on pristine and defect-containing graphene cases.

The obtained binding energies of Gr-GBs for WS_2 are presented in **Table 4.1**. Among the possible Gr-GB cases, the most stable structure for a WS_2 layer is found to be a W-substituted Gr-GB case. The fairly high binding energy difference (almost 1 eV in total energy) drives the formation of a graphene-W-WS_2 network.[162] Accordingly, Figure 4.6b shows the optimized structure of fully relaxed WS_2 on the W-substituted Gr-GB that includes a covalent bond between the substituted W atom and the edge S atom of the WS_2 monolayer. We observe that the optimized structure of the WS_2 layer is nearly unaffected by their local environments and similar to the structure of isolated WS_2, as shown in the TEM images in Figures 4.1b-e. To further confirm bonding between WS_2 and graphene, we performed charge density analysis (Figure 4.6c). Compared with WS_2 on pristine graphene (the B-WS_2 case), the predicted D-WS_2 case shows that charge redistribution mostly occurs in the contact region between WS_2 and W-substituted Gr-GB, originating from the hybrid orbitals.

In addition to the calculations, we also performed an EELS study to have a better understanding of the bonding nature between two heterostructures. An EELS in STEM provides information on π plasmon and $\pi+\sigma$ plasmon with considerable in-plane components from several milliradians of collection angles.[163] As observed in Figures 4.1b-e, there are no differences between the lattice parameters or structures of B- and D-WS_2 flakes. However, Figure 4.7 shows significantly different low-loss electron excitations of graphene in B-WS_2 and D-WS_2 flakes. The π plasmon peak at around ~5 eV is presented in B-WS_2 flakes like a pristine graphene monolayer,[164] whereas the reduced π plasmon peak in D-WS_2 flakes indicates the degradation of this characteristic of intrinsic graphene. In addition, there is a significant blue shift in the $\pi+\sigma$ plasmon region of B-WS_2 flakes, compared to that of D-WS_2 flakes (and the reported $\pi+\sigma$ plasmon region (~15-16 eV) of pristine graphene monolayer[163-165]). In previous research, the bulk plasmon region (a combination of π^* and σ^* electronic excitations) of a semiconductor was suggested to reflect weakly bound valence electrons.[166] Therefore, a shift in the $\pi+\sigma$ plasmon peak is related to the density of valence electrons. In the case of B-WS_2 flakes, the valence electrons in WS_2 and graphene are superimposed upon each other via vdW bonding (with no practical bonds between valence electrons), resulting in increased valence electron density and a significant blue

shift in the bulk plasmon peak.[167] On the contrary, in the case of D-WS$_2$ flakes, we can estimate that valence electrons are shared between WS$_2$ flakes and graphene defects with substituted W atoms that have numerous unfilled valence electrons.[168] We then validate the estimation using density of state (DOS) analysis (Figure 4.6d-g), and demonstrate that valence electrons of WS$_2$, graphene, and W atomic bridge near the Fermi level are shared each other (red shaded area in Figure 4.6g). In other words, the valence electrons of D-WS$_2$ flakes and defective graphene are strongly coupled.
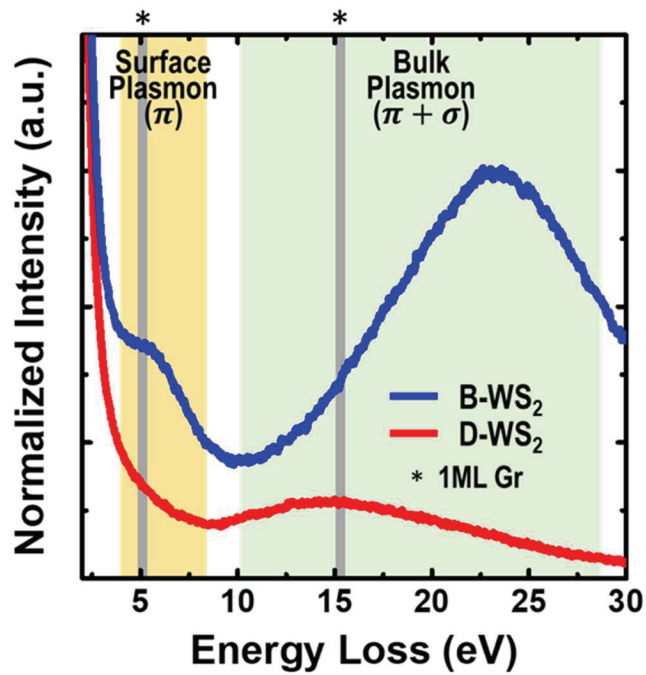
Figure 4.7 Low-loss EELS spectra in B-WS$_2$ flakes (blue curve) and D-WS$_2$ flakes (red curve) on graphene.

4.5 Electrical Characterizations for Electronic and Junction Properties

The formation of interfacial bonding should have a direct effect on the electronic and junction properties of heterostructures.[169] C-AFM measurements, using graphene as a back electrode, were performed to evaluate out-of-plane charge transport at the interfaces between B- and D-WS$_2$ flakes and graphene. A Pt-Ir-coated conductive tip measured the current generated by the applied bias voltage as a function of *x-y* position, while maintaining mechanical contact with the surface. The topography of the as-grown monolayer of WS$_2$ flakes on graphene (Figure 4.8a) shows no contrast between flakes of B- and D-WS$_2$, as described above. The simultaneously recorded current map is given in Figure 4.8b. As predicted based on the individual electrical properties of WS$_2$ flakes and graphene, lower currents are recorded on B-WS$_2$ flakes, which makes the flake distinct from the surrounding graphene. It has been reported previously that Schottky contacts are formed between WS$_2$ and graphene with small Schottky barrier. Consistent results are obtained from the I–V curves on B-WS$_2$ flakes (blue-colored curve) in Figure 4.8c, showing the non-linear characteristics typical of a metal-semiconductor junction. However, compared with B-WS$_2$, the current map on D-WS$_2$ flakes shows enhancement of electrical conductance with uniform current contrast through the entire flake due to the current spreading in WS$_2$ layer.
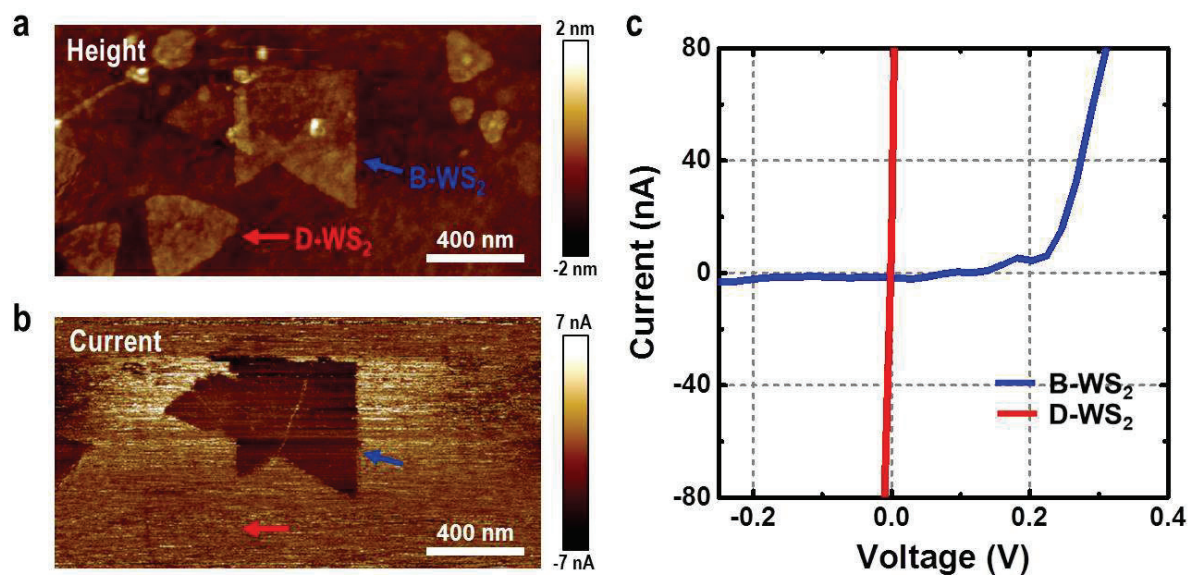
Figure 4.8 (a) The topography (height) image and (b) corresponding current image (recorded at +0.2V) of WS$_2$ flakes grown on graphene. (c) I-V curves recorded with Pt-Ir coated tip on B-WS$_2$ flakes (blue curve) and D-WS$_2$ flakes (red curve) on graphene.

It is worthwhile to note that a strong current spreading in TMDs was experimentally observed in the MoS$_2$ monolayer of approximately 1 μm in diameter,[170] which is greater than the triangle sizes of our monolayer WS$_2$ flakes. Moreover, I-V curves of D-WS$_2$ (red-colored curve) show a strong linear dependence, implying low resistance Ohmic contacts between D-WS$_2$ and graphene. These electrical characterization results suggest the formation of electrical connections between D-WS$_2$ and graphene.[171] In the DOS analysis, we also found that D-WS$_2$ and graphene share electronic states near the Fermi level that can contribute electrical conductivity of D-WS$_2$ (blue shaded area in Figure 4.6g). In other words, the formation of larger overlapping hybrid orbitals improves the intrinsic conductivity of D-WS$_2$, as opposed to general vdW bonded heterostructures.[172]

4.6 Summary and Outlook

The availability of various isolated two-dimensional (2D) materials allows the facile formation of van der Waals (vdW) heterostructures by stacking layers of different materials and thicknesses. The physical properties of the vdW heterostructures are significantly affected by their stacking geometries and interlayer coupling (including interlayer charge transfer and energy transfer). In a previous study, we showed that monolayer WS_2 flakes grown onto a graphene substrate exhibit outstanding air stability compared to the flakes grown on a SiO_2/Si substrate.[130] Using various characterization tools and based on previous reports, we demonstrated that the surface charge transfer significantly affects the prevention of air degradation for the first time. This result suggested that understanding the effect of interlayer coupling in the stacking geometry of vdW heterostructures is highly important for obtaining materials with desirable properties.

In this work, we discover that the intrinsic properties of subsequent layers of a heterostructure are dependent on the structural features of the template layer (*e.g.,* the basal plane and GB of graphene). We have compared the intrinsic characteristics of vertical 2D heterostructures using two types of WS_2 flakes grown directly on graphene defects (D-WS_2) and a pristine basal plane (B-WS_2). In contrast to B-WS_2 flakes, D-WS_2 flakes are highly conductive and exhibit lower contact resistance with effective charge transport at the interface, even though both types of WS_2 flakes have the same crystal structure without atomic distortions or defect formation. Using experimental and computational studies, this difference in behavior of D-WS_2 flakes is attributed to the formation of covalent bonds via W atomic bridges at defect sites. Our results reveal the importance of understanding the interlayer bonding and structural differences can affect the fundamental properties of 2D heterostructures and provide materials useful for a wide spectrum of engineering applications. This new defect-mediated heterostructure and its new properties extend the various possibilities for a wide spectrum of engineering applications, and also emphasize the importance of understanding the interlayer coupling in the stacking and interlayer geometries and its correlation effect for designing desirable properties.

CHAPTER 5

Conclusion and Discussion

As mentioned in the previous chapter, although vertical heterostructures can be easily fabricated through a multiple-step aligned transfer method, this method is time-consuming and residual polymer and unavoidable contaminants have negative effects on the properties of as-made heterostructures. Controlled scalable synthesis of multi-junction van der Waals (vdW) heterostructures with clean interface is still the bottleneck of practical applications. Therefore, an all-CVD method must be developed for growing high quality vertical heterostructures.

In this dissertation, I have deat with the with the synthesis and characterization of semiconducting 2D TMDs and their heterostructures, especially with graphene, for emerging applications. At first, the direct growth method for obtaining high-quality uniform WS_2/graphene heterostructure with strong interlayer coupling was proposed. We achieved the uniform nucleation of monolayer WS2 flakes on an inert basal plane of graphene by introducing source contact geometry. This uniform nucleation results in a genuine vdW epitaxy with negligible lateral strain and promotes charge transfer between the two layers. Thus, our epitaxially grown WS_2/graphene samples show superior strain homogeneity and high crystal quality with extremely low levels of charged impurities and defects.

Furthermore, for stable device fabrication and operation, understanding of their air-stability is highly important. In this work, the investigation on environmental stability and oxidation mechanism of 2H-TMDs were observed in time sequence. Meanwhile, our epitaxially grown WS_2/Gr samples have a clean, uniform surface without any encapsulation, even after 1 years in ambient air conditions. We also show that graphene substrates prohibit the aging phenomena in both of the basal planes and edges of 2D TMDs flakes, compared to the commonly observed short-term degradation of TMD flakes. Based on these result, we demonstrate that high crystallinity is a key factor that determines the high air stability, and firstly reveal the charge transfer-induced doping as an additional factor for the enhanced air stability.

Since dangling bonds at vacancy defects, curved wrinkles, and grain boundaries (GBs) are more reactive and have interaction strengths different from that of a pristine region, the structural characteristics of graphene, as well as just graphene itself, can affect to the properties of TMDs. Using our WS_2/Gr samples, we also studied the effects of atomic and structural defects on the interlayer properties or configuration in the van der Waals heterostructures have been thoroughly investigated and presented that the differences are attributed to the formation of covalent bonds at defect sites on graphene surface.

These results reveal the importance of understanding the interlayer coupling in stacking geometries and its correlation effect for designing desirable properties in 2D vdW heterostructures for

future device applications. The practical application of heterostructures is still at an early stage. In this sense, it is expected that our results can pave the way for the realization of high-performance and air-stable vdW heterostructure-based electronic and optoelectronic devices in the near future.

REFERENCES

1. Novoselov, K. S.; Geim, A. K.; Morozov, S. V.; Jiang, D.; Zhang, Y.; Dubonos, S. V.; Grigorieva, I. V.; Firsov, A. A., Electric field effect in atomically thin carbon films. *Science* **2004,** *306* (5696), 666-669.

2. Bae, S.; Kim, H.; Lee, Y.; Xu, X.; Park, J.-S.; Zheng, Y.; Balakrishnan, J.; Lei, T.; Kim, H. R.; Song, Y. I., Roll-to-roll production of 30-inch graphene films for transparent electrodes. *Nat. Nanotechnol.* **2010,** *5* (8), 574.

3. Geim, A. K.; Grigorieva, I. V., Van der Waals heterostructures. *Nature* **2013,** *499* (7459), 419.

4. Radisavljevic, B.; Radenovic, A.; Brivio, J.; Giacometti, i. V.; Kis, A., Single-layer MoS_2 transistors. *Nat. Nanotechnol.* **2011,** *6* (3), 147.

5. Li, X.; Cai, W.; An, J.; Kim, S.; Nah, J.; Yang, D.; Piner, R.; Velamakanni, A.; Jung, I.; Tutuc, E., Large-area synthesis of high-quality and uniform graphene films on copper foils. *Science* **2009,** *324* (5932), 1312-1314.

6. Lee, Y. H.; Zhang, X. Q.; Zhang, W.; Chang, M. T.; Lin, C. T.; Chang, K. D.; Yu, Y. C.; Wang, J. T. W.; Chang, C. S.; Li, L. J., Synthesis of large-area MoS_2 atomic layers with chemical vapor deposition. *Adv. Mater.* **2012,** *24* (17), 2320-2325.

7. Li, S.; Wang, S.; Tang, D.-M.; Zhao, W.; Xu, H.; Chu, L.; Bando, Y.; Golberg, D.; Eda, G., Halide-assisted atmospheric pressure growth of large WSe_2 and WS_2 monolayer crystals. *Appl. Mater. Today* **2015,** *1* (1), 60-66.

8. Gong, Y.; Lin, J.; Wang, X.; Shi, G.; Lei, S.; Lin, Z.; Zou, X.; Ye, G.; Vajtai, R.; Yakobson, B. I., Vertical and in-plane heterostructures from WS_2/MoS_2 monolayers. *Nat. Mater.* **2014,** *13* (12), 1135.

9. Kang, K.; Xie, S.; Huang, L.; Han, Y.; Huang, P. Y.; Mak, K. F.; Kim, C.-J.; Muller, D.; Park, J., High-mobility three-atom-thick semiconducting films with wafer-scale homogeneity. *Nature* **2015,** *520* (7549), 656.

10. Zhou, L.; Zubair, A.; Wang, Z.; Zhang, X.; Ouyang, F.; Xu, K.; Fang, W.; Ueno, K.; Li, J.; Palacios, T., Synthesis of High-Quality Large-Area Homogenous 1T′ $MoTe_2$ from Chemical Vapor Deposition. *Adv. Mater.* **2016,** *28* (43), 9526-9531.

11. Liu, K.-K.; Zhang, W.; Lee, Y.-H.; Lin, Y.-C.; Chang, M.-T.; Su, C.-Y.; Chang, C.-S.; Li, H.; Shi, Y.; Zhang, H., Growth of large-area and highly crystalline MoS_2 thin layers on insulating substrates. *Nano Lett.* **2012,** *12* (3), 1538-1544.

12. Gong, Y.; Lei, S.; Ye, G.; Li, B.; He, Y.; Keyshar, K.; Zhang, X.; Wang, Q.; Lou, J.; Liu, Z., Two-step growth of two-dimensional $WSe_2/MoSe_2$ heterostructures. *Nano Lett.* **2015,** *15* (9), 6135-6141.

13. Zhang, Z.; Chen, P.; Duan, X.; Zang, K.; Luo, J.; Duan, X., Robust epitaxial growth of two-dimensional heterostructures, multiheterostructures, and superlattices. *Science* **2017,** *357* (6353), 788-792.

14. Ali, M. N.; Xiong, J.; Flynn, S.; Tao, J.; Gibson, Q. D.; Schoop, L. M.; Liang, T.; Haldolaarachchige, N.; Hirschberger, M.; Ong, N., Large, non-saturating magnetoresistance in WTe$_2$. *Nature* **2014,** *514* (7521), 205.

15. Naylor, C. H.; Parkin, W. M.; Gao, Z.; Kang, H.; Noyan, M.; Wexler, R. B.; Tan, L. Z.; Kim, Y.; Kehayias, C. E.; Streller, F., Large-area synthesis of high-quality monolayer 1T'-WTe$_2$ flakes. *2D Mater.* **2017,** *4* (2), 021008.

16. Yun, S. J.; Han, G. H.; Kim, H.; Duong, D. L.; Shin, B. G.; Zhao, J.; Vu, Q. A.; Lee, J.; Lee, S. M.; Lee, Y. H., Telluriding monolayer MoS$_2$ and WS$_2$ via alkali metal scooter. *Nat. Commun.* **2017,** *8* (1), 2163.

17. Kwak, J.; Jo, Y.; Song, S.; Kim, J. H.; Kim, S. Y.; Lee, J. U.; Lee, S.; Park, J.; Kim, K.; Lee, G. D., Single-Crystalline Nanobelts Composed of Transition Metal Ditellurides. *Adv. Mater.* **2018,** *30* (30), 1707260.

18. Zhou, J.; Lin, J.; Huang, X.; Zhou, Y.; Chen, Y.; Xia, J.; Wang, H.; Xie, Y.; Yu, H.; Lei, J., A library of atomically thin metal chalcogenides. *Nature* **2018,** *556* (7701), 355.

19. Gong, Y.; Ye, G.; Lei, S.; Shi, G.; He, Y.; Lin, J.; Zhang, X.; Vajtai, R.; Pantelides, S. T.; Zhou, W., Synthesis of Millimeter-Scale Transition Metal Dichalcogenides Single Crystals. *Adv. Funct. Mater.* **2016,** *26* (12), 2009-2015.

20. Fan, X.; Zhao, Y.; Zheng, W.; Li, H.; Wu, X.; Hu, X.; Zhang, X.; Zhu, X.; Zhang, Q.; Wang, X., Controllable growth and formation mechanisms of dislocated WS$_2$ spirals. *Nano Lett.* **2018,** *18* (6), 3885-3892.

21. Grove, A. S., *Physics and technology of semiconductor devices*. Wiley: 1967.

22. Hussain, S.; Shehzad, M. A.; Vikraman, D.; Khan, M. F.; Singh, J.; Choi, D.-C.; Seo, Y.; Eom, J.; Lee, W.-G.; Jung, J., Synthesis and characterization of large-area and continuous MoS$_2$ atomic layers by RF magnetron sputtering. *Nanoscale* **2016,** *8* (7), 4340-4347.

23. Zhou, L.; Zubair, A.; Wang, Z.; Zhang, X.; Ouyang, F.; Xu, K.; Fang, W.; Ueno, K.; Li, J.; Palacios, T.; Kong, J.; Dresselhaus, M. S., Synthesis of High-Quality Large-Area Homogenous 1T′ MoTe$_2$ from Chemical Vapor Deposition. *Adv. Mater.* **2016,** *28* (43), 9526-9531.

24. Kim, S.-Y.; Kwak, J.; Ciobanu, C. V.; Kwon, S.-Y., Recent Developments in Controlled Vapor-Phase Growth of 2D Group 6 Transition Metal Dichalcogenides. *Adv. Mater.* **2019,** *31* (20), 1804939.

25. Wang, S.; Rong, Y.; Fan, Y.; Pacios, M.; Bhaskaran, H.; He, K.; Warner, J. H., Shape evolution of monolayer MoS$_2$ crystals grown by chemical vapor deposition. *Chem. Mater.* **2014,** *26* (22), 6371-6379.

26. Ago, H.; Fukamachi, S.; Endo, H.; Solís-Fernández, P.; Mohamad Yunus, R.; Uchida, Y.; Panchal, V.; Kazakova, O.; Tsuji, M., Visualization of Grain Structure and Boundaries of Polycrystalline Graphene and Two-Dimensional Materials by Epitaxial Growth of Transition Metal Dichalcogenides. *ACS Nano* **2016,** *10* (3), 3233-3240.

27. Lee, C.; Wei, X.; Kysar, J. W.; Hone, J., Measurement of the elastic properties and intrinsic strength of monolayer graphene. *Science* **2008,** *321* (5887), 385-388.

28. Balandin, A. A.; Ghosh, S.; Bao, W.; Calizo, I.; Teweldebrhan, D.; Miao, F.; Lau, C. N., Superior thermal conductivity of single-layer graphene. *Nano Lett.* **2008,** *8* (3), 902-907.

29. Kwak, J.; Kim, S. Y.; Jo, Y.; Kim, N. Y.; Kim, S. Y.; Lee, Z.; Kwon, S. Y., Unraveling the Water Impermeability Discrepancy in CVD-Grown Graphene. *Adv. Mater.* **2018,** *30* (30), 1800022.

30. Kwon, S.-Y.; Ciobanu, C. V.; Petrova, V.; Shenoy, V. B.; Bareno, J.; Gambin, V.; Petrov, I.; Kodambaka, S., Growth of semiconducting graphene on palladium. *Nano Lett.* **2009,** *9* (12), 3985-3990.

31. Balog, R.; Jørgensen, B.; Nilsson, L.; Andersen, M.; Rienks, E.; Bianchi, M.; Fanetti, M.; Lægsgaard, E.; Baraldi, A.; Lizzit, S., Bandgap opening in graphene induced by patterned hydrogen adsorption. *Nat. Mater.* **2010,** *9* (4), 315.

32. Zhou, S. Y.; Gweon, G.-H.; Fedorov, A.; First, P., de; De Heer, W.; Lee, D.-H.; Guinea, F.; Neto, A. C.; Lanzara, A., Substrate-induced bandgap opening in epitaxial graphene. *Nat. Mater.* **2007,** *6* (10), 770.

33. Splendiani, A.; Sun, L.; Zhang, Y.; Li, T.; Kim, J.; Chim, C.-Y.; Galli, G.; Wang, F., Emerging photoluminescence in monolayer MoS_2. *Nano Lett.* **2010,** *10* (4), 1271-1275.

34. Komsa, H.-P.; Krasheninnikov, A. V., Effects of confinement and environment on the electronic structure and exciton binding energy of MoS_2 from first principles. *Phys. Rev. B* **2012,** *86* (24), 241201.

35. Wang, X.; Gong, Y.; Shi, G.; Chow, W. L.; Keyshar, K.; Ye, G.; Vajtai, R.; Lou, J.; Liu, Z.; Ringe, E., Chemical vapor deposition growth of crystalline monolayer $MoSe_2$. *ACS Nano* **2014,** *8* (5), 5125-5131.

36. Chen, K.; Chen, Z.; Wan, X.; Zheng, Z.; Xie, F.; Chen, W.; Gui, X.; Chen, H.; Xie, W.; Xu, J., A Simple Method for Synthesis of High-Quality Millimeter-Scale 1T′ Transition-Metal Telluride and Near-Field Nanooptical Properties. *Adv. Mater.* **2017,** *29* (38), 1700704.

37. Najmaei, S.; Liu, Z.; Zhou, W.; Zou, X.; Shi, G.; Lei, S.; Yakobson, B. I.; Idrobo, J.-C.; Ajayan, P. M.; Lou, J., Vapour phase growth and grain boundary structure of molybdenum disulphide atomic layers. *Nat. Mater.* **2013,** *12* (8), 754.

38. Kwak, J.; Jo, Y.; Park, S.-D.; Kim, N. Y.; Kim, S.-Y.; Shin, H.-J.; Lee, Z.; Kim, S. Y.; Kwon, S.-Y., Oxidation behavior of graphene-coated copper at intrinsic graphene defects of different origins. *Nat. Commun.* **2017,** *8* (1), 1549.

39. Chen, L.; Liu, B.; Ge, M.; Ma, Y.; Abbas, A. N.; Zhou, C., Step-edge-guided nucleation and growth of aligned WSe$_2$ on sapphire via a layer-over-layer growth mode. *ACS Nano* **2015,** *9* (8), 8368-8375.

40. Ji, Q.; Zhang, Y.; Zhang, Y.; Liu, Z., Chemical vapour deposition of group-VIB metal dichalcogenide monolayers: engineered substrates from amorphous to single crystalline. *Chem. Soc. Rev.* **2015,** *44* (9), 2587-2602.

41. Ross, J. S.; Klement, P.; Jones, A. M.; Ghimire, N. J.; Yan, J.; Mandrus, D.; Taniguchi, T.; Watanabe, K.; Kitamura, K.; Yao, W., Electrically tunable excitonic light-emitting diodes based on monolayer WSe$_2$ p–n junctions. *Nat. Nanotechnol.* **2014,** *9* (4), 268.

42. Scardamaglia, M.; Struzzi, C.; Osella, S.; Reckinger, N.; Colomer, J.-F.; Petaccia, L.; Snyders, R.; Beljonne, D.; Bittencourt, C., Tuning nitrogen species to control the charge carrier concentration in highly doped graphene. *2D Mater.* **2016,** *3* (1), 011001.

43. Siao, M.; Shen, W.; Chen, R.; Chang, Z.; Shih, M.; Chiu, Y.; Cheng, C.-M., Two-dimensional electronic transport and surface electron accumulation in MoS$_2$. *Nat. Commun.* **2018,** *9* (1), 1442.

44. Xia, J.; Zhu, D.; Wang, L.; Huang, B.; Huang, X.; Meng, X. M., Large-Scale Growth of Two-Dimensional SnS$_2$ Crystals Driven by Screw Dislocations and Application to Photodetectors. *Adv. Funct. Mater.* **2015,** *25* (27), 4255-4261.

45. Zhang, Y.; Ji, Q.; Wen, J.; Li, J.; Li, C.; Shi, J.; Zhou, X.; Shi, K.; Chen, H.; Li, Y., Monolayer MoS$_2$ Dendrites on a Symmetry-Disparate SrTiO$_3$ (001) Substrate: Formation Mechanism and Interface Interaction. *Adv. Funct. Mater.* **2016,** *26* (19), 3299-3305.

46. Jin, S.; Bierman, M. J.; Morin, S. A., A new twist on nanowire formation: Screw-dislocation-driven growth of nanowires and nanotubes. *J. Phys. Chem. Lett.* **2010,** *1* (9), 1472-1480.

47. Meng, F.; Morin, S. A.; Forticaux, A.; Jin, S., Screw dislocation driven growth of nanomaterials. *Acc. Chem. Res.* **2013,** *46* (7), 1616-1626.

48. Chen, L.; Liu, B.; Abbas, A. N.; Ma, Y.; Fang, X.; Liu, Y.; Zhou, C., Screw-dislocation-driven growth of two-dimensional few-layer and pyramid-like WSe$_2$ by sulfur-assisted chemical vapor deposition. *ACS Nano* **2014,** *8* (11), 11543-11551.

49. Wu, J.; Hu, Z.; Jin, Z.; Lei, S.; Guo, H.; Chatterjee, K.; Zhang, J.; Yang, Y.; Li, B.; Liu, Y., Spiral growth of SnSe$_2$ crystals by chemical vapor deposition. *Adv. Mater. Interfaces* **2016,** *3* (16), 1600383.

50. Ly, T. H.; Zhao, J.; Kim, H.; Han, G. H.; Nam, H.; Lee, Y. H., Vertically conductive MoS$_2$ spiral pyramid. *Adv. Mater.* **2016,** *28* (35), 7723-7728.

51. Luo, Y.-R., *Comprehensive handbook of chemical bond energies*. CRC press: 2007.

52. Muñoz, R.; Gómez-Aleixandre, C., Review of CVD synthesis of graphene. *Chem. Vap. Deposition* **2013,** *19* (10-11-12), 297-322.

53. Wei, D.; Liu, Y.; Wang, Y.; Zhang, H.; Huang, L.; Yu, G., Synthesis of N-doped graphene by chemical vapor deposition and its electrical properties. *Nano Lett.* **2009,** *9* (5), 1752-1758.

54. Lv, R.; Li, Q.; Botello-Méndez, A. R.; Hayashi, T.; Wang, B.; Berkdemir, A.; Hao, Q.; Elías, A. L.; Cruz-Silva, R.; Gutiérrez, H. R., Nitrogen-doped graphene: beyond single substitution and enhanced molecular sensing. *Sci. Rep.* **2012,** *2*, 586.

55. Zhang, Y.; Zhang, Y.; Ji, Q.; Ju, J.; Yuan, H.; Shi, J.; Gao, T.; Ma, D.; Liu, M.; Chen, Y., Controlled growth of high-quality monolayer WS_2 layers on sapphire and imaging its grain boundary. *ACS Nano* **2013,** *7* (10), 8963-8971.

56. Eichfeld, S. M.; Hossain, L.; Lin, Y.-C.; Piasecki, A. F.; Kupp, B.; Birdwell, A. G.; Burke, R. A.; Lu, N.; Peng, X.; Li, J., Highly scalable, atomically thin WSe_2 grown via metal–organic chemical vapor deposition. *ACS Nano* **2015,** *9* (2), 2080-2087.

57. Ohring, M., *Materials science of thin films*. Elsevier: 2001.

58. Yu, Y.; Li, C.; Liu, Y.; Su, L.; Zhang, Y.; Cao, L., Controlled scalable synthesis of uniform, high-quality monolayer and few-layer MoS_2 films. *Sci. Rep.* **2013,** *3*, 1866.

59. Shi, J.; Zhang, X.; Ma, D.; Zhu, J.; Zhang, Y.; Guo, Z.; Yao, Y.; Ji, Q.; Song, X.; Zhang, Y.; Li, C.; Liu, Z.; Zhu, W.; Zhang, Y., Substrate Facet Effect on the Growth of Monolayer MoS_2 on Au Foils. *ACS Nano* **2015,** *9* (4), 4017-4025.

60. Wang, S. S.; Pacios, M.; Bhaskaran, H.; Warner, J. H., Substrate control for large area continuous films of monolayer MoS_2 by atmospheric pressure chemical vapor deposition. *Nanotechnology* **2016,** *27* (8).

61. Tarasov, A.; Campbell, P. M.; Tsai, M.-Y.; Hesabi, Z. R.; Feirer, J.; Graham, S.; Ready, W. J.; Vogel, E. M., Highly Uniform Trilayer Molybdenum Disulfide for Wafer-Scale Device Fabrication. *Adv. Funct. Mater.* **2014,** *24* (40), 6389-6400.

62. Zhan, Y.; Liu, Z.; Najmaei, S.; Ajayan, P. M.; Lou, J., Large-Area Vapor-Phase Growth and Characterization of MoS_2 Atomic Layers on a SiO_2 Substrate. *Small* **2012,** *8* (7), 966-971.

63. Lin, Y.-C.; Zhang, W.; Huang, J.-K.; Liu, K.-K.; Lee, Y.-H.; Liang, C.-T.; Chu, C.-W.; Li, L.-J., Wafer-scale MoS_2 thin layers prepared by MoO3 sulfurization. *Nanoscale* **2012,** *4* (20), 6637-6641.

64. Chow, P. K.; Singh, E.; Viana, B. C.; Gao, J.; Luo, J.; Li, J.; Lin, Z.; Elías, A. L.; Shi, Y.; Wang, Z.; Terrones, M.; Koratkar, N., Wetting of Mono and Few-Layered WS_2 and MoS_2 Films Supported on Si/SiO_2 Substrates. *ACS Nano* **2015,** *9* (3), 3023-3031.

65. Duerloo, K.-A. N.; Li, Y.; Reed, E. J., Structural phase transitions in two-dimensional Mo- and W-dichalcogenide monolayers. *Nat. Commun.* **2014,** *5*, 4214.

66. Keum, D. H.; Cho, S.; Kim, J. H.; Choe, D.-H.; Sung, H.-J.; Kan, M.; Kang, H.; Hwang, J.-Y.; Kim, S. W.; Yang, H.; Chang, K. J.; Lee, Y. H., Bandgap opening in few-layered monoclinic $MoTe_2$. *Nat. Phys.* **2015,** *11*, 482.

67. Song, J.-G.; Park, J.; Lee, W.; Choi, T.; Jung, H.; Lee, C. W.; Hwang, S.-H.; Myoung, J. M.; Jung, J.-H.; Kim, S.-H., Layer-controlled, wafer-scale, and conformal synthesis of tungsten disulfide nanosheets using atomic layer deposition. *ACS Nano* **2013,** *7* (12), 11333-11340.

68. Tai, G.; Zeng, T.; Yu, J.; Zhou, J.; You, Y.; Wang, X.; Wu, H.; Sun, X.; Hu, T.; Guo, W., Fast and large-area growth of uniform MoS$_2$ monolayers on molybdenum foils. *Nanoscale* **2016,** *8* (4), 2234-2241.

69. Tai, G. a.; Wang, K.; Sun, Z.; Yin, J.; Ng, S. M.; Zhou, J.; Yan, F.; Leung, C. W.; Wong, K. H.; Guo, W., Nonlithographic fabrication of crystalline silicon nanodots on graphene. *J. Phys. Chem. C* **2011,** *116* (1), 532-537.

70. Antczak, G.; Ehrlich, G., *Surface diffusion: metals, metal atoms, and clusters*. Cambridge University Press: 2010.

71. Govind Rajan, A.; Warner, J. H.; Blankschtein, D.; Strano, M. S., Generalized mechanistic model for the chemical vapor deposition of 2D transition metal dichalcogenide monolayers. *ACS Nano* **2016,** *10* (4), 4330-4344.

72. Chen, J.; Zhao, X.; Tan, S. J.; Xu, H.; Wu, B.; Liu, B.; Fu, D.; Fu, W.; Geng, D.; Liu, Y., Chemical vapor deposition of large-size monolayer MoSe$_2$ crystals on molten glass. *J. Am. Chem. Soc.* **2017,** *139* (3), 1073-1076.

73. Lee, J.; Pak, S.; Giraud, P.; Lee, Y. W.; Cho, Y.; Hong, J.; Jang, A. R.; Chung, H. S.; Hong, W. K.; Jeong, H. Y., Thermodynamically Stable Synthesis of Large-Scale and Highly Crystalline Transition Metal Dichalcogenide Monolayers and their Unipolar n–n Heterojunction Devices. *Adv. Mater.* **2017,** *29* (33), 1702206.

74. Van Der Zande, A. M.; Huang, P. Y.; Chenet, D. A.; Berkelbach, T. C.; You, Y.; Lee, G.-H.; Heinz, T. F.; Reichman, D. R.; Muller, D. A.; Hone, J. C., Grains and grain boundaries in highly crystalline monolayer molybdenum disulphide. *Nat. Mater.* **2013,** *12* (6), 554.

75. Ling, X.; Lee, Y.-H.; Lin, Y.; Fang, W.; Yu, L.; Dresselhaus, M. S.; Kong, J., Role of the Seeding Promoter in MoS$_2$ Growth by Chemical Vapor Deposition. *Nano Lett.* **2014,** *14* (2), 464-472.

76. Özden, A.; Ay, F.; Sevik, C.; Perkgöz, N. K., CVD growth of monolayer MoS$_2$: Role of growth zone configuration and precursors ratio. *Jpn. J. Appl. Phys.* **2017,** *56* (6S1), 06GG05.

77. Wang, S.; Pacios, M.; Bhaskaran, H.; Warner, J. H., Substrate control for large area continuous films of monolayer MoS$_2$ by atmospheric pressure chemical vapor deposition. *Nanotechnology* **2016,** *27* (8), 085604.

78. Lee, W. Y.; Besmann, T. M.; Stott, M. W., Preparation of MoS$_2$ thin films by chemical vapor deposition. *J. Mater. Res.* **2011,** *9* (6), 1474-1483.

79. Yu, Y.; Li, C.; Liu, Y.; Su, L.; Zhang, Y.; Cao, L., Controlled Scalable Synthesis of Uniform, High-Quality Monolayer and Few-layer MoS$_2$ Films. *Sci. Rep.* **2013,** *3*, 1866.

80. O'Brien, M.; McEvoy, N.; Hallam, T.; Kim, H.-Y.; Berner, N. C.; Hanlon, D.; Lee, K.; Coleman, J. N.; Duesberg, G. S., Transition Metal Dichalcogenide Growth via Close Proximity Precursor Supply. *Sci. Rep.* **2014,** *4*, 7374.

81. Lee, Y.; Lee, J.; Bark, H.; Oh, I.-K.; Ryu, G. H.; Lee, Z.; Kim, H.; Cho, J. H.; Ahn, J.-H.; Lee, C., Synthesis of wafer-scale uniform molybdenum disulfide films with control over the layer number using a gas phase sulfur precursor. *Nanoscale* **2014,** *6* (5), 2821-2826.

82. Lee, K. J.; Lee, J.; Hwang, H.; Reitmeier, Z. J.; Davis, R. F.; Rogers, J. A.; Nuzzo, R. G., A Printable Form of Single-Crystalline Gallium Nitride for Flexible Optoelectronic Systems. *Small* **2005,** *1* (12), 1164-1168.

83. Kalanyan, B.; Kimes, W. A.; Beams, R.; Stranick, S. J.; Garratt, E.; Kalish, I.; Davydov, A. V.; Kanjolia, R. K.; Maslar, J. E., Rapid Wafer-Scale Growth of Polycrystalline 2H-MoS$_2$ by Pulsed Metalorganic Chemical Vapor Deposition. *Chem. Mater.* **2017,** *29* (15), 6279-6288.

84. Yu, W. J.; Li, Z.; Zhou, H.; Chen, Y.; Wang, Y.; Huang, Y.; Duan, X., Vertically stacked multi-heterostructures of layered materials for logic transistors and complementary inverters. *Nat. Mater.* **2012,** *12*, 246.

85. Chiu, M.-H.; Zhang, C.; Shiu, H.-W.; Chuu, C.-P.; Chen, C.-H.; Chang, C.-Y. S.; Chen, C.-H.; Chou, M.-Y.; Shih, C.-K.; Li, L.-J., Determination of band alignment in the single-layer MoS$_2$/WSe$_2$ heterojunction. *Nat. Commun.* **2015,** *6*, 7666.

86. Yang, W.; Chen, G.; Shi, Z.; Liu, C.-C.; Zhang, L.; Xie, G.; Cheng, M.; Wang, D.; Yang, R.; Shi, D.; Watanabe, K.; Taniguchi, T.; Yao, Y.; Zhang, Y.; Zhang, G., Epitaxial growth of single-domain graphene on hexagonal boron nitride. *Nat. Mater.* **2013,** *12*, 792.

87. Lin, Y.-C.; Ghosh, R. K.; Addou, R.; Lu, N.; Eichfeld, S. M.; Zhu, H.; Li, M.-Y.; Peng, X.; Kim, M. J.; Li, L.-J.; Wallace, R. M.; Datta, S.; Robinson, J. A., Atomically thin resonant tunnel diodes built from synthetic van der Waals heterostructures. *Nat. Commun.* **2015,** *6*, 7311.

88. Yu, Y.; Hu, S.; Su, L.; Huang, L.; Liu, Y.; Jin, Z.; Purezky, A. A.; Geohegan, D. B.; Kim, K. W.; Zhang, Y.; Cao, L., Equally Efficient Interlayer Exciton Relaxation and Improved Absorption in Epitaxial and Nonepitaxial MoS$_2$/WS$_2$ Heterostructures. *Nano Lett.* **2015,** *15* (1), 486-491.

89. Gong, Y.; Lei, S.; Ye, G.; Li, B.; He, Y.; Keyshar, K.; Zhang, X.; Wang, Q.; Lou, J.; Liu, Z.; Vajtai, R.; Zhou, W.; Ajayan, P. M., Two-Step Growth of Two-Dimensional WSe$_2$/MoSe$_2$ Heterostructures. *Nano Lett.* **2015,** *15* (9), 6135-6141.

90. Choudhary, N.; Park, J.; Hwang, J. Y.; Chung, H.-S.; Dumas, K. H.; Khondaker, S. I.; Choi, W.; Jung, Y., Centimeter Scale Patterned Growth of Vertically Stacked Few Layer Only 2D MoS$_2$/WS$_2$ van der Waals Heterostructure. *Sci. Rep.* **2016,** *6*, 25456.

91. Xue, Y.; Zhang, Y.; Liu, Y.; Liu, H.; Song, J.; Sophia, J.; Liu, J.; Xu, Z.; Xu, Q.; Wang, Z.; Zheng, J.; Liu, Y.; Li, S.; Bao, Q., Scalable Production of a Few-Layer MoS$_2$/WS$_2$ Vertical Heterojunction Array and Its Application for Photodetectors. *ACS Nano* **2016,** *10* (1), 573-580.

92. Li, Y.; Qin, J.-K.; Xu, C.-Y.; Cao, J.; Sun, Z.-Y.; Ma, L.-P.; Hu, P. A.; Ren, W.; Zhen, L., Electric Field Tunable Interlayer Relaxation Process and Interlayer Coupling in WSe_2/Graphene Heterostructures. *Adv. Funct. Mater.* **2016,** *26* (24), 4319-4328.

93. Georgiou, T.; Jalil, R.; Belle, B. D.; Britnell, L.; Gorbachev, R. V.; Morozov, S. V.; Kim, Y.-J.; Gholinia, A.; Haigh, S. J.; Makarovsky, O.; Eaves, L.; Ponomarenko, L. A.; Geim, A. K.; Novoselov, K. S.; Mishchenko, A., Vertical field-effect transistor based on graphene–WS_2 heterostructures for flexible and transparent electronics. *Nat. Nanotechnol.* **2012,** *8*, 100.

94. Wang, S.; Wang, X.; Warner, J. H., All Chemical Vapor Deposition Growth of MoS_2:h-BN Vertical van der Waals Heterostructures. *ACS Nano* **2015,** *9* (5), 5246-5254.

95. Uchida, Y.; Nakandakari, S.; Kawahara, K.; Yamasaki, S.; Mitsuhara, M.; Ago, H., Controlled Growth of Large-Area Uniform Multilayer Hexagonal Boron Nitride as an Effective 2D Substrate. *ACS Nano* **2018,** *12* (6), 6236-6244.

96. Ago, H.; Endo, H.; Solís-Fernández, P.; Takizawa, R.; Ohta, Y.; Fujita, Y.; Yamamoto, K.; Tsuji, M., Controlled van der Waals Epitaxy of Monolayer MoS_2 Triangular Domains on Graphene. *ACS Appl. Mater. Interfaces* **2015,** *7* (9), 5265-5273.

97. Yan, A.; Velasco, J.; Kahn, S.; Watanabe, K.; Taniguchi, T.; Wang, F.; Crommie, M. F.; Zettl, A., Direct Growth of Single- and Few-Layer MoS_2 on h-BN with Preferred Relative Rotation Angles. *Nano Lett.* **2015,** *15* (10), 6324-6331.

98. Kobayashi, Y.; Sasaki, S.; Mori, S.; Hibino, H.; Liu, Z.; Watanabe, K.; Taniguchi, T.; Suenaga, K.; Maniwa, Y.; Miyata, Y., Growth and Optical Properties of High-Quality Monolayer WS_2 on Graphite. *ACS Nano* **2015,** *9* (4), 4056-4063.

99. Jo, S.; Ubrig, N.; Berger, H.; Kuzmenko, A. B.; Morpurgo, A. F., Mono- and Bilayer WS_2 Light-Emitting Transistors. *Nano Lett.* **2014,** *14* (4), 2019-2025.

100. Shi, Y.; Zhou, W.; Lu, A.-Y.; Fang, W.; Lee, Y.-H.; Hsu, A. L.; Kim, S. M.; Kim, K. K.; Yang, H. Y.; Li, L.-J.; Idrobo, J.-C.; Kong, J., van der Waals Epitaxy of MoS_2 Layers Using Graphene As Growth Templates. *Nano Lett.* **2012,** *12* (6), 2784-2791.

101. Kim, Y.-T.; Han, J. H.; Hong, B. H.; Kwon, Y.-U., Electrochemical Synthesis of CdSe Quantum-Dot Arrays on a Graphene Basal Plane Using Mesoporous Silica Thin-Film Templates. *Adv. Mater.* **2010,** *22* (4), 515-518.

102. Yu, S. U.; Park, B.; Cho, Y.; Hyun, S.; Kim, J. K.; Kim, K. S., Simultaneous Visualization of Graphene Grain Boundaries and Wrinkles with Structural Information by Gold Deposition. *ACS Nano* **2014,** *8* (8), 8662-8668.

103. Britnell, L.; Ribeiro, R.; Eckmann, A.; Jalil, R.; Belle, B.; Mishchenko, A.; Kim, Y.-J.; Gorbachev, R.; Georgiou, T.; Morozov, S., Strong light-matter interactions in heterostructures of atomically thin films. *Science* **2013,** *340* (6138), 1311-1314.

104. Yu, W. J.; Liu, Y.; Zhou, H.; Yin, A.; Li, Z.; Huang, Y.; Duan, X., Highly efficient gate-tunable photocurrent generation in vertical heterostructures of layered materials. *Nat. Nanotechnol.* **2013,** *8* (12), 952.

105. Subhedar, K. M.; Sharma, I.; Dhakate, S. R., Control of layer stacking in CVD graphene under quasi-static condition. *PCCP* **2015,** *17* (34), 22304-22310.

106. Fang, W.; Hsu, A. L.; Song, Y.; Birdwell, A. G.; Amani, M.; Dubey, M.; Dresselhaus, M. S.; Palacios, T.; Kong, J., Asymmetric growth of bilayer graphene on copper enclosures using low-pressure chemical vapor deposition. *ACS Nano* **2014,** *8* (6), 6491-6499.

107. Zeng, H.; Liu, G.-B.; Dai, J.; Yan, Y.; Zhu, B.; He, R.; Xie, L.; Xu, S.; Chen, X.; Yao, W., Optical signature of symmetry variations and spin-valley coupling in atomically thin tungsten dichalcogenides. *Sci. Rep.* **2013,** *3*, 1608.

108. Buscema, M.; Steele, G. A.; van der Zant, H. S.; Castellanos-Gomez, A., The effect of the substrate on the Raman and photoluminescence emission of single-layer MoS_2. *Nano Res.* **2014,** *7* (4), 561-571.

109. Cardona, M.; Meyer, T.; Thewalt, M., Temperature dependence of the energy gap of semiconductors in the low-temperature limit. *Phys. Rev. Lett.* **2004,** *92* (19), 196403.

110. Zhu, B.; Chen, X.; Cui, X., Exciton binding energy of monolayer WS_2. *Sci. Rep.* **2015,** *5*, 9218.

111. Chow, P. K.; Jacobs-Gedrim, R. B.; Gao, J.; Lu, T.-M.; Yu, B.; Terrones, H.; Koratkar, N., Defect-induced photoluminescence in monolayer semiconducting transition metal dichalcogenides. *ACS Nano* **2015,** *9* (2), 1520-1527.

112. Bromley, R.; Murray, R.; Yoffe, A., The band structures of some transition metal dichalcogenides. III. Group VIA: trigonal prism materials. *J. Phys. Condens. Matter* **1972,** *5* (7), 759.

113. Mattheiss, L., Band structures of transition-metal-dichalcogenide layer compounds. *Phys. Rev. B* **1973,** *8* (8), 3719.

114. Ramasubramaniam, A., Large excitonic effects in monolayers of molybdenum and tungsten dichalcogenides. *Phys. Rev. B* **2012,** *86* (11), 115409.

115. Yun, S. J.; Chae, S. H.; Kim, H.; Park, J. C.; Park, J.-H.; Han, G. H.; Lee, J. S.; Kim, S. M.; Oh, H. M.; Seok, J., Synthesis of centimeter-scale monolayer tungsten disulfide film on gold foils. *ACS Nano* **2015,** *9* (5), 5510-5519.

116. Kim, H.; Ovchinnikov, D.; Deiana, D.; Unuchek, D.; Kis, A., Suppressing Nucleation in Metal–Organic Chemical Vapor Deposition of MoS_2 Monolayers by Alkali Metal Halides. *Nano Lett.* **2017,** *17* (8), 5056-5063.

117. Fang, H.; Tosun, M.; Seol, G.; Chang, T. C.; Takei, K.; Guo, J.; Javey, A., Degenerate n-doping of few-layer transition metal dichalcogenides by potassium. *Nano Lett.* **2013,** *13* (5), 1991-1995.

118. Britnell, L.; Gorbachev, R.; Jalil, R.; Belle, B.; Schedin, F.; Mishchenko, A.; Georgiou, T.; Katsnelson, M.; Eaves, L.; Morozov, S., Field-effect tunneling transistor based on vertical graphene heterostructures. *Science* **2012,** *335* (6071), 947-950.

119. Haigh, S.; Gholinia, A.; Jalil, R.; Romani, S.; Britnell, L.; Elias, D.; Novoselov, K.; Ponomarenko, L.; Geim, A.; Gorbachev, R., Cross-sectional imaging of individual layers and buried interfaces of graphene-based heterostructures and superlattices. *Nat. Mater.* **2012,** *11* (9), 764.

120. Wood, J. D.; Wells, S. A.; Jariwala, D.; Chen, K.-S.; Cho, E.; Sangwan, V. K.; Liu, X.; Lauhon, L. J.; Marks, T. J.; Hersam, M. C., Effective passivation of exfoliated black phosphorus transistors against ambient degradation. *Nano Lett.* **2014,** *14* (12), 6964-6970.

121. Li, Y.; Zhou, Z.; Zhang, S.; Chen, Z., MoS2 nanoribbons: high stability and unusual electronic and magnetic properties. *J. Am. Chem. Soc.* **2008,** *130* (49), 16739-16744.

122. Ly, T. H.; Chiu, M.-H.; Li, M.-Y.; Zhao, J.; Perello, D. J.; Cichocka, M. O.; Oh, H. M.; Chae, S. H.; Jeong, H. Y.; Yao, F., Observing grain boundaries in CVD-grown monolayer transition metal dichalcogenides. *ACS Nano* **2014,** *8* (11), 11401-11408.

123. Gao, J.; Li, B.; Tan, J.; Chow, P.; Lu, T.-M.; Koratkar, N., Aging of transition metal dichalcogenide monolayers. *ACS Nano* **2016,** *10* (2), 2628-2635.

124. N'Diaye, M.; Pascaretti-Grizon, F.; Massin, P.; Baslé, M. F.; Chappard, D., Water absorption of poly (methyl methacrylate) measured by vertical interference microscopy. *Langmuir* **2012,** *28* (31), 11609-11614.

125. Lee, G.-H.; Cui, X.; Kim, Y. D.; Arefe, G.; Zhang, X.; Lee, C.-H.; Ye, F.; Watanabe, K.; Taniguchi, T.; Kim, P., Highly stable, dual-gated MoS$_2$ transistors encapsulated by hexagonal boron nitride with gate-controllable contact, resistance, and threshold voltage. *ACS Nano* **2015,** *9* (7), 7019-7026.

126. Chang, H.-Y.; Yang, S.; Lee, J.; Tao, L.; Hwang, W.-S.; Jena, D.; Lu, N.; Akinwande, D., High-performance, highly bendable MoS$_2$ transistors with high-k dielectrics for flexible low-power systems. *ACS Nano* **2013,** *7* (6), 5446-5452.

127. Lin, Y.-C.; Lu, N.; Perea-Lopez, N.; Li, J.; Lin, Z.; Peng, X.; Lee, C. H.; Sun, C.; Calderin, L.; Browning, P. N.; Bresnehan, M. S.; Kim, M. J.; Mayer, T. S.; Terrones, M.; Robinson, J. A., Direct Synthesis of van der Waals Solids. *ACS Nano* **2014,** *8* (4), 3715-3723.

128. Chen, X.; Shinde, S. M.; Dhakal, K. P.; Lee, S. W.; Kim, H.; Lee, Z.; Ahn, J.-H., Degradation behaviors and mechanisms of MoS$_2$ crystals relevant to bioabsorbable electronics. *NPG Asia Mater.* **2018,** *10* (8), 810-820.

129. KC, S.; Longo, R. C.; Wallace, R. M.; Cho, K., Surface oxidation energetics and kinetics on MoS$_2$ monolayer. *J. Appl. Phys.* **2015,** *117* (13), 135301.

130. Kim, S.-Y.; Kwak, J.; Kim, J. H.; Lee, J.-U.; Jo, Y.; Youb Kim, S.; Cheong, H.; Lee, Z.; Kwon, S.-Y., Substantial improvements of long-term stability in encapsulation-free WS$_2$ using highly interacting graphene substrate. *2D Mater.* **2017,** *4* (1).

131. Zhou, H.; Yu, F.; Liu, Y.; Zou, X.; Cong, C.; Qiu, C.; Yu, T.; Yan, Z.; Shen, X.; Sun, L., Thickness-dependent patterning of MoS$_2$ sheets with well-oriented triangular pits by heating in air. *Nano Res.* **2013,** *6* (10), 703-711.

132. Ghatak, S.; Pal, A. N.; Ghosh, A., Nature of Electronic States in Atomically Thin MoS$_2$ Field-Effect Transistors. *ACS Nano* **2011,** *5* (10), 7707-7712.

133. Ferrari, A. C.; Meyer, J. C.; Scardaci, V.; Casiraghi, C.; Lazzeri, M.; Mauri, F.; Piscanec, S.; Jiang, D.; Novoselov, K. S.; Roth, S.; Geim, A. K., Raman Spectrum of Graphene and Graphene Layers. *Phys. Rev. Lett.* **2006,** *97* (18), 187401.

134. Komsa, H.-P.; Kurasch, S.; Lehtinen, O.; Kaiser, U.; Krasheninnikov, A. V., From point to extended defects in two-dimensional MoS$_2$: Evolution of atomic structure under electron irradiation. *Phys. Rev. B* **2013,** *88* (3), 035301.

135. Lin, Y.-C.; Chang, C.-Y. S.; Ghosh, R. K.; Li, J.; Zhu, H.; Addou, R.; Diaconescu, B.; Ohta, T.; Peng, X.; Lu, N.; Kim, M. J.; Robinson, J. T.; Wallace, R. M.; Mayer, T. S.; Datta, S.; Li, L.-J.; Robinson, J. A., Atomically Thin Heterostructures Based on Single-Layer Tungsten Diselenide and Graphene. *Nano Lett.* **2014,** *14* (12), 6936-6941.

136. Giusca, C. E.; Rungger, I.; Panchal, V.; Melios, C.; Lin, Z.; Lin, Y.-C.; Kahn, E.; Elías, A. L.; Robinson, J. A.; Terrones, M.; Kazakova, O., Excitonic Effects in Tungsten Disulfide Monolayers on Two-Layer Graphene. *ACS Nano* **2016,** *10* (8), 7840-7846.

137. Yang, L.; Majumdar, K.; Liu, H.; Du, Y.; Wu, H.; Hatzistergos, M.; Hung, P. Y.; Tieckelmann, R.; Tsai, W.; Hobbs, C.; Ye, P. D., Chloride Molecular Doping Technique on 2D Materials: WS$_2$ and MoS$_2$. *Nano Lett.* **2014,** *14* (11), 6275-6280.

138. Sim, D. M.; Kim, M.; Yim, S.; Choi, M.-J.; Choi, J.; Yoo, S.; Jung, Y. S., Controlled Doping of Vacancy-Containing Few-Layer MoS2 via Highly Stable Thiol-Based Molecular Chemisorption. *ACS Nano* **2015,** *9* (12), 12115-12123.

139. Mak, K. F.; He, K.; Lee, C.; Lee, G. H.; Hone, J.; Heinz, T. F.; Shan, J., Tightly bound trions in monolayer MoS$_2$. *Nat. Mater.* **2012,** *12*, 207.

140. Gutiérrez, H. R.; Perea-López, N.; Elías, A. L.; Berkdemir, A.; Wang, B.; Lv, R.; López-Urías, F.; Crespi, V. H.; Terrones, H.; Terrones, M., Extraordinary Room-Temperature Photoluminescence in Triangular WS$_2$ Monolayers. *Nano Lett.* **2013,** *13* (8), 3447-3454.

141. Zan, R.; Ramasse, Q. M.; Jalil, R.; Georgiou, T.; Bangert, U.; Novoselov, K. S., Control of Radiation Damage in MoS$_2$ by Graphene Encapsulation. *ACS Nano* **2013,** *7* (11), 10167-10174.

142. Kim, S.-Y.; Kim, J. H.; Lee, S.; Kwak, J.; Jo, Y.; Yoon, E.; Lee, G.-D.; Lee, Z.; Kwon, S.-Y., The impact of substrate surface defects on the properties of two-dimensional van der Waals heterostructures. *Nanoscale* **2018,** *10* (40), 19212-19219.

143. Wang, L.; Meric, I.; Huang, P.; Gao, Q.; Gao, Y.; Tran, H.; Taniguchi, T.; Watanabe, K.; Campos, L.; Muller, D., One-dimensional electrical contact to a two-dimensional material. *Science* **2013,** *342* (6158), 614-617.

144. Deng, Y.; Luo, Z.; Conrad, N. J.; Liu, H.; Gong, Y.; Najmaei, S.; Ajayan, P. M.; Lou, J.; Xu, X.; Ye, P. D., Black phosphorus–monolayer MoS_2 van der Waals heterojunction p–n diode. *ACS Nano* **2014,** *8* (8), 8292-8299.

145. Duan, X.; Wang, C.; Shaw, J. C.; Cheng, R.; Chen, Y.; Li, H.; Wu, X.; Tang, Y.; Zhang, Q.; Pan, A., Lateral epitaxial growth of two-dimensional layered semiconductor heterojunctions. *Nat. Nanotechnol.* **2014,** *9* (12), 1024.

146. Zhou, W.; Zou, X.; Najmaei, S.; Liu, Z.; Shi, Y.; Kong, J.; Lou, J.; Ajayan, P. M.; Yakobson, B. I.; Idrobo, J.-C., Intrinsic structural defects in monolayer molybdenum disulfide. *Nano Lett.* **2013,** *13* (6), 2615-2622.

147. Bonaccorso, F.; Sun, Z.; Hasan, T.; Ferrari, A., Graphene photonics and optoelectronics. *Nat. Photonics* **2010,** *4* (9), 611.

148. Zhang, F.; Li, W.; Ma, Y.; Tang, Y.; Dai, X., Tuning the Schottky contacts at the graphene/WS_2 interface by electric field. *RSC Advances* **2017,** *7* (47), 29350-29356.

149. Kresse, G.; Hafner, J., Ab initio molecular dynamics for liquid metals. *Phys. Rev. B* **1993,** *47* (1), 558.

150. Perdew, J.; Burke, K.; Ernzerhof, M., Perdew, burke, and ernzerhof reply. *Phys. Rev. Lett.* **1998,** *80* (4), 891.

151. Grimme, S.; Antony, J.; Ehrlich, S.; Krieg, H., A consistent and accurate ab initio parametrization of density functional dispersion correction (DFT-D) for the 94 elements H-Pu. *J. Chem. Phys.* **2010,** *132* (15), 154104.

152. Yazyev, O. V.; Louie, S. G., Topological defects in graphene: Dislocations and grain boundaries. *Phys. Rev. B* **2010,** *81* (19), 195420.

153. Monkhorst, H. J.; Pack, J. D., Special points for Brillouin-zone integrations. *Phys. Rev. B* **1976,** *13* (12), 5188.

154. Tongay, S.; Fan, W.; Kang, J.; Park, J.; Koldemir, U.; Suh, J.; Narang, D. S.; Liu, K.; Ji, J.; Li, J., Tuning interlayer coupling in large-area heterostructures with CVD-grown MoS_2 and WS_2 monolayers. *Nano Lett.* **2014,** *14* (6), 3185-3190.

155. Lu, Y.; Zeng, J.; Wang, S.; Sun, B.; Wang, Q.; Lu, J.; Gravier, S.; Bladin, J.; Wang, W.; Pan, M., Structural signature of plasticity unveiled by nano-scale viscoelastic contact in a metallic glass. *Sci. Rep.* **2016,** *6*, 29357.

156. Huang, W.; Liu, Z.-F.; Yang, Z.-Y., Top or underneath? Revealing the structure of multilayer graphene domains with atomic force microscopy and theoretical analysis. *Carbon* **2016,** *99*, 131-137.

157. Walter, T. N.; Kwok, F.; Simchi, H.; Aldosari, H. M.; Mohney, S. E., Oxidation and oxidative vapor-phase etching of few-layer MoS_2. *J. Vac. Sci. Technol. B* **2017,** *35* (2), 021203.

158. Smith, B. W.; Luzzi, D. E., Electron irradiation effects in single wall carbon nanotubes. *J. Appl. Phys.* **2001,** *90* (7), 3509-3515.

159. Komsa, H.-P.; Kotakoski, J.; Kurasch, S.; Lehtinen, O.; Kaiser, U.; Krasheninnikov, A. V., Two-dimensional transition metal dichalcogenides under electron irradiation: defect production and doping. *Phys. Rev. Lett.* **2012,** *109* (3), 035503.

160. Meyer, J. C.; Chuvilin, A.; Algara-Siller, G.; Biskupek, J.; Kaiser, U., Selective sputtering and atomic resolution imaging of atomically thin boron nitride membranes. *Nano Lett.* **2009,** *9* (7), 2683-2689.

161. Wang, B.; Puzyrev, Y. S.; Pantelides, S. T., Enhanced chemical reactions of oxygen at grain boundaries in polycrystalline graphene. *Polyhedron* **2013,** *64*, 158-162.

162. Di Valentin, C.; Ferrighi, L.; Fazio, G., Theoretical Studies of Oxygen Reactivity of Free-Standing and Supported Boron-Doped Graphene. *ChemSusChem* **2016,** *9* (10), 1061-1077.

163. Eberlein, T.; Bangert, U.; Nair, R.; Jones, R.; Gass, M.; Bleloch, A.; Novoselov, K.; Geim, A.; Briddon, P., Plasmon spectroscopy of free-standing graphene films. *Phys. Rev. B* **2008,** *77* (23), 233406.

164. Kapetanakis, M. D.; Zhou, W.; Oxley, M. P.; Lee, J.; Prange, M. P.; Pennycook, S. J.; Idrobo, J. C.; Pantelides, S. T., Low-loss electron energy loss spectroscopy: An atomic-resolution complement to optical spectroscopies and application to graphene. *Phys. Rev. B* **2015,** *92* (12), 125147.

165. Bulusheva, L.; Sedelnikova, O.; Okotrub, A., Many-body effects in optical response of graphene-based structures. *Int. J. Quantum Chem* **2016,** *116* (4), 270-281.

166. Laffont, L.; Monthioux, M.; Serin, V., Plasmon as a tool for in situ evaluation of physical properties for carbon materials. *Carbon* **2002,** *40* (5), 767-780.

167. Oh, H.; Hong, Y. J.; Kim, K.-S.; Yoon, S.; Baek, H.; Kang, S.-H.; Kwon, Y.-K.; Kim, M.; Yi, G.-C., Architectured van der Waals epitaxy of ZnO nanostructures on hexagonal BN. *NPG Asia Mater.* **2014,** *6* (12), e145.

168. Gass, M. H.; Bangert, U.; Bleloch, A. L.; Wang, P.; Nair, R. R.; Geim, A., Free-standing graphene at atomic resolution. *Nat. Nanotechnol.* **2008,** *3* (11), 676.

169. Cusati, T.; Fiori, G.; Gahoi, A.; Passi, V.; Lemme, M. C.; Fortunelli, A.; Iannaccone, G., Electrical properties of graphene-metal contacts. *Sci. Rep.* **2017,** *7* (1), 5109.

170. Ruzmetov, D.; Zhang, K.; Stan, G.; Kalanyan, B.; Bhimanapati, G. R.; Eichfeld, S. M.; Burke, R. A.; Shah, P. B.; O'Regan, T. P.; Crowne, F. J., Vertical 2D/3D semiconductor heterostructures based on epitaxial molybdenum disulfide and gallium nitride. *ACS Nano* **2016,** *10* (3), 3580-3588.

171. Shi, S.; Gao, D.; Xia, B.; Liu, P.; Xue, D., Enhanced hydrogen evolution catalysis in MoS_2 nanosheets by incorporation of a metal phase. *J. Mater. Chem. A* **2015,** *3* (48), 24414-24421.

172. Park, C.; Fenter, P. A.; Nagy, K. L.; Sturchio, N. C., Hydration and distribution of ions at the mica-water interface. *Phys. Rev. Lett.* **2006,** *97* (1), 016101.